Grant Agreement No: 101096307

Full Title: THz Industrial Mesh Networks in Smart Sensing and Propagation Environments

Start date: 01/01/2023

End date: 31/12/2025

Duration: 36 Months

DeliverableD4.2

Intermediate report on multi-goal mesh network optimization and exploitation of smart propagation environments

Document Type	Deliverable
Title	D4.2 - Intermediate report on multi-goal mesh network optimization and exploitation of smart propagation environments
Contractual due date	30/06/2024
Actual submission date	21/06/2024
Nature	Report
Dissemination Level	PUB
Lead Beneficiary	CNIT
Responsible Author	Marco Moretti (CNIT)
Contributions from	Giacomo Bacci, Chiara Buratti, Sara Cavallero, Giampaolo Cuozzo, Davide Dardari, Marina Lotti, Francesco Miccoli, Marco Moretti, Alessia Tarozzi, Giulia Torcolacci (CNIT), Lutfi Samara, Malte Schellmann, Tommaso Zugno (HWDU), Steffen Kroos (TUBS)

Revision history

Version	Issue Date	Changes	Contributor(s)
v0.1	22/02/2024	Initial Version	Giampaolo Cuozzo (CNIT), Giacomo Bacci (CNIT), Marco Moretti (CNIT), Tommaso Zugno (HWDU)
v0.2	07/06/2024	Version for the Reviewers	Giacomo Bacci (CNIT), Giampaolo Cuozzo (CNIT), Sara Cavallero (CNIT), Alessia Tarozzi (CNIT), Francesco Miccoli (CNIT), Chiara Buratti (CNIT), Davide Dardari (CNIT), Marina Lotti (CNIT), Marco Moretti (CNIT), Lutfi Samara (HWDU), Malte Schellmann (HWDU), Giulia Torcolacci (CNIT), Tommaso Zugno (HWDU), Steffen Kroos (TUBS)
v0.3	21/06/2024	Edit from revised Version	Giacomo Bacci (CNIT), Giampaolo Cuozzo (CNIT), Sara Cavallero (CNIT), Alessia Tarozzi (CNIT), Francesco Miccoli (CNIT), Chiara Buratti (CNIT), Davide Dardari (CNIT), Marina Lotti (CNIT), Marco Moretti (CNIT), Lutfi Samara (HWDU), Malte Schellmann (HWDU), Giulia Torcolacci (CNIT), Tommaso Zugno (HWDU), Steffen Kroos (TUBS)
v1.0	21/06/2024	Final Version	Danila Ferretti (CNIT), Luca Sanguinetti (CNIT)

Disclaimer

Copyright Message

Table of Contents

List of Abbreviations

6G sixth-generation

ACK Acknowledgment

AI Artificial Intelligence

AoA Angle of Arrival

AoD Angle of Departure

AWGN Additive White Gaussian Noise

BER Bit Error Rate

BO Back-Off

BS Base Station

CIR Channel Impulse Response

CN Camera Node

CSI channel state information

EM electromagnetic

FIR finite impulse response

FSS Frequency Selective Surface

HO handover

ISAC Integrated Sensing and Communication

ISI Inter-Symbol Interference

ISP Inverse Scattering Problem

KPI Key Performance Indicator

LLS link level simulator

LOS Line of Sight

LS Least Squares

MAC Medium Access Control

MIMO Multiple-Input-Multiple-Output

ML Maximum Likelihood

MPC Multipath Component

MSE Mean Square Error

MMSE Minimum Mean Square Error

MR Maximum Ratio

NLOS Non Line of Sight

NMSE Normalized Mean Square Error

NRT Non Real-Time

OFDM Orthogonal Frequency Division Multiplexing

PAP power angular profile

PDP power delay profile

PEC Perfect Electric Conductor

PHY physical

PLC Programmable Logic Controller

RCS Radar Cross Section

RF Radio Frequency

RIS Reconfigurable Intelligent Surface

ROI Region of Interest

RSRP Referenz Signal Received Power

RX Receiver

SAR Synthetic Aperture Radar

SIMO Single Input Multiple Output

SiMoNe Simulator for Mobile Networks

SLS system level simulator

SNR Signal-to-Noise-Ratio

SINR Signal-to-Interference-plus-Noise Ratio

SNR signal-to-noise-ratio

THz Terahertz

TSVD Truncated Singular Value Decomposition

TX Transmitter

UE User Equipment

WP Work Package

BS base station

FF far-field

LoS line-of-sight

NF near-field

NLoS non-line-of-sight

RIS Reflective Intelligent Surface

RT Real-Time

UE User Equipment

UPA uniform planar array

ULA uniform linear array

Executive Summary

The TIMES project's objective is to construct an intelligent radio environment capable of functioning in complex industrial environments, offering performance comparable to wired networks. Central to this endeavor is the adoption of Terahertz (THz) communications as the primary technological catalyst. Leveraging the abundant radio resources in THz bands and the sensor-friendly attributes of THz signals, the project aims to facilitate extremely high data rates (measured in terabits per second), ultra-low latency, precise sensing capabilities, and high reliability. However, working with THz frequencies poses significant challenges, particularly in channel propagation.

To tackle these challenges, the project focuses on exploiting smart propagation environments and multi-goal mesh-based THz radio networks able to guarantee wired-like performance and support heterogeneous devices. In particular, this deliverable is divided in two main parts: the first part, corresponding to Section 2, presents preliminary findings on physical level issues related to smart propagation environments, the second one, presented in Section 3, describes intermediate outcomes on the most important aspects related to the optimization of THz-based multi-goal mesh networks.

1 Introduction

The TIMES project envisions a smart radio ecosystem operating at THz frequencies able to achieve wired like performance and support a large number of heterogeneous devices in complex scenarios such as industrial environments. One of the main objective of the project is to develop the innovative "intelligent and multi-goal mesh network" concept, where the radio access network is assisted by a smart propagation environment made of active nodes and metasurfaces interconnected in a mesh topology and leverages intelligent MAC and networking protocols.

A key focus is on the use of metasurfaces such as Reflective Intelligent Surfaces (RISs) and metaprisms to enhance physical layer performance, particularly in the THz range, which is crucial for enabling high data-rate applications in complex scenarios. Accordingly, the first part of this document explores various facets of RIS, such as their performance at THz frequencies, their impact on Multiple-Input-Multiple-Output (MIMO) channels, and their effectiveness under phase error conditions. Additionally, the role of metaprisms and their communications and sensing applications within industrial environments is examined. The implementation of a simulation tool able to evaluate the performance of smart propagation environments with a high level of realism is discussed.

The second part of the document delves into the design of THz-tailored Medium Access Control (MAC) protocols from a network-level perspective. In particular, it addresses the deployment of sensors in real factory settings, focusing on the challenges and innovations required to handle the vast and heterogeneous amounts of data generated by these sensors. Indeed, these scenarios are extremely challenging from the design of mobile radio networks, as the number of sensors, as well as the corresponding data-rates, produce network throughput that can be as large as tens of Gbit/s, and sensor miniaturization imposes another fundamental constraint. The document then discusses the implications of these challenges on THz-based MAC protocols, by also considering two network architectures, star and mesh, and the main peculiarities of such high frequencies. The implications of employing RISs and smart propagation environments are also preliminarily analyzed.

It is deemed appropriate to point out that the results reported in this document are preliminary as the aforementioned activities are still ongoing. The final outcomes will be presented in a subsequent report and will provide more detailed design guidelines for the optimization of THz-based multi-goal mesh networks and exploitation of smart propagation environments.

1.1 Scope

This deliverable presents enhanced opportunities offered by the exploitation of intelligent reflecting surfaces within multi-goal mesh networks. It also describes the intermediate outcomes concerning multi-goal network optimization schemes and MAC procedures developed for THz-based mesh networks.

1.2 Audience

This report is intended for public use.

1.3 Structure

This deliverable is organized in two main parts: the first part, corresponding to Section 2, mainly deals with physical level issues related to smart propagation environments, the second one, presented in Section 3, addresses the most important aspects of optimization of THz-based mesh networks.

In details, Section 2 first briefly introduces the channel models of THz propagation and then investigates the theoretic potentials of employing RISs. This investigation is eventually employed to study the performance of RIS-enhanced factory environments. To make these studies more realistic, we will evaluate the impact of RF

impairments on RIS-based networks at THz. A multi-carrier approach employing passive metaprisms is also considered. The study of the potentials of THz channels for enhancing sensing and localization with the use of RISs concludes this section. Eventually, the SW tool Simulator for Mobile Networks (SiMoNe) will be employed to integrate and evaluate selected solutions proposed in this deliverable.

After both the characterization of the PHY layer and the exploitation of RIS at THz frequencies, Section 3 shifts focus to higher-layer aspects, specifically the design and validation of MAC protocol features tailored for THz networks, encompassing both star and mesh network architectures. Initially, the section delineates the complex industrial environment under consideration, namely Robopac-Aetna and Bi-Rex, and its corresponding modeling. Subsequently, we assess the performance of well-established contention-based MAC protocols, namely Slotted and Unslotted Aloha, within the context of a star network topology operating at THz frequencies. To address the identified challenges posed by the unique characteristics of THz frequencies, we further propose an optimization strategy employing mesh networking at these frequencies, facilitated by a custom MAC protocol solution. Finally, we elucidate the potential integration of a PHY layer incorporating RISs into the proposed network simulator, concluding with a summary of findings.

2 THz communications in smart propagation environments

Smart propagation environments refer to advanced systems and technologies designed to optimize the transmission and reception of wireless signals. These environments utilize intelligent infrastructure and adaptive technologies to enhance signal quality, coverage, and overall network performance. In particular, this section studies communication and sensing techniques in smart propagation environments in a factory ecosystem, particularly focusing on the physical layer in the THz range. Among the smart propagation environments, RISs are planar structures, often called metasurfaces, composed of cells designed to control electromagnetic waves with unprecedented flexibility and efficiency. They are further classified into various categories based on their specific design, functionality, and applications. Various technologies exist for creating RIS, each adhering to its own specific model. Broadly, RIS can be categorized into two types: those with cells acting as small radiating elements with tunable load impedance [1–4] and subwavelength RIS that modify the electromagnetic (EM) field and can be modelled as impedance sheets [5–9]. Although the concepts and novel solutions discussed below can be in principle applicable to both types, for the sake of clarity and analysis, we primarily focus on the former category in this deliverable.

First, in Sect. 2.1 the performance of RISs at THz frequencies are studied by evaluating the impact of a number of parameters in the system design. In particular, the section is structured to: 1) briefly introduce the channel models used to properly describe the propagation scenarios, 2) evaluate the RIS-assisted propagation scenario as a function of the locations of the system entities and the RIS size, and 3) investigate the achievable throughput of the RIS-aided architecture as a function of the main system parameters.

The potentials of the RIS in a line-of-sight (LoS) MIMO channel are analyzed in Sect. 2.2. The high-rank LoS-MIMO channel created by RIS in the radiative near-field allows for parallel communication via eigenchannels, significantly boosting link capacity compared to a direct link.

In order to develop a more realistic model of the smart propagation environments, Sect. 2.3 evaluates the performance of an RIS-assisted communication link when the reflecting elements have phase errors. The impact of these errors on average SNR (Signal-to-Noise Ratio) and spectral efficiency is highlighted.

Metaprisms are a particular class of passive smart environments and Sect. 2.4 introduces metaprisms as a static Frequency Selective Surface (FSS), which offers different reflection behaviours based on the incident signal's spectral characteristics. This section details: 1) the system model, 2) the frequency-dependent phase profile and its application in beam steering, 3) non-line-of-sight (NLoS) conditions, and LoS with a transmitted antenna array. The performance is visualized using signal-to-noise-ratio (SNR) heat maps.

The characteristics of intelligent surfaces can be exploited for both imaging and location. Sect. 2.5 presents algorithms designed for localization in NLoS conditions by using the metaprism introduced in Sect. 2.4. Additionally, Sect. 2.5 addresses near-field imaging using extremely large-scale MIMO (XL-MIMO) antennas and RIS. The section details a system for holographic imaging, where a fixed transmitting antenna array illuminates a Region of Interest (ROI) and a fixed receiving array estimates the ROI's scattering coefficients. The optimal illumination signal and RIS configuration are derived, and successful image retrieval from an industrial ROI is presented to validate the proposed imaging algorithm.

Finally, Sect. 2.6 introduces SiMoNe, a simulation tool designed for evaluating the algorithms proposed in this Deliverable. The main focus of this activity has been to lay the groundwork in preparation for a successive SW release.

2.1 Performance and design of RIS at THz

Considering the deterministic channel modelling detailed in [10], we begin by comparing the channel gain experienced by the User Equipment (UE) in the LoS scenario (the direct link between the base station (BS) and the UE), with the channel gain measured in the NLoS scenario (i.e., without the BS-UE direct link, and hence BS and UE are connected through the RIS).

Parameter	Value	Parameter	Value
Carrier frequency	$f_c = 100 \div 1,000$ GHz	Wavelength	$\lambda = 0.3 \div 3$ mm
Antenna area	$A = \left(\frac{\lambda}{4}\right)^2$	Array height	$h = 0 \div 5$ m
Horizontal spacing	$d_H = \lambda/2$	Vertical spacing	$d_V = \lambda/2$

Table 1: RIS parameters.

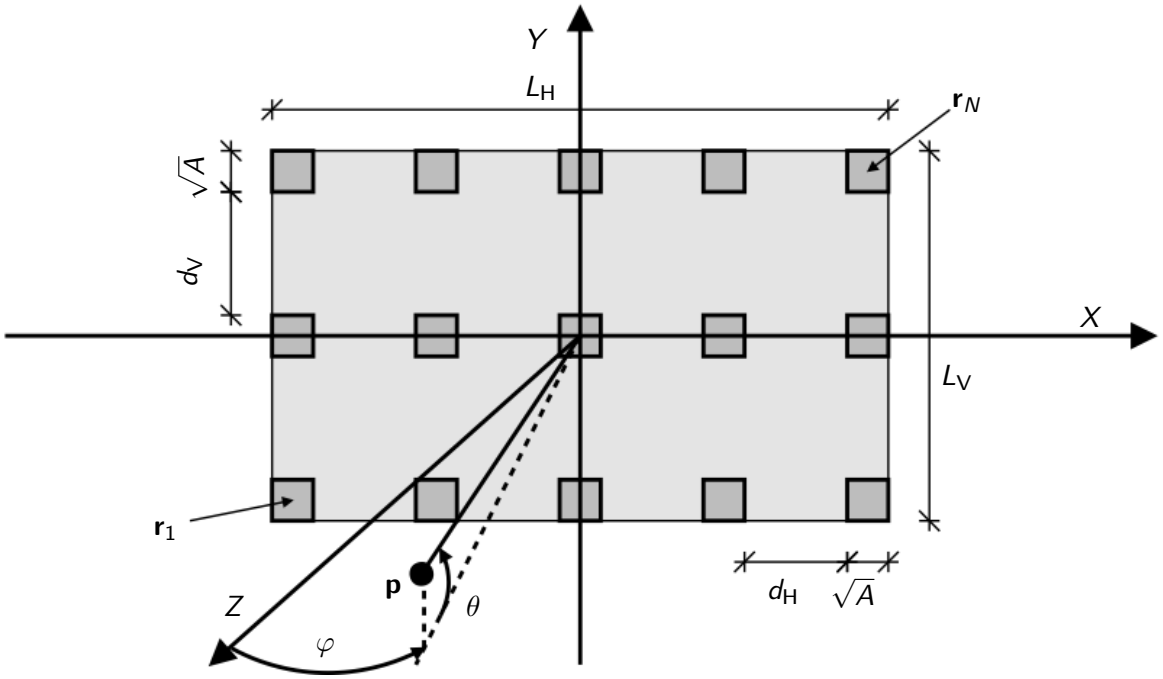

Figure 1: Diagram of the 2D planar array located in the XY-plane.

2.1.1 Channel models

To introduce the effects of the propagation channel, we consider the planar array shown in Figure 1, detailed in [10]. The array consists of N_V horizontal rows and N_H antennas per row, for a total of $N = N_H N_V$ antennas. Each antenna is a squared patch antenna and has an area A. The spacing (between edges) is d_H and d_V along the horizontal and vertical directions, respectively. Thus, the horizontal and vertical lengths of the array are respectively given by

$$L_H = N_H\sqrt{A} + (N_H - 1)\, d_H \tag{1}$$

$$L_V = N_V\sqrt{A} + (N_V - 1)\, d_V. \tag{2}$$

The antennas are numbered from left to right and from the bottom row to the top row so that antenna n is located at $\mathbf{r}_n = [x_n, y_n, z_n]^T$, where

$$x_n = \Delta_H \left(-\frac{N_H - 1}{2} + \mathrm{mod}\,(n-1, N_H)\right) \tag{3}$$

$$y_n = \Delta_V \left(-\frac{N_V - 1}{2} + \lfloor (n-1)/N_H \rfloor\right) \tag{4}$$

with $\Delta_H = \sqrt{A} + d_H$ and $\Delta_V = \sqrt{A} + d_V$, and z_n is the height of the nth radiating element of the array.

The mathematical model employed to describe the propagation channel depends on the distance d_{Tx-Rx} between the transmitter and the receiver. When d_{Tx-Rx} is smaller than the Fraunhofer distance, computed

as

$$d_{\mathrm{F}} = 2\frac{L_{\mathrm{H}}^2 + L_{\mathrm{V}}^2}{\lambda}, \tag{5}$$

then the channel can be described as near-field (NF), while when it is $d_{Tx-Rx} > d_{\mathrm{F}}$ the propagation takes place in the so-called far-field (FF) region.

Near-field channel model To model the channel vector $\mathbf{h}^{\mathrm{NF}}$ between the planar array and a generic single-antenna device located in $\mathbf{p} = [x, y, z]^{\mathsf{T}}$, we assume that the transmission makes use of Y-polarized signals when traveling in the Z direction. Under this hypothesis,

$$\mathbf{h}^{\mathrm{NF}} = \left[\left|h_1{}^{\mathrm{NF}}\right| e^{j\varphi_1^{\mathrm{NF}}}, \left|h_2{}^{\mathrm{NF}}\right| e^{j\varphi_2^{\mathrm{NF}}}, \ldots, \left|h_N{}^{\mathrm{NF}}\right| e^{j\varphi_N^{\mathrm{NF}}}\right] \tag{6}$$

where the (squared) amplitude of each radiating element n is

$$\begin{aligned}\left|h_n^{\mathrm{NF}}\right|^2 = &\frac{1}{12\pi}\sum_{i=0}^{1}\sum_{j=0}^{1}\frac{g_i\left(\Delta x_n\right) g_j\left(\Delta y_n\right)\left|\Delta z_n\right|}{\left(g_j^2\left(\Delta y_n\right) + \Delta z_n^2\right)\sqrt{g_i^2\left(\Delta x_n\right) + g_j^2\left(\Delta y_n\right) + \Delta z_n^2}} \\ &+ \frac{1}{6\pi}\sum_{i=0}^{1}\sum_{j=0}^{1}\tan^{-1}\left(\frac{g_i\left(\Delta x_n\right) g_j\left(\Delta y_n\right)}{\left|\Delta z_n\right|\sqrt{g_i^2\left(\Delta x_n\right) + g_j^2\left(\Delta y_n\right) + \Delta z_n^2}}\right),\end{aligned} \tag{7}$$

where

$$g_i\left(\alpha\right) \triangleq \sqrt{A}/2 + \left(-1\right)^i \alpha, \tag{8}$$

and

$$\Delta x_n = x - x_n, \tag{9}$$
$$\Delta y_n = y - y_n, \tag{10}$$
$$\Delta z_n = z - z_n, \tag{11}$$

whereas the phase can be obtained as

$$\varphi_n^{\mathrm{NF}} = 2\pi \mod \left(\frac{||\mathbf{r}_n - \mathbf{p}||}{\lambda}, 1\right). \tag{12}$$

Far-field channel model Note that the NF model introduced in (6) represents the most general one, which is valid irrespective of the distance between the transmitter and the receiver. When the propagation takes place in the so-called FF region, the channel vector can be approximated as follows:

$$\mathbf{h}^{\mathrm{FF}} = \left[\left|h_1{}^{\mathrm{FF}}\right| e^{j\varphi_1^{\mathrm{FF}}}, \left|h_2{}^{\mathrm{FF}}\right| e^{j\varphi_2^{\mathrm{FF}}}, \ldots, \left|h_N{}^{\mathrm{FF}}\right| e^{j\varphi_N^{\mathrm{FF}}}\right] \tag{13}$$

where the (squared) amplitude of each radiating element n is

$$\left|h_n^{\mathrm{FF}}\right|^2 = \frac{NA\cos\varphi}{4\pi d^2}, \tag{14}$$

where $d = ||\mathbf{r}_{\lfloor N/2 \rfloor} - \mathbf{p}||$ is the distance of the receiver from the center of the array and $\varphi \in [-\pi/2, +\pi/2]$ is the azimuth angle, and

$$\varphi_n^{\mathrm{FF}} = \mathbf{k}^{\mathsf{T}}\left(\varphi, \theta\right)\mathbf{r}_n, \tag{15}$$

where $\mathbf{k}\left(\varphi, \theta\right) = \frac{2\pi}{\lambda}\left[\cos\theta\sin\varphi, \sin\theta, \cos\theta\cos\varphi\right]^{\mathsf{T}}$ is the wave vector [11].

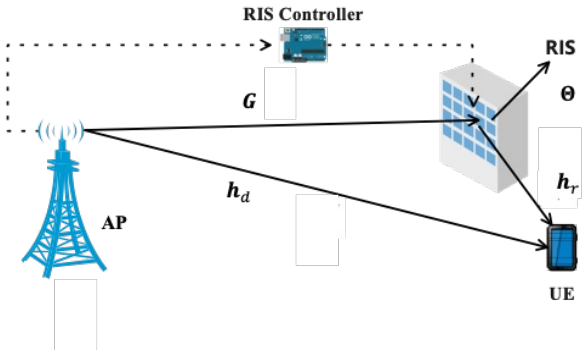

Figure 2: A communication system employing a RIS to enhance its performance.

RIS channel model Figure 2 shows a downlink communication system featuring a RIS equipped with N reflecting elements, aimed at enhancing communications from a BS with M antennas to a single-antenna user, situated near the RIS.

Because the signal impinges on the RIS and is reflected towards the user, the link between the BS and the RIS is obtained as the cascade of two channels: $\mathbf{G} \in \mathbb{C}^{N\times M}$, which is the baseband equivalent wireless channel between the BS and the RIS, and $\mathbf{h}_r \in \mathbb{C}^{1\times N}$, the baseband equivalent wireless channel between the RIS and the user. If also the direct link $\mathbf{h}_d \in \mathbb{C}^{1\times M}$ between the BS and the user is present, the received user's signal can be expressed as

$$\mathbf{y} = (\mathbf{h_r}\boldsymbol{\Theta}\mathbf{G} + \mathbf{h_d})\mathbf{x} \tag{16}$$

where $\boldsymbol{\Theta}$ denotes the $N \times N$ reflection coefficient matrix and $\mathbf{x}$ is the transmitted signal. The link gains $\mathbf{h_r}$, $\mathbf{G}$ and $\mathbf{h_d}$ follow the propagation model of standard wireless links and can be modelled employing the near-field of far-field channel model depending on the various system parameters. In practice, it is reasonable to assume that the connection between the BS and the RIS is in line-of-sight because both devices are in fixed positions, optimized for improving the system performance, while the nature of the other links depends on the propagation scenario and the user's position. In general, RISs are passive devices in terms of gain and, accordingly, the coefficient matrix is usually modelled as a diagonal matrix $\boldsymbol{\Theta} = \text{diag}[e^{j\theta_1}, e^{j\theta_2}, \dots, e^{j\theta_N}]$, where the main diagonal is a vector of phase offsets.

Dimensioning $\boldsymbol{\Theta}$ is a very challenging task and it is usually done by solving specific optimization problems, rendered more difficult by the nonconvex constraint that the module of each RIS coefficient is unitary. A very specific case is the one where the number of antenna elements at the BS is $M = 1$, so that the matrix $\mathbf{G} = [g(1)e^{j\varphi_g(1)}, g(2)e^{j\varphi_g(2)}, \dots, g(N)e^{j\varphi_g(N)}]$ becomes a column vector and both the direct link $h_d = |h_d|e^{j\varphi_0}$ and the cascaded channel gain $h_R = \mathbf{h_r}\boldsymbol{\Theta}\mathbf{G}$ are scalars. In this case, it is

$$h_R = \sum_{n=1}^{N} h_r(n)g(n)e^{j(\varphi_r(n)+\varphi_g(n)+\theta_n)}. \tag{17}$$

The gain of the cascaded channel is maximized when all the components of the vectors $\mathbf{h_r}$ and $\mathbf{G}$ sum coherently. According to the same principle, when the direct link is present the gain of the combined channel $h_d + h_R$ is maximum when the cascaded channel and the direct link are aligned. Thus, by choosing

$$\theta_n = -(\varphi_r(n) + \varphi_g(n)) + \varphi_0, \tag{18}$$

the cascaded channel simplifies to

$$h_R = \sum_{n=1}^{N} h_r(n)g(n)e^{j\varphi_0}, \tag{19}$$

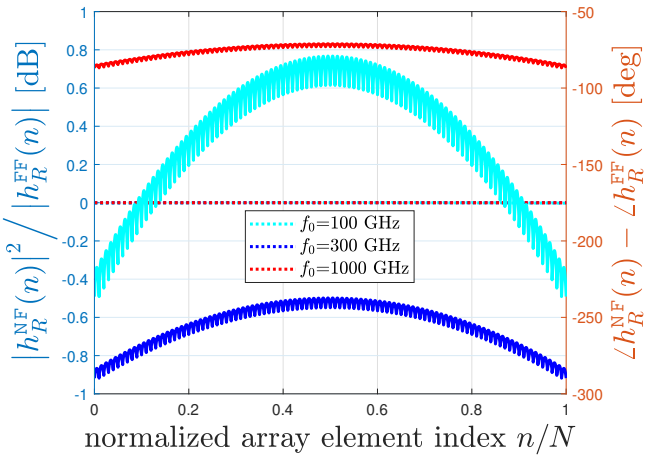

Figure 3: Difference in the amplitude (left axis) and phase (right axis) between the NF model and the FF approximation.

and

$$|h_R| = \sum_{n=1}^{N} h_r(n) g(n). \tag{20}$$

In the remainder of this document, anytime we deal with a system where the BS and the UE are equipped with a single antenna, the RIS coefficients are chosen according to (18).

A comparison of the value of h_R for near-field and far-field channel models By performing an analysis similar to the one proposed in [12], let us analyze the differences in amplitude and phase between the NF and the FF models. A numerical example is reported in Figure 3, which reports the case of a squared RIS equipped with $N = 10,000$ radiating elements, located in between a single-antenna BS (and hence $M = 1$) and a single-antenna UE. To better visualize the scenario, let us focus on the one represented in Figure 4, in which the RIS is located in the XY plane in the origin of the reference system: $\mathbf{r} = (0, 0, 0)$. The BS and the UE are spaced apart by a distance d_0, and are located symmetrically concerning the Z axis, such that the BS's coordinates $\mathbf{b}$ and the UE's coordinates $\mathbf{u}$ are as follows: $\mathbf{b} = (-d_0/2, 0, \delta)$ and $\mathbf{u} = (+d_0/2, 0, \delta)$, where δ is the distance of both the BS and the UE from the RIS on the azimuthal plane, and all entities are located at the same height (otherwise stated, the RIS is not elevated with respect to the UE – we will relax this hypothesis in the remainder of the document).

For our numerical investigation, we consider $d_0 = 20$ m and $\delta = 4$ m with respect to the line joining BS and UE. Three frequencies are considered, $f_0 = [100, 300, 1000]$ GHz, using a spacing across elements equal to $\lambda/2$ and each element's area equal to $(\lambda/4)^2$. Amplitude variations between NF and FF models (with each model indicated by the superscript) are reported with dotted lines (using the left axis), whereas phase variations between NF and FF models are represented by the solid lines (using the right axis). While the amplitude variations are negligible, the phase variations are significant, even for 100 GHz. As better detailed in the next sections, this might have an impact, especially when the distance across the devices grows large, thus approaching (or even going beyond) the Fraunhofer distance [10].

2.1.2 Dimensioning the RIS

For simplicity, we assume both the BS and the UE as single-antenna devices, so that it is $M = 1$, whereas the RIS is equipped with a uniform planar array (UPA) with $N = N_{\mathrm{H}} N_{\mathrm{V}}$ radiating elements.

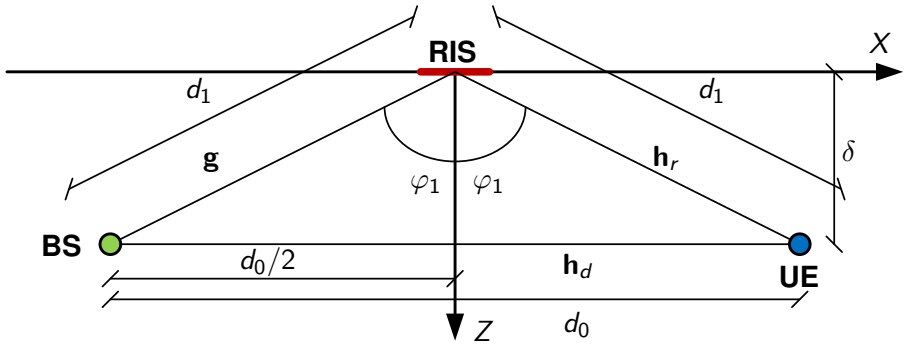

Figure 4: Toy example of RIS-assisted propagation scenario with symmetric placement of BS and UE.

Near-field analysis In this paragraph, we investigate a number of toy scenarios, that are ancillary to evaluate the gain introduced by the RIS to offset the extra-propagation path attenuation introduced by the NLoS (i.e., through the RIS, without the direct link) scenario compared to the LoS (i.e., direct-link BS-UE) one. We start by considering the NF propagation model introduced in Sect. 2.1.1, in which the norm of the channel gain of a generic link, between a single-antenna device and a multi-antenna device equipped with N antennas, can be measured as (6). By using the parameters listed in Table 1, throughout the section we consider $A = (\lambda/4)^2$, where $\lambda = c/f_0$ is the carrier wavelength, and c and f_0 denote the speed of the light and the carrier frequency, respectively.

To better visualize the problem under investigation, let us again focus on the scenario represented in Figure 4. The formulation (7) applies in a single-hop channel, such as the LoS one between the BS and the UE: h_d. In the case of a RIS-aided scenario, we can consider the well-known cascaded channel model detailed in Sect. 2.1.1. Under the hypothesis of perfect channel state information (CSI) information, and thus using a beamforming matrix $\boldsymbol{\Theta}$ which coherently combines the phase of each component of the N-dimensional channel vectors in the BS-to-RIS link, and the RIS-to-UE link, as in (18), the squared amplitude of the cascaded channel gain h_R is equal to the sum of the products of the squared amplitude of the channel gains of each link, as in (20).

For the sake of simplicity, we assume that both the single-element antennas used by BS and the UE do not discriminate across different angles of arrival, and hence the gains do not depend on either the azimuth or the elevation angles. Following the notation introduced in Sect. 2.1.1, $N = 1$, $\mathbf{r} = \mathbf{b}$ and $\mathbf{p} = \mathbf{u}$, and hence $\Delta z = d_0$, and $\Delta x = \Delta y = 0$.[1] Based on (7), the LoS channel gain has an amplitude equal to

$$\left|h_d^{\mathrm{NF}}\right|^2 = \frac{1}{3\pi}\frac{A d_0}{(A+4d_0^2)\sqrt{A/2+d_0^2}} + \frac{2}{3\pi}\tan^{-1}\left(\frac{A}{4d_0\sqrt{A/2+d_0^2}}\right), \tag{21}$$

where the superscript NF is used to emphasize that the NF model is used.

In the case of the RIS equipped with N radiating elements, the squared norm of the cascaded channel is $|h_R^{\mathrm{NF}}| = \sum_{n=1}^{N} h_r^{\mathrm{NF}}(n) \cdot g^{\mathrm{NF}}(n)$, given by (20), where each component of the sum is modeled by (7), with $\mathbf{p} = \mathbf{b}$ and $\mathbf{p} = \mathbf{u}$, respectively.

While we cannot compute the closed-form expression, we can numerically solve

$$\left|h_d^{\mathrm{NF}}\right| = \left|h_R^{\mathrm{NF}}\right|, \tag{22}$$

that yields the results illustrated in Figure 5, which reports the RIS size (plotted as $\log_{10} N$ instead of N, to better appreciate the variations in the colormap) as a function of the carrier frequency (left axis) and of the distance δ on the azimuthal plane (bottom axis). As can be seen, for a given δ, increasing the carrier frequency increases N, due to a more severe path loss (which counts twice in the cascaded channel compared to the LoS link): as an example, when $\delta = 2\,\mathrm{m}$ and $f_0 = 300\,\mathrm{GHz}$, a RIS with $N \approxeq 370,000$ radiating elements is required.

[1] To properly account for the relative azimuth and elevation between the BS and the UE, a rotation of the reference system must be applied, so that $x'_u = x_b - (z_u - z_b)$ and $z'_u = z_b - (x_u - x_b)$, while $y'_u = y_u$.

For a given f_0, in the selected scenario the behaviour of N is not monotonically increasing, due to the following reason. When δ is small, both the BS and the UE are located far away from the boresight direction of the RIS, and hence the reduced RIS-UE distance d_1 (25) is overwhelmed by the poor RIS antenna gain. As δ increases, despite the fact that also the distance d_1 increases (and with it the path loss, according to (26)), both the BS and the UE get closer to the direction of maximum gain (i.e., φ_1 becomes smaller), and hence the necessary N reduces. This trend continues up to a certain distance $\delta^\star$ (with the selected parameters, $\delta^\star \cong 7$ m for almost all considered frequencies): since then, N becomes increasing again, as the RIS gain cannot keep the pace with the increased path loss. As an example, Figure 6 reports N as a function of δ for $f_0 = 300$ GHz.

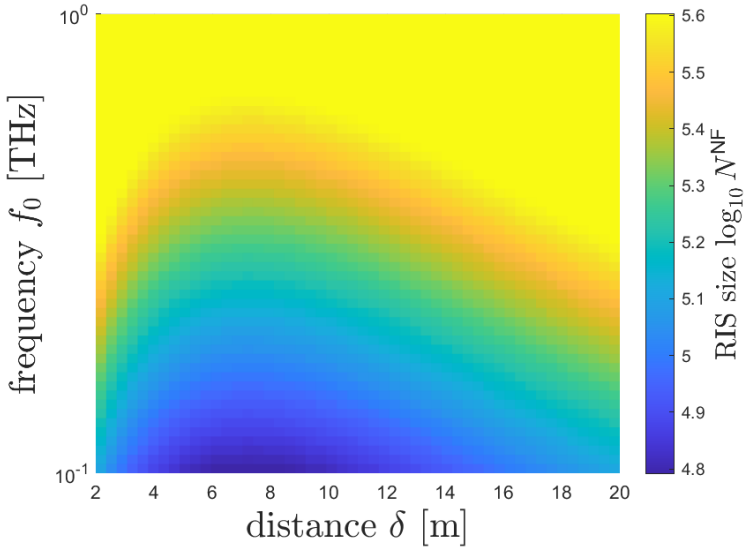

Figure 5: RIS size N as a function of the carrier frequency f_0 and the distance δ on the azimuthal plane to equalize LoS and NLoS RIS-aided paths (near-field scenario).

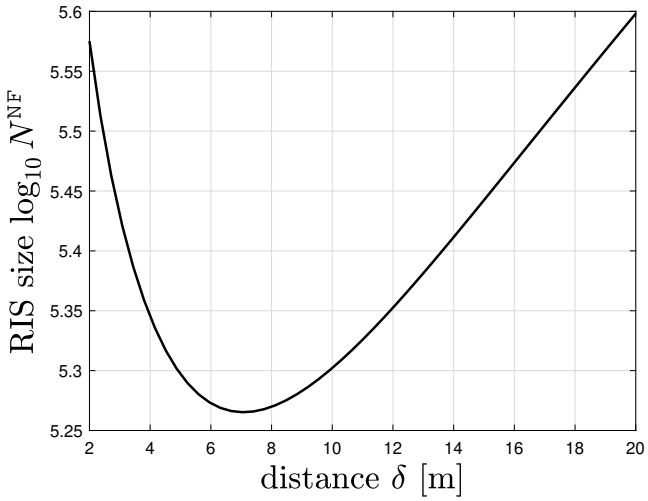

Figure 6: RIS size N as a function of the distance δ on the azimuthal plane to equalize LoS and NLoS RIS-aided paths (near-field scenario, $f_0 = 300$ GHz).

Let us now remove the constraint of symmetry considered in Figure 4, and let us consider the scenario plotted in Figure 7. This means that we want to investigate the behavior of the RIS size when, for a given distance δ, we move the RIS closer to either the UE or the BS. Otherwise stated, for a given distance d_0, the coordinate $x = x_u$ (i.e., UE X-coordinate) takes all the values in the range $[0, d_0]$, with $x = 0$ denoting the UE right in front

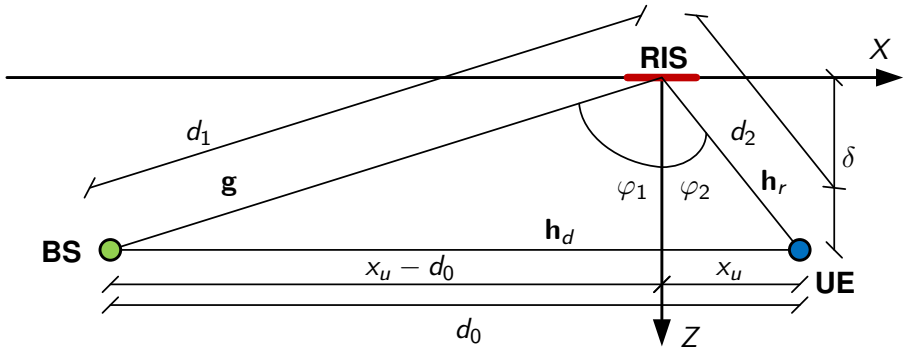

Figure 7: Toy example of RIS-assisted propagation scenario with asymmetric placement of BS and UE.

of the RIS, and $x = d_0$ denoting the opposite case of the BS placed in front of the RIS.

Since now $\mathbf{u} = (x, 0, \delta)$ and $\mathbf{b} = (x - d_0, 0, \delta)$, we can conduct the same numerical analysis performed above, in which it is easy to verify that the case investigated in Figure 4 is a special case of Figure 7, where $x = d_0/2$. We can thus obtain Figure 8, which reports the RIS size (plotted as $\log_{10} N$ instead of N, to better appreciate the variations in the colormap) as a function of the carrier frequency (left axis) and of the UE's X coordinate, given the distance $\delta = 4$ m and the BS-UE distance d_0. As can be seen, due to the fact that both the BS and the UE are single-antenna devices, the results are symmetric with respect to the UE X-coordinate $x_u = d_0/2$ (which also yields the same results of Figure 5, computed for the considered δ). In particular, $x_u = d_0/2$ represents the worst case, as the combination of path loss and RIS directivity is the worst one. As before, increasing the carrier frequency calls for an increasing number of radiating elements N.

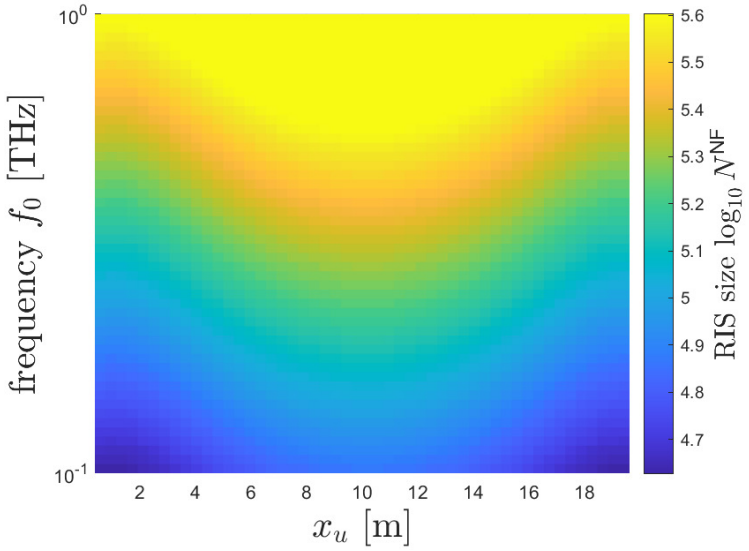

Figure 8: RIS size N as a function of the carrier frequency f_0 and the UE X-coordinate x_u to equalize LoS and NLoS RIS-aided paths ($d_0 = 20$ m, $\delta = 4$ m, using the scenario of Figure 7) (near-field scenario).

Far-field analysis Let us conduct the same analysis when considering the FF propagation model introduced in Sect. 2.1.1 instead of the relation (7). Under this hypothesis, thanks to the duality of the wireless channel in both the uplink and the downlink, each radiating element n of the RIS depicted in Figure 1 experiences a channel gain (13) [12]. Using the notation introduced in Sect. 2.1.2, $\mathbf{p} = \mathbf{b}$ in the case of the BS, and $\mathbf{p} = \mathbf{u}$ in the case of the UE).

Let us consider again the scenario reported in Figure 4, in which there is only one radiating element at both the BS and the UE. Based on (14), since $N = 1$, the LoS channel gain has a module equal to

$$|h_d^{\mathrm{FF}}| = \sqrt{\frac{A}{4\pi d_0^2}}, \tag{23}$$

since the azimuth angle is 0 (see Figure 4), and where the superscript FF is used to emphasize that the FF model is used.

To compute the amplitude of the channel gains $g^{\mathrm{FF}}(n)$ between the BS and the RIS, and of the channel gains $h_r^{\mathrm{FF}}(n)$ between the RIS and the UE, we need to compute the distance d_1 and the azimuth φ_1 (which is common to both the BS and the UE. It is easy to verify that

$$\varphi_1 = \tan^{-1}\left(\frac{d_0}{2\delta}\right) \tag{24}$$

and

$$d_1 = \frac{d_0}{2\sin\varphi_1}. \tag{25}$$

As a consequence, since the RIS is equipped with N antennas, in the FF hypothesis we have that the squared amplitude of the cascaded channel is equal to

$$g^{\mathrm{FF}}(n) = h_r^{\mathrm{FF}}(n)\sqrt{\frac{A\cos\varphi_1}{4\pi\left[d_0/\left(2\sin\varphi_1\right)\right]^2}} = \sqrt{\frac{A\cos\varphi_1\sin^2\varphi_1}{\pi d_0^2}}. \tag{26}$$

In order to compute the necessary RIS size which guarantees that the amplitude of the cascaded channel equals the LoS channel, we can investigate the equality $|h_d^{\mathrm{FF}}| = |h_R^{\mathrm{FF}}| = \sum_{n=1}^{N} h_r^{\mathrm{FF}}(n)\cdot g^{\mathrm{FF}}(n)$, where the right-hand side corresponds to the norm of the cascaded channel. By simple manipulations, we get

$$N = \frac{d_0}{\cos\varphi_1\sin^2\varphi_1}\sqrt{\frac{\pi}{4A}}, \tag{27}$$

whose behavior as a function of f_0 and δ is plotted in Figure 9.

The same trends observed in Figure 5 are confirmed in Figure 9. However, it is interesting to evaluate the difference $\Delta_N = N^{\mathrm{NF}} - N^{\mathrm{FF}}$ between the RIS size N^{NF}, computed numerically and plotted in Figure 5, and the RIS size N^{FF}, computed as in (27) and plotted in Figure 9. The analysis is presented in Figure 10. Note that, while for low frequencies, $\Delta_N \approxeq 0$, as NF and FF propagation conditions are almost coincident (confirming the findings of [12] and [10]), when increasing f_0 the two solutions differ. In particular, the FF approximation may significantly over-estimate the number N of necessary radiating elements, especially when considering a distance δ which departs from the one that minimizes N (i.e., $\delta^\star$ introduced in Sect. 2.1.2). As a conclusion, it is recommended to adopt the NF channel modeling, in order to avoid the usage of an unnecessarily high size of the RIS.

Let us now focus on the asymmetric scenario depicted in Figure 7. Since $\mathbf{u} = (x, 0, \delta)$ and $\mathbf{b} = (x - d_0, 0, \delta)$, the following quantities can be computed:

$$\varphi_1 = \tan^{-1}\left(\frac{x - d_0}{\delta}\right), \tag{28}$$

$$\varphi_2 = \tan^{-1}\left(\frac{x}{\delta}\right), \tag{29}$$

$$d_1 = \frac{x - d_0}{\sin\varphi_1}, \tag{30}$$

$$d_2 = \frac{x}{\sin\varphi_2}, \tag{31}$$

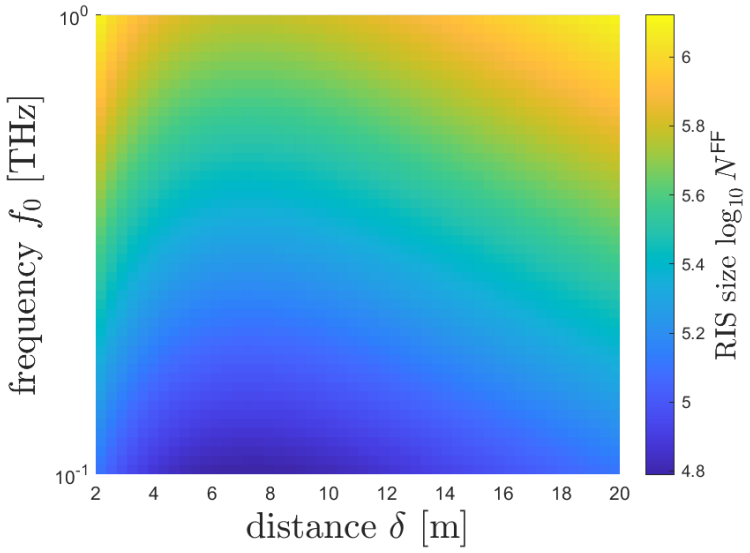

Figure 9: RIS size N as a function of the carrier frequency f_0 and the distance δ on the azimuthal plane to equalize LoS and NLoS RIS-aided paths (far-field scenario).

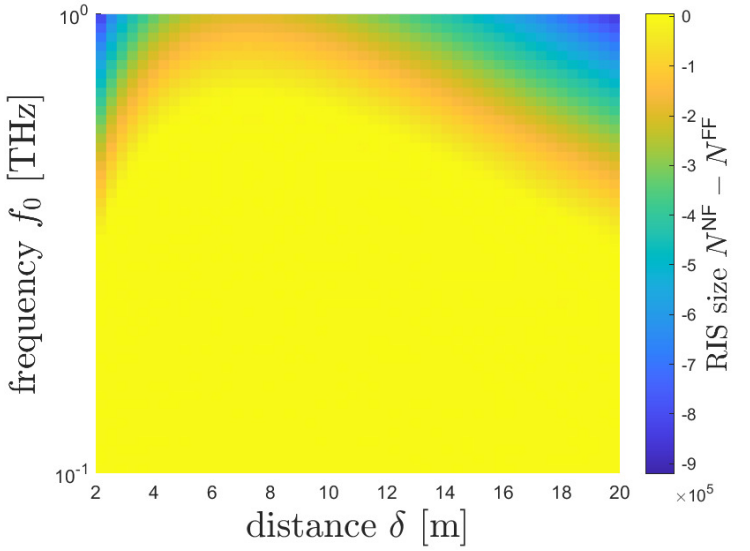

Figure 10: Δ_N as a function of the carrier frequency f_0 and the distance δ on the azimuthal plane to equalize LoS and NLoS RIS-aided paths (near- vs. far-field scenarios).

in which, as expected, the case investigated in Figure 4 is a special case of Figure 7, where $x = d_0/2$. By performing the same operations considered for the case above, we can compute the needed RIS size to equalize the two propagation conditions:

$$N = \sqrt{\frac{4\pi x^2 \left(x - d_0\right)^2}{A d_0^2 \cos\varphi_1 \sin^2\varphi_1 \cos\varphi_2 \sin^2\varphi_2}}, \tag{32}$$

which gives the plot in Figure 11.

To better visualize the problem from another perspective, let us consider the values provided by Figure 11 when

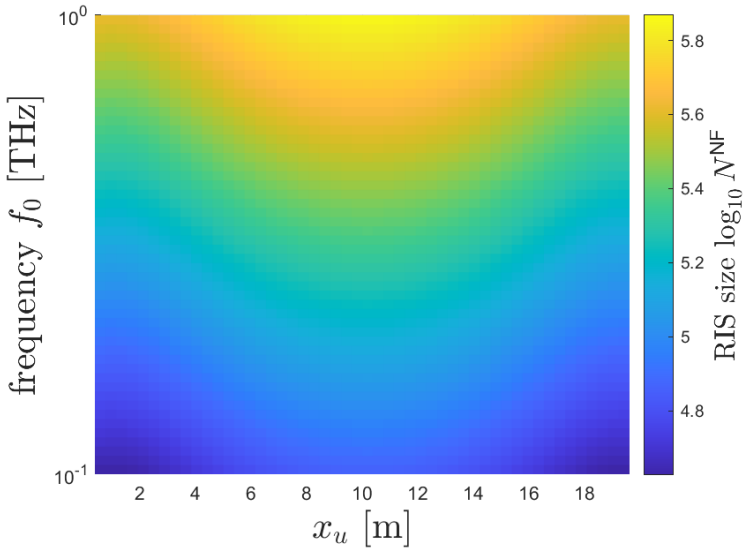

Figure 11: RIS size N as a function of the carrier frequency f_0 and the UE X-coordinate x_u to equalize LoS and NLoS RIS-aided paths ($d_0 = 20$ m, $\delta = 4$ m, using the scenario of Figure 7) (far-field scenario).

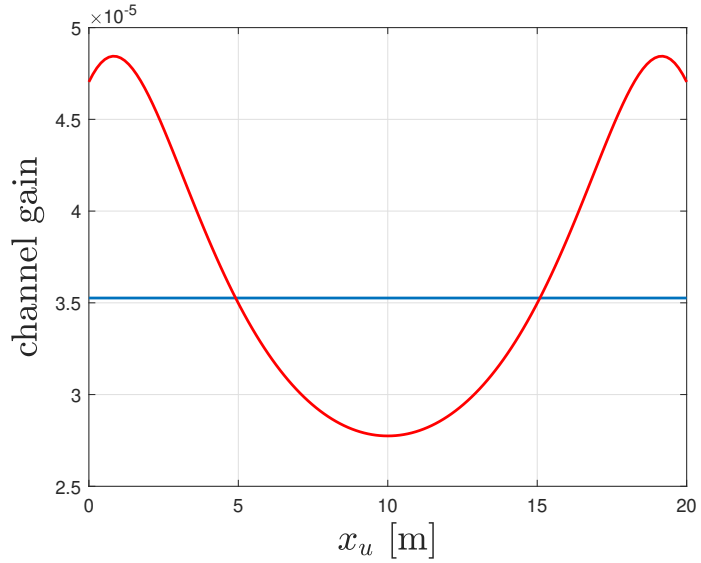

Figure 12: FF channel gains as functions of the UE X-coordinate x_u ($d_0 = 20$ m, $\delta = 4$ m, using the scenario of Figure 7).

$d_0 = 20\,\mathrm{m}$, $\delta = 4\,\mathrm{m}$, $x_u = 5\,\mathrm{m}$, and $f_0 = 30\,\mathrm{GHz}$.[2] In this case, we get $N \cong 17,500$. Figure 12 plots the channel gains $\left|h_d^{\mathrm{FF}}\right|$ (LoS path, blue curve) and $\left|h_R^{\mathrm{FF}}\right|$ (cascaded channel, red curve) as functions of x_u, using $d_0 = 20\,\mathrm{m}$, $\delta = 4\,\mathrm{m}$, $N = 17,500$, and $f_0 = 30\,\mathrm{GHz}$. As expected, $\left|h_{\mathrm{LoS}}^{\mathrm{FF}}\right|$ does not change with x_u, as the BS-UE distance, which is the only parameter that matters, remains the same: $d_0 = 20\,\mathrm{m}$. On the contrary, $\left\|\mathbf{g}_{\mathrm{NLoS}}^{\mathrm{FF}}\right\| \cdot \left\|\mathbf{h}_{\mathrm{NLoS}}^{\mathrm{FF}}\right\|$ does depend on x_u, due to variations in path loss and RIS gain as a function of φ_1 and φ_2. As desired, the two curves intersect for $x_u = 5\,\mathrm{m}$ and $x_u = d_0 - 5\,\mathrm{m} = 15\,\mathrm{m}$ (due to the symmetry already observed above), thus confirming the findings of Figure 11.

[2]Please note that a low value of f_0 has been chosen, in order to avoid numerical issues when increasing N.

Parameter	Value	Parameter	Value
BS-UE distance	$d_0 = 20\,\text{m}$	BS antenna gain (LoS)	$\Gamma_{\text{LoS}} = 55\,\text{dBi}$
RIS-UE Z-plane distance	$\delta = 4\,\text{m}$	BS antenna gain (NLoS)	$\Gamma_{\text{NLoS}} = 40\,\text{dBi}$
RIS-UE X-plane distance	$x_u = 10\,\text{m}$	BS transmit power	$p = 15\,\text{dBm}$
BS/RIS elevation	$h = 0\,\text{m}$	Noise figure	$NF = 8\,\text{dB}$
Bandwidth	$B = 0.1 f_0$	Noise power	$\sigma^2 = -174\,\text{dBm} + NF + B\|_{\text{dB}}$

Table 2: RIS-based simulation parameters.

Following the same approach conducted for the scenario reported in Figure 7, Figure 13 compares the requested RIS size for both NF and FF models for the symmetric case. Again, the difference in the RIS size can be significant (in some cases, more than $1,000$ radiating elements for the selected parameters).

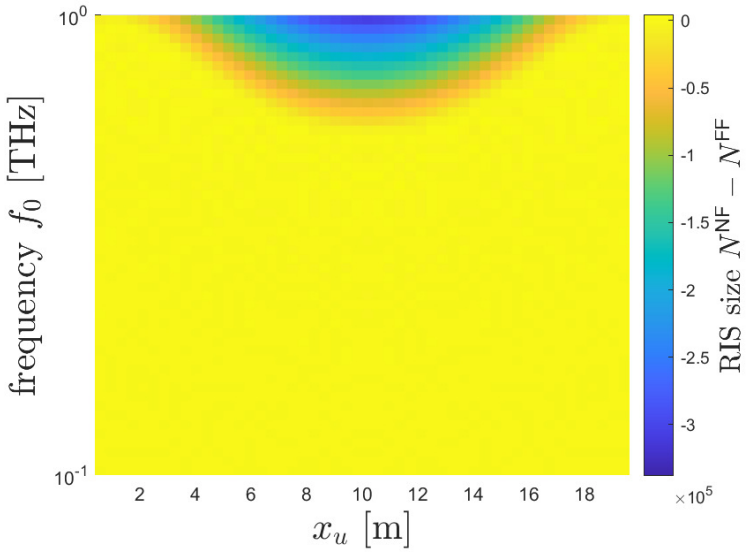

Figure 13: Δ_N as a function of the carrier frequency f_0 and the UE X-coordinate x_u to equalize LoS and NLoS RIS-aided paths ($d_0 = 20$ m, $\delta = 4$ m, using the scenario of Figure 7 (near- vs. far-field scenarios).

To provide a better insight, please refer to the discussion provided in the next section.

2.1.3 Throughput analysis

This section investigates the performance, measured in terms of the achievable throughput, of the direct (LoS) vs. indirect, RIS-aided (NLoS) links, as a function of the carrier frequency f_0 and of the RIS size N. Unless otherwise stated, the relevant simulation parameters are reported in Table 2, having in mind the block diagram depicted in Figure 7.

Since we focus on a single-user scenario, we adopt a Maximum Ratio (MR) combining technique, which yields a SNR equal to

$$\gamma = \frac{\Gamma |h|^2 p}{\sigma^2}, \tag{33}$$

where Γ is the BS transmit antenna gain in the direction of the receiver, p is the BS transmit power, and σ^2 is

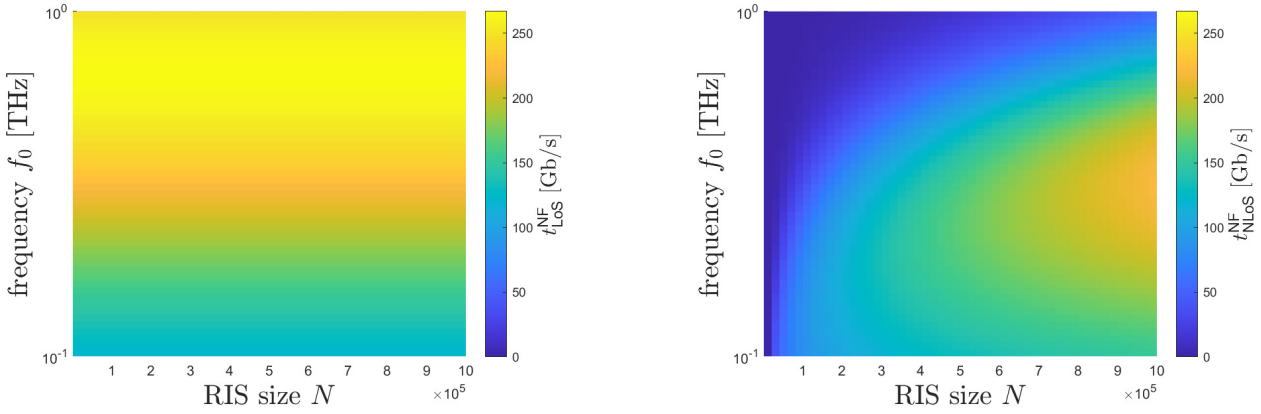

(a) LoS link.

(b) NLoS link.

Figure 14: Throughput as a function of the carrier frequency f_0 and the RIS size N when the RIS is placed closer to the UE (near-field model, $d_0 = 20$ m, $\delta = 4$ m, $x_u = 5$ m).

the noise power, so that the achievable throughput can be measured as

$$t = B \cdot \log_2 (1 + \gamma) . \tag{34}$$

Impact of UE placement We first investigate the difference in performance by considering two different cases:

a) RIS closer to the UE: $x_u = 5$ m (which is equivalent to the case with the RIS closer to the BS, i.e., $x_u = 15$ m, thanks to the symmetry of the entity placement, see Sect. 2.1.2); and

b) RIS at the same distance with respect to the UE and the BS: $x_u = 10$ m.

In both cases, the considered frequency range lies in $[0.1, 1]$ THz, whereas the RIS size N assumes values in the range $[1\,000, 1\,000\,000]$ (in accordance with the numbers found in Sect. 2.1.2).

In the case a) ($x_u = 5$ m), the performance in terms of achievable throughput when the NF model detailed in Sect. 2.1.1 is considered. In particular, Figure 14 reports the values of the throughput $t^{\mathrm{NF}}_{\mathrm{LoS}}$, computed using (34) with $|h|^2 = \left|h^{\mathrm{NF}}_d\right|^2$ (Figure 14(a)), and $t^{\mathrm{NF}}_{\mathrm{NLoS}}$, computed using (34) with $|h|^2 = \left|h^{\mathrm{NF}}_R\right|^2$ (Figure 14(b)), respectively, whereas Figure 15 shows the gap between the LoS and the NLoS links, defined as

$$\Delta_t = t^{\mathrm{NF}}_{\mathrm{LoS}} - t^{\mathrm{NF}}_{\mathrm{NLoS}}. \tag{35}$$

As expected, the throughput achieved in the LoS link does not depend on N, and hence Figure 14(a) shows a constant behavior along the horizontal axis. Interestingly, despite B is increasing with f_0, the throughput $t^{\mathrm{NF}}_{\mathrm{LoS}}$ is not monotonically increasing with f_0, due to the impact of both the path loss and the noise power (which increases with B), which reduces the SNR. When considering the NLoS link, the situation is somewhat similar, although now the RIS size N does affect the performance. In particular, when N is relatively low (in the order of thousands), the throughput $t^{\mathrm{NF}}_{\mathrm{NLoS}}$ is low irrespectively of f_0. When N increases, the RIS gain mitigates the path loss and the noise power, and thus $t^{\mathrm{NF}}_{\mathrm{NLoS}}$ becomes to assume significant values (in the order of tens of Gb/s). When N is extremely large (in the order of hundreds of thousands), then the behavior is similar to the one observed for the LoS link: there is an optimal value of f_0 that maximizes $t^{\mathrm{NF}}_{\mathrm{NLoS}}$: for instance, when $N = 1\,000\,000$, $t^{\mathrm{NF}}_{\mathrm{NLoS}} \approxeq 222$ Gb/s for $f_0 \approxeq 316$ GHz.

When looking at the gap between LoS and NLoS links (reported in Figure 15 using the values reported in Table 2, in particular Γ_{LoS} and Γ_{NLoS})[3], we can observe the following facts:

[3] please see the following sections to evaluate the impact of other parameter configurations.

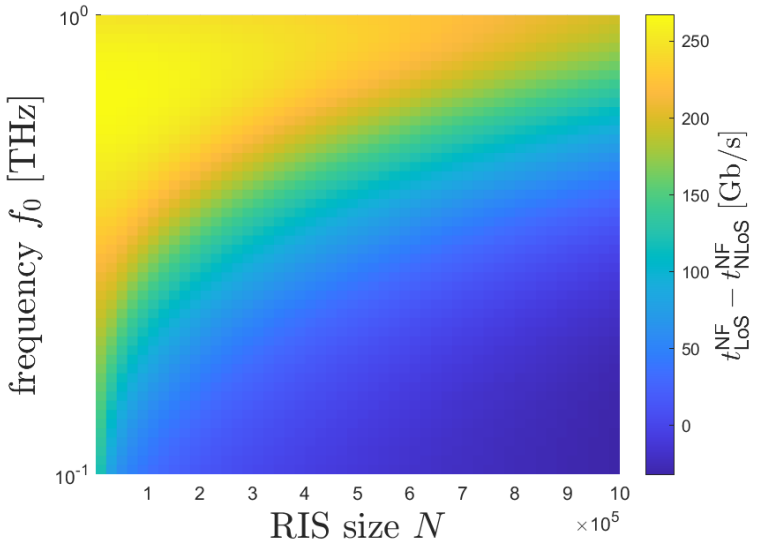

Figure 15: Δ_t as a function of the carrier frequency f_0 and the RIS size N when the RIS is placed closer to the UE (near-field model, $d_0 = 20$ m, $\delta = 4$ m, $x_u = 5$ m).

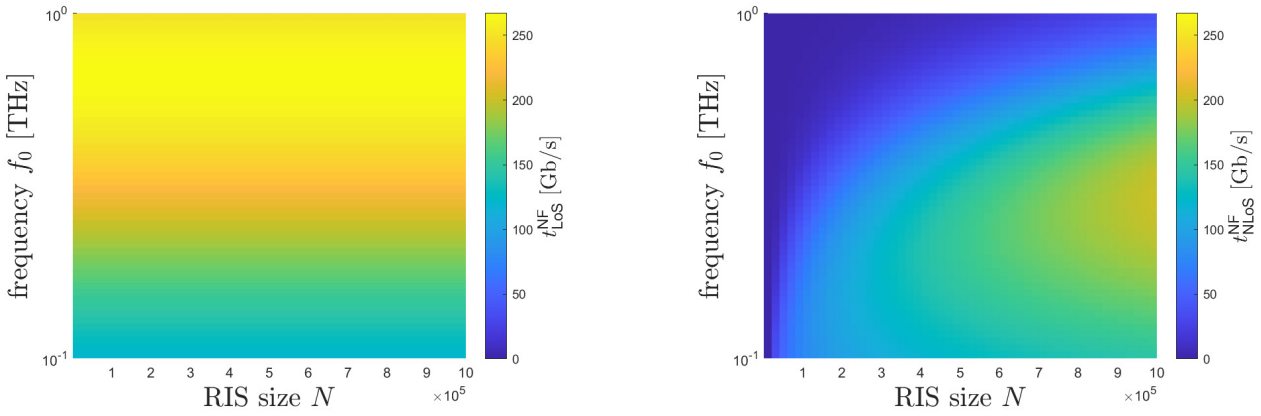

(a) LoS link.

(b) NLoS link.

Figure 16: Throughput as a function of the carrier frequency f_0 and the RIS size N when the RIS is equidistant from UE and BS (near-field model, $d_0 = 20$ m, $\delta = 4$ m, $x_u = 10$ m).

- for low frequencies (i.e., around 100 GHz), the RIS-aided scenario can outperform the LoS one, even when Γ_{NLoS} is significantly lower than Γ_{LoS} (e.g., $\Gamma_{\mathrm{NLoS}} = 40$ dBi $= \Gamma_{\mathrm{LoS}} - 15$ dBi) for a (relatively) low number N of radiating elements (e.g., when $f_0 = 100$ GHz, $N \geq 330\,000$);
- for middle-range frequencies (i.e., around 300 GHz), the RIS-aided scenario can provide approximately the same performance in terms of throughput given by the direct, LoS link, using a large number of radiating elements (e.g., when $f_0 = 300$ GHz, $N \approxeq 100\,000$);
- for high frequencies (i.e., around 1 THz), the RIS-aided link *cannot* achieve the same performance provided by the LoS configuration, even when using an extremely large number N of radiating elements, and hence this shortcoming can be mitigated only by improving the gain Γ_{NLoS} (please see Sect. 2.1.3).

The performance of the case b) ($x_u = 10$ m), when the NF model detailed in Sect. 2.1.1 is considered, is

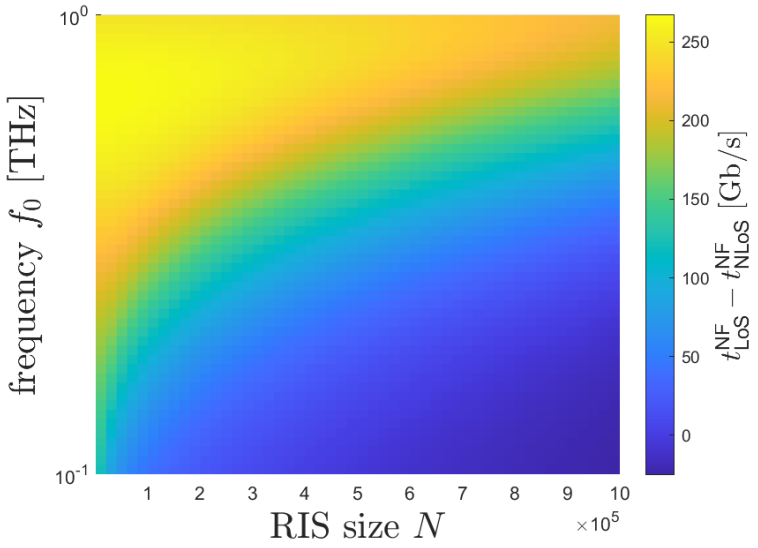

Figure 17: Δ_t as a function of the carrier frequency f_0 and the RIS size N when the RIS is equidistant from UE and BS (near-field model, $d_0 = 20$ m, $\delta = 4$ m, $x_u = 10$ m).

reported in Figs. 16 and 17, showing the gap between the LoS and the NLoS links. In accordance with the results shown in Sect. 2.1.2, this represents the most unfavorable condition for the RIS-aided scenario. In fact, by looking at Figure 17, we can see that an additional number N of radiating elements is required to achieve the same performance of the LoS link, given the same carrier frequency f_0, with respect to the asymmetric situation depicted in Figure 15. Furthermore, the same conclusions drawn before apply in this case as well.

For the sake of completeness, the results in terms of Δ_t are reported in Figure 18 when using the FF model detailed in Sect. 2.1.1 is considered. As can be seen by comparing each subfigure with the NF-based counterpart, the difference when adopting the two models tends to blur. This means that, when considering the throughput (and, in particular, due to the logarithmic relationship between the channel gains and the throughput), both models provide basically the same results.

Impact of signal bandwidth In this section, we investigate the impact of the signal bandwidth in terms of the achievable throughput. Unlike the analysis conducted in Sect. 2.1.3, in which the signal bandwidth B is a function of the carrier frequency f_0 (in particular, according to Table 2, it represents 10% of the carrier frequency), here we consider a fixed bandwidth $B = 1$ GHz. For the sake of brevity, we only consider the case $x_u = 10$ m.

The numerical results are reported in Figs. 19 and 20. As can be seen, when considering a fixed bandwidth, we cannot benefit from the same compensation effect observed in Sect. 2.1.3 for what concerns the achievable throughput (in which the bandwidth occurs both in the noise power and in multiplying the logarithm of the SNR), and hence now the path loss is the dominating factor. For this reason, $t^{\mathrm{NF}}_{\mathrm{LoS}}$ decreases as f_0 increases (Figure 19(a)). Furthermore, choosing a lower B also affects the absolute values of the throughput (as can be seen, the maximum value is around 15 Gb/s, compared to more than 250 Gb/s when considering $B = 0.1 f_0$ in Figs. 14-15).

This reduced range of achievable throughputs is somewhat beneficial concerning the gap reported in Figure 20. However, the main conclusions drawn in Sect. 2.1.3 are still valid. Note also that analogous results, computed when using the FF approximation, achieve very similar performance, and are then omitted in the interest of space.

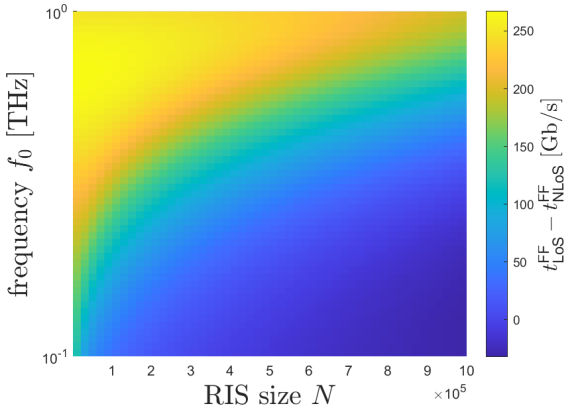

(a) $x_u = 5$ m.

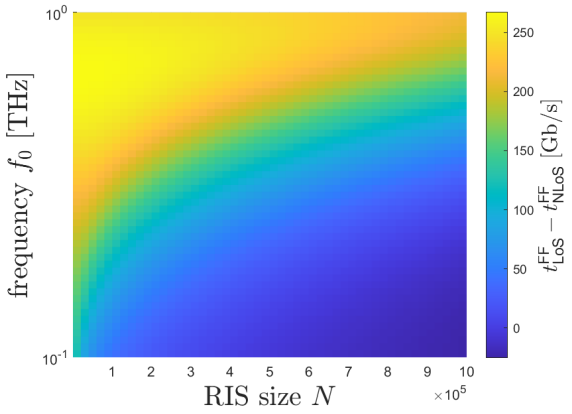

(b) $x_u = 10$ m.

Figure 18: Δ_t as a function of the carrier frequency f_0 and the RIS size N (far-field model, $d_0 = 20$ m, $\delta = 4$ m).

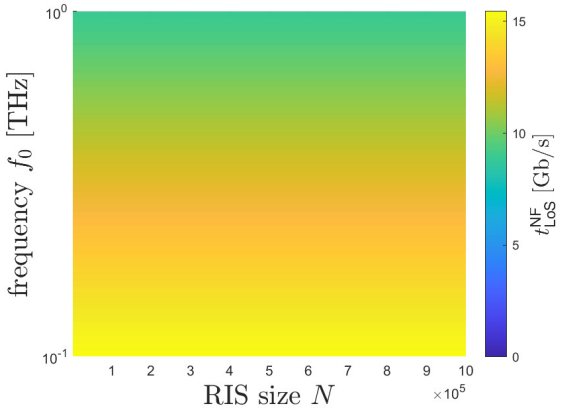

(a) LoS link.

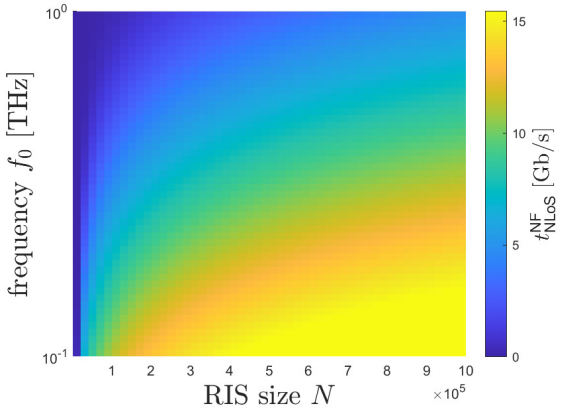

(b) NLoS link.

Figure 19: Throughput as a function of the carrier frequency f_0 and the RIS size N when $B = 1$ GHz (near-field model, $d_0 = 20$ m, $\delta = 4$ m, $x_u = 10$ m).

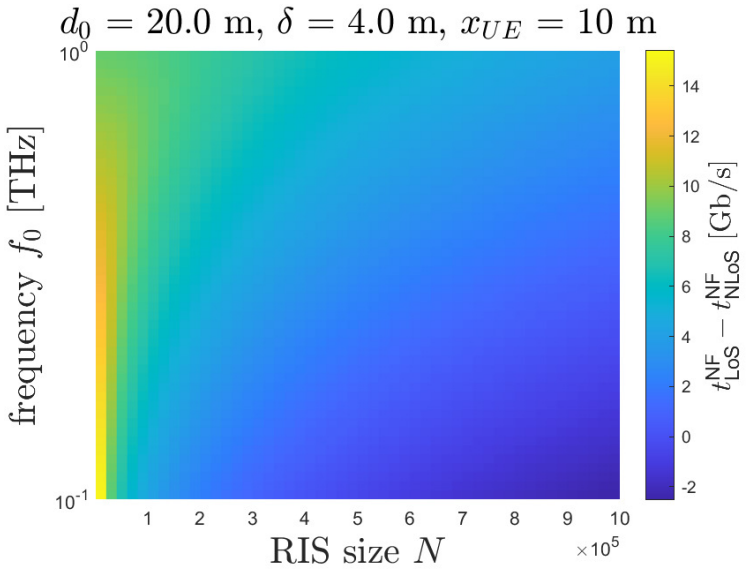

Figure 20: Δ_t as a function of the carrier frequency f_0 and the RIS size N when $B = 1$ GHz (near-field model, $d_0 = 20$ m, $\delta = 4$ m, $x_u = 10$ m).

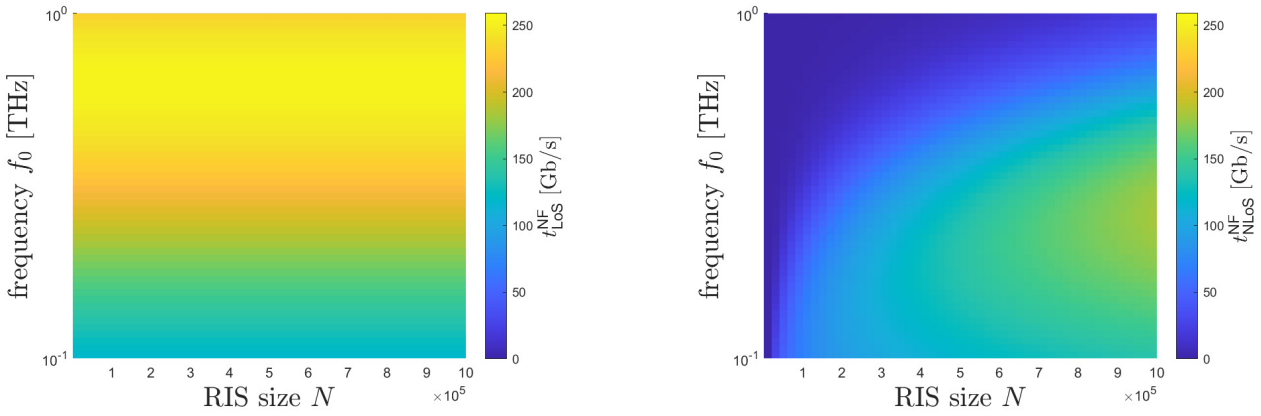

(a) LoS link.

(b) NLoS link.

Figure 21: Throughput as a function of the carrier frequency f_0 and the RIS size N when $h = 5$ m (near-field model, $d_0 = 20$ m, $\delta = 4$ m, $x_u = 10$ m).

Impact of RIS elevation In this section, we investigate the impact of the antenna elevation for both the RIS and the BS with respect to the UE plane. In particular, in accordance with [10], we consider $h = 5$ m. For the sake of brevity, we only consider the cases $x_u = 10$ m and $B = 0.1 f_0$.

The numerical results are reported in Figs. 21 and 22 (analogous results, computed when using the FF approximation, achieve very similar results, and are omitted in the interest of space). As can be seen by comparing these plots with Figs. 16-17, when elevating the RIS and the BS, the situation gets worse, due to two concurrent reasons: not only the RIS-UE distance increases, but also the directivity of the array is reduced, thus decreasing the array gain towards the UE. As a conclusion, the findings outlined in Sect. 2.1.3 still apply, with some worsening in terms of the necessary number of radiating elements N. Hence, specific attention must be paid when dimensioning the scenario of application.

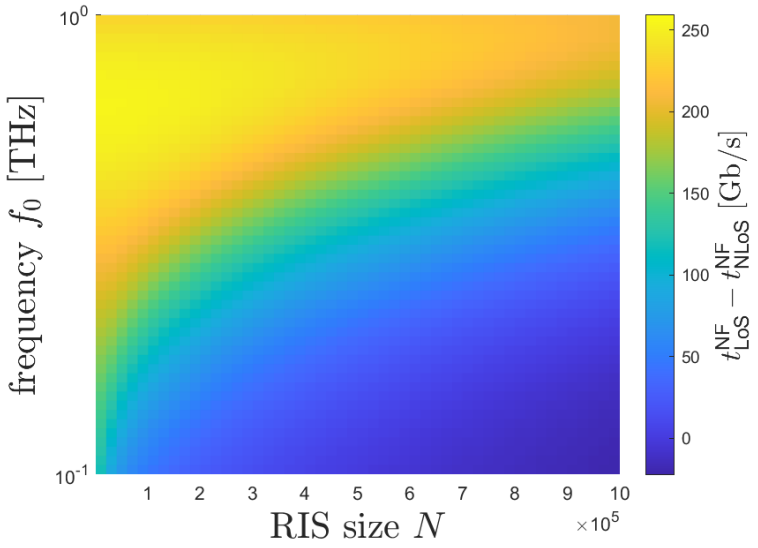

Figure 22: Δ_t as a function of the carrier frequency f_0 and the RIS size N when $h = 5$ m (near-field model, $d_0 = 20$ m, $\delta = 4$ m, $x_u = 10$ m).

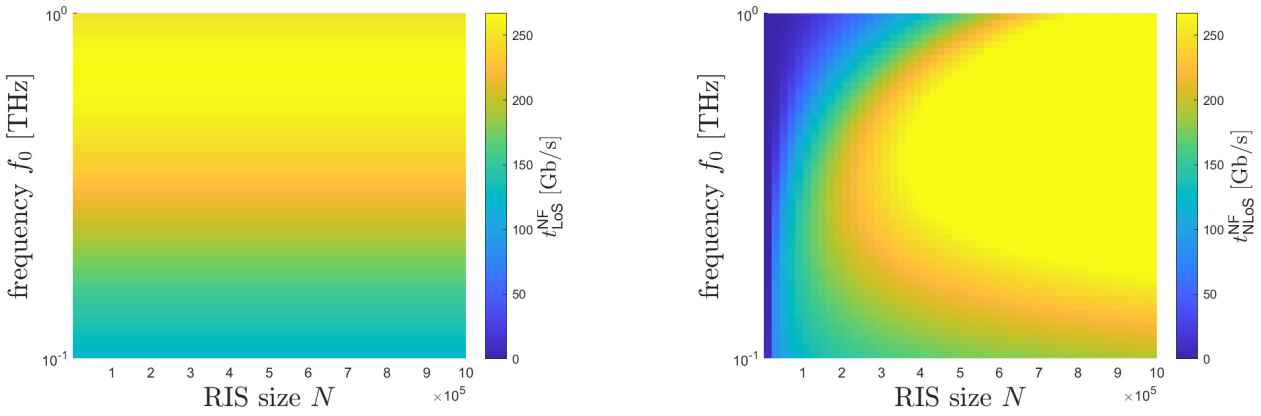

(a) LoS link.

(b) NLoS link.

Figure 23: Throughput as a function of the carrier frequency f_0 and the RIS size N when $\Gamma_{\mathrm{NLoS}} = \Gamma_{\mathrm{LoS}} = 55$ dBi (near-field model, $d_0 = 20$ m, $\delta = 4$ m, $x_u = 10$ m).

Impact of antenna gain In this section, we investigate the impact of the antenna gain Γ_{NLoS} in the BS-RIS link (compared to the antenna gain Γ_{LoS} in the BS-UE link). For the sake of brevity, we only consider the cases $x_u = 10$ m and $B = 0.1 f_0$.

The numerical results are reported in Figs. 23 and 24 (analogous results, computed when using the FF approximation, achieve very similar results, and are omitted in the interest of space). As can be seen by comparing these plots with Figs. 16-17, and as widely expected, when increasing Γ_{NLoS} the situation is significantly better. In particular, Figure 23 shows that the maximum value is achieved when a significantly lower number of elements N is used. This is reflected in Figure 24, which significantly improved the conclusions drawn in Sect. 2.1.3.

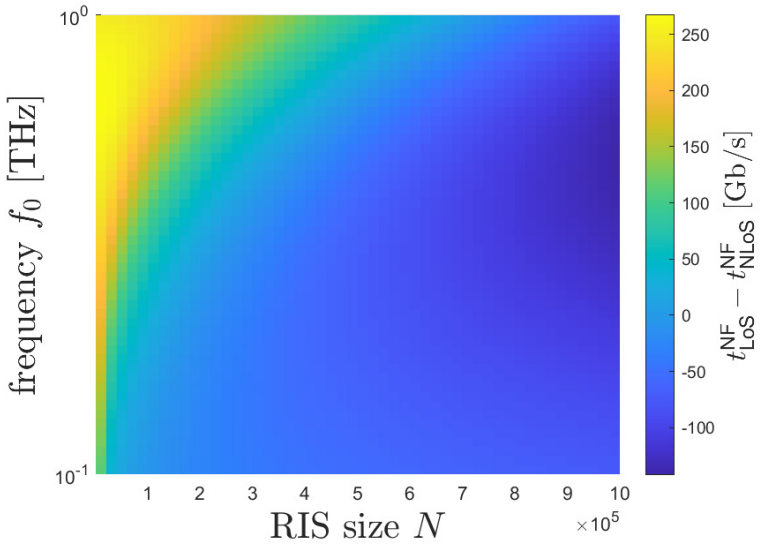

Figure 24: Δ_t as a function of the carrier frequency f_0 and the RIS size N when $\Gamma_{NLoS} = \Gamma_{LoS} = 55$ dBi (near-field model, $d_0 = 20$ m, $\delta = 4$ m, $x_u = 10$ m).

2.1.4 Discussion

From the numerical analysis conducted above, we can summarize the following trends. In particular, by looking at the channel gains, we can conclude as follows:

- for a given scenario (in particular, distances d_0 and δ), N increases as f_0 increases; this holds true for both the exact (NF) and the approximated (FF) models, and the difference (in terms of N) across the two models increases as f_0 increases (with the FF model over-estimating N);
- for a given scenario (in particular, distances d_0 and x_u), the distance δ that minimizes N does not depend on f_0, while it depends on d_0, so as to balance the effects of path loss directivity of the array at the RIS; in particular, a symmetric situation ($x_u = d_0/2$) yields the minimum N;
- for reasonable values of d_0, δ, and x_u, the required N exceeds several tens of thousands elements, even for f_0 taken in the lower range of THz communications (i.e., $f_0 = 0.1$ THz).

Looking at the throughput, and considering at least $100,000$ radiating elements, we can derive the following trends:

- when increasing f_0 and/or decreasing N, the gap between direct (LoS) and indirect, RIS-assisted, link (with blockage) increases, without significant differences between the exact (NF) and the approximated (FF) models, and with a limited impact given by the RIS height (only with a small decrease in the performance, due to an increased path loss and a reduced directivity);
- the most crucial parameters, in order to achieve significant performance and to limit the penalty gap between direct and indirect links, are represented by the antenna gains at the BS and the RIS; in particular, if the gap is significant, then the RIS-assisted communication suffers from a substantial penalty gap; however, for medium-range gaps of the antenna gains, the RIS-assisted configuration is able to guarantee some connectivity in case of complete blockage of the direct link.

2.2 LoS-MIMO capacity evaluations in RIS-enhanced factory environments

When operating in the near-field using multiple antenna systems, the spherical model of wave propagation enables the creation of independent channel paths, rendering the corresponding MIMO matrix to have a rank larger than one. This phenomenon can be effectively used for facilitating spatial multiplexing transmission to a single user to increase its communication capacity. In RIS-enhanced environments, where the link between a BS and a UE is established through the reflection of a LoS path via a RIS, the size of the RIS effectively determines the level of spatial multiplexing that can be supported for this link. Transmitter and Receiver both need to be equipped with multiple antennas to allow for the separation of the spatially multiplexed beams and for precisely shaping the beam direction towards the RIS. The solution for beam design and configuration of the RIS weights to enable spatial multiplexing in RIS-enhanced communication links has been proposed in [13]. In this section, we will reuse the approach proposed therein and study the achievable capacity of a UE moving through a factory hall and being served by a BS through a RIS-enhanced communication link. After evaluating the capacity for different RIS deployments assuming ideal conditions (i.e., continuous phase shifts for the RIS weights, ideal channel knowledge), we then investigate the effect of discrete levels for the phase shift at the RIS weights as well as the effect of UE displacements by small offsets yielding channel mismatches.

2.2.1 Evaluation scenario and system model

The scenario under study is depicted in Fig. 25. A cuboid factory hall is assumed of width $W = 20$ m, length $L = 30$ m and height $H = 10$ m. The (x, y, z) coordinate system is defined as shown in the figure with its origin in the (lower) top left corner of the hall. The BS is mounted at a height $h = 8$ m, i.e., 2 meters below the ceiling, in the centre of the hall at coordinates $(15, 10, 8)$. Two RIS are mounted to the left wall at height $h = 4$ m with equal distance d to the x-coordinate of the BS, given by the coordinates $(15 \pm d, 0, 4)$. Finally, a UE with height $h = 1$ m centered in the hall moves along the x-axis from one end of the hall to the other, i.e., $(x, 10, 1)$ with $x \in [0, 30]$. BS, UE and RIS are assumed to use a uniform planar array (UPA), which is centered at the respective location of the communication node. The orientation of all UPAs is perpendicular to the y/z plane; while the UPAs at the RIS as planar with the wall they are mounted at, the UPAs at BS and UE are assumed to be tilted by 45° towards the RIS.

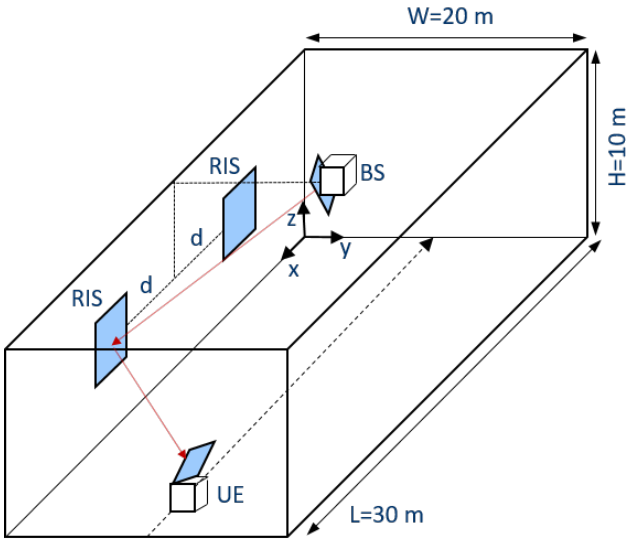

Figure 25: RIS-enhanced deployment scenario in factory hall

The UE is served by LoS links via the right RIS (seen from the BS perspective) as long as it moves along the x-axis in the range $x \in [0, 15]$, while it is served via the left RIS thereafter, $x \in [15, 30]$. As the transmitter at the BS is assumed to be capable of forming precisely shaped beams towards the RIS, possible interference

created by the other RIS during serving the UE via the selected RIS is considered to be negligible (though this is considered to be studied in future work). The near-field channels between RIS and BS and RIS and UE, respectively, are modelled according to the free-space propagation model, yielding for channel coefficient between the n-th RIS element and the k-th element at the BS (or UE, respectively):

$$h_{nk} = \frac{\lambda}{4\pi d_{nk}} \exp\left(j\frac{2\pi}{\lambda} d_{nk}\right) \tag{36}$$

with d_{nk} the distance between antenna element n at the RIS and k at the BS/UE. For calculating the capacity achievable by spatial multiplexing over the RIS-enhanced LoS channels, we reuse the solution proposed in [13]. Therein, the authors have shown that the RIS weights w_n achieving the capacity of the LoS-MIMO channel are obtained for each RIS element n by the product of the two phase factors representing the average phase shift between the RIS element and the BS and between the RIS element and the UE, respectively:

$$w_n = \exp\left(j\frac{2\pi}{\lambda} d_n^{UE}\right) \cdot \exp\left(-j\frac{2\pi}{\lambda} d_n^{BS}\right) \tag{37}$$

These average phase shifts are derived from the free-space propagation model for the distance between the n-th RIS element and the center point of the UPA at BS (or UE, respectively). These RIS weights can be stacked into a diagonal (unitary) matrix $\mathbf{\Phi}$ of dimension $N \times N$, with N being the total number of RIS elements. Similarly, by stacking the channel coefficients for the BS-RIS link into a $N \times K$ matrix $\mathbf{H}_B$ and those for the RIS-UE link into a $K \times N$ matrix $\mathbf{H}_U$, the effective channel for the RIS-enhanced link can be given as

$$\mathbf{H}_{eff} = \mathbf{H}_U \mathbf{\Phi} \mathbf{H}_B \tag{38}$$

Since this effective channel has a rank larger one when BS and UE are in the near-field of RIS, it is well known that the optimum transmission scheme is the singular value decomposition (SVD)-based precoding, which enables to use the Eigenchannels for transmission. The authors in [13] have shown that the left and right singular vectors of $\mathbf{H}_{eff}$ to be used as the pre- and decoders for Eigenchannel transmission are identical to the left singular vector of $\mathbf{H}_U$ and the right singular vector of $\mathbf{H}_B$, respectively. Further, they have shown that the Eigenchannels of $\mathbf{H}_{eff}$ are identical to the product of the Eigenchannels of $\mathbf{H}_U$ and $\mathbf{H}_B$.

To achieve the maximum capacity C, optimal power distribution over the Eigenchannels of $\mathbf{H}_{eff}$ according to the Waterfilling algorithm is mandated. However, the authors have further shown that, as long as the magnitudes of the Eigenchannels σ_i of the L channels selected for transmission, $i \in \{1, \dots, L\}$, do not differ by a factor larger than 10, the difference to the much simpler equal power allocation scheme is insignificant. For the capacity evaluations carried out here, we have therefore selected the number of Eigenchannels achieving the highest capacity under the equal power allocation scheme, where the above requirement could be safely fulfilled:

$$C = \max_L \sum_{i=1}^{L} \log\left(1 + \frac{P_0}{LN_0}\sigma_i^2\right), \tag{39}$$

where P_0 and N_0 is the transmit power and noise power, respectively.

2.2.2 Results

The system evaluation is carried out for a carrier frequency $f = 120$ GHz, yielding a wavelength $\lambda = 2.5$ mm. The assumed bandwidth is $B = 10^8$ Hz = 100 MHz, which leads to a noise power $N_0 = -174 + 80 = -94$ dBm. The transmit power is set to $P_0 = 20$ dBm. At the BS and the UE, an UPA with 8×8 antennas is assumed with an antenna spacing of 8λ, while the RIS is assumed to have an UPA with 64×64 RIS elements with a spacing of 2λ. Note that the choice of these parameters, which differ from the ones used in Sect. 2.1, is mainly due to complexity issues. As a matter of fact, reducing the spacing between the elements increases the RIS size, without achieving a significant benefit in terms of performance. A different consideration can be drawn for the selected bandwidth: increasing the bandwidth increases the noise power, and thus reduces the SNR for a given signal power budget, thus reducing the possibility to activate additional eigenchannels (and thus limiting the performance).

Capacity evaluation results for the UE moving along the x-axis in the center of the factory hall are shown in Fig. 26 (a). As the baseline scenario, a direct communication between BS and UE (i.e, without RIS enhancements) is considered, where the tilting of the UPAs at BS and UE is set to 90° (i.e., parallel to the ceiling) to align their orientation with the direct LoS link between the two. In this case, the channel matrix for this LoS link has only one usable Eigenchannel, and the corresponding plot in the figure exhibits the lowest capacity. When the RIS-enhanced deployment is considered, a significant boost of the capacity can be observed, which reaches gains up to 50% compared to the baseline. This capacity boost is attributed to a substantially increased number of usable Eigenchannels in the LoS-MIMO link, as shown in Fig. 26 (b), where it is seen that up to 5 Eigenchannels will be used. The different placements of the RIS considered in Fig. 26, characterized by the distance d to the BS, reveal that by placing the RIS close to the BS, a high capacity – supported by a large number of used Eigenchannels – can be achieved close to the center of the hall, while it drops steeply when the UE moves towards the corners. Opposed to that, a placement of the RIS further away from the BS exhibits a more balanced capacity distribution in the factory hall, which is supported by a constant number of Eigenchannels used; the average capacity is significantly lowered compared to the former case, though.

For further evaluations, the RIS placement is fixed to $d = 3$ m. The focus is now turned on the sensitivity of the Eigenvectors used for beamforming at UE and BS with respect to UE displacements in x, y and z direction. In particular, it is assumed that these beamformers are determined as the left singular vectors $\mathbf{u}_i$ of the channel $\mathbf{H}_U$ between RIS and the UE located at a pre-defined position, but the actual channel $\hat{\mathbf{H}}_U$ used for transmission is then calculated for the UE position with an offset in x, y or z direction. Since the beamformers at the BS are determined as the right singular vectors $\mathbf{v}_i$ of the channel $\mathbf{H}_B$ between RIS and BS, these are not affected by the UE displacement. The effective channel thus becomes

$$\hat{\mathbf{H}}_{eff} = \hat{\mathbf{H}}_U \mathbf{\Phi} \mathbf{H}_B \,. \tag{40}$$

The useful signal power P_i of the i-th Eigenchannel and the interference power Z_i of the other Eigenchannels distorting the i-th Eigenchannel then amount to

$$P_i = P_0/L \, ||\mathbf{u}_i^H \hat{\mathbf{H}}_{eff} \mathbf{v}_i||^2 \tag{41}$$

$$Z_i = P_0/L \sum_{j=1, j\neq i}^{L} ||\mathbf{u}_i^H \hat{\mathbf{H}}_{eff} \mathbf{v}_j||^2 \,. \tag{42}$$

The SINR for the i-th Eigenchannel then yields $\frac{P_i}{Z_i+N_0}$, which allows to calculate the capacity achievable under UE displacement according to

$$C_{\text{displacement}} = \sum_{i=1}^{L} \log\left(1 + \frac{P_i}{Z_i + N_0}\right) \,. \tag{43}$$

The drop in capacity for UE displacements of different offsets is shown in Fig. 27 (a). We have investigated displacements in x, y and z direction by an offset of 2 cm $= 8\lambda$ and 5 cm $= 20\lambda$, respectively. It is observed that the lowest sensitivity is for offsets in the y-direction, which is the direction perpendicular to the RIS. The sensitivity for offsets in x and z direction, i.e. parallel to the RIS surface, is significantly more pronounced, though: It is observed that a displacement of 5 cm in x-direction yields a capacity drop by 20% close to the edges and by 50% in the worst case. The strongest capacity drop is observed at the x-positions of the RIS (x=12 m and x=18 m), where the LoS link between UE and RIS link is closest to the RIS' perpendicular. Moreover, we observe from the plots that the most pronounced drops in capacity appear in the region with the highest number of Eigenchannels used; compare with Fig. 26 (b). Hence, we also plotted for the maximum displacement considered the case where the total number of Eigenchannels (EC) is limited to 3. From those plots, it can be observed that the capacity drops smooth out considerably, which suggests that reducing the number of Eigenchannels in case of larger expected displacement is a useful approach to alleviate the induced capacity drop.

Finally, we investigated the effect of 2-bit quantized RIS weights in matrix $\mathbf{\Phi}$, as shown in 27 (b). We focused on the capacity performance in an ideal setting (i.e., no offsets) and to those with offsets in x-direction, taken from Fig. 27 (a). The figure reveals that by quantizing the RIS weights with 2-bit, the capacity drops by roughly

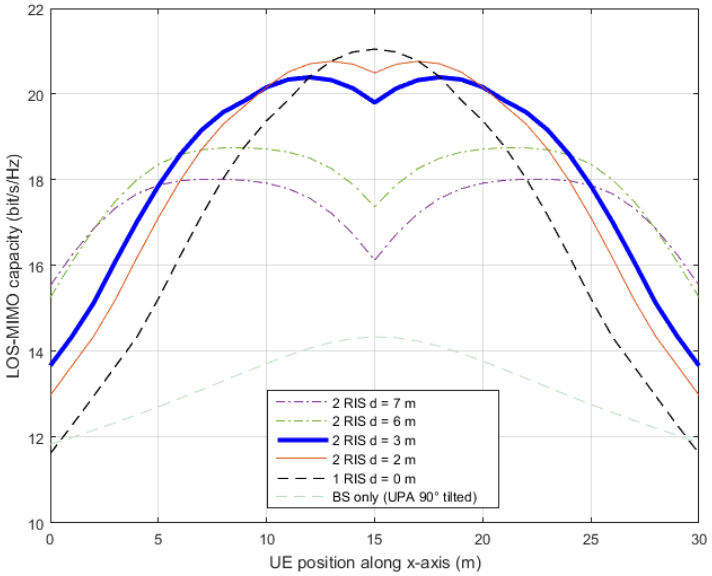

(a) LoS-MIMO capacity

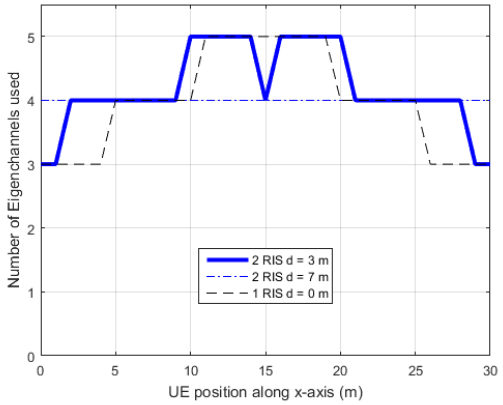

(b) Number of used Eigenchannels

Figure 26: (a) LoS-MIMO capacity and (b) number of used Eigenchannels vs. UE position for different RIS placements.

6%, irrespective of the considered offsets. In line with existing results from the literature for RIS-enhanced communications, it can be confirmed that a 2-bit quantization is a pragmatic choice also for high-rank LoS-MIMO communications, allowing for a favourable cost-benefit trade-off.

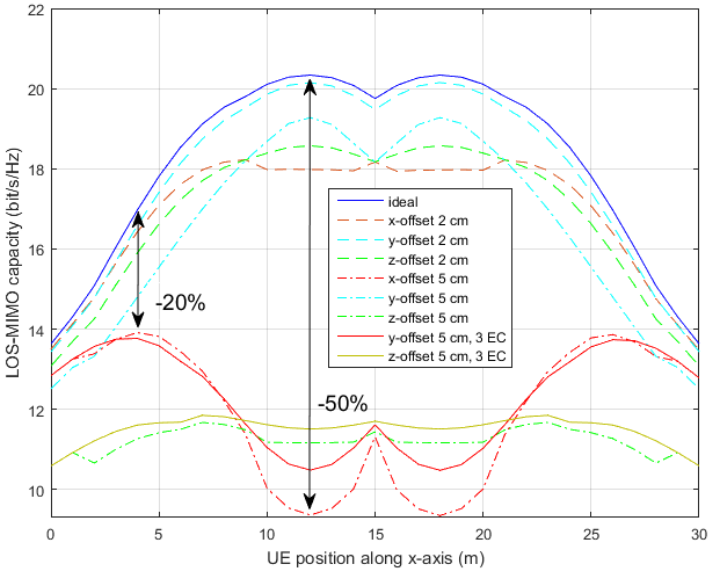

(a) Offsets in x, y, z direction

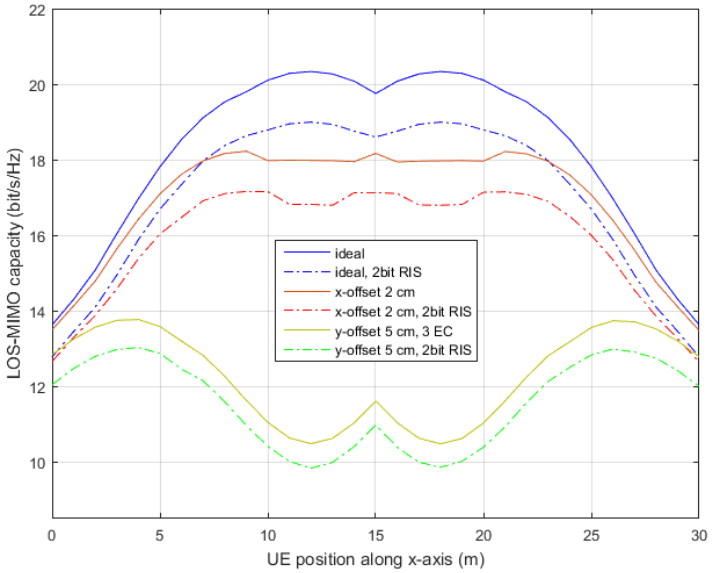

(b) 2-bit quantized RIS weights

Figure 27: Drop in capacity due to (a) UE displacements given as offsets in x, y and z direction and (b) quantization of RIS weights.

2.3 Impact of RF impairments on RIS-based communication links

When operating at higher frequencies such as the sub-THz band, the effective channel loss imposes a challenge to design high throughput, stable and reliable communication links. Towards this goal, directional beamforming can assist in alleviating some of the channel induced losses. However, if high gain directional antennas are deployed, an established communication link becomes sensitive to blockage, where in such cases, communication link outage is inevitable, and an alternative path can assist in re-establishing the communication link. RIS has attracted the attention of the community due its potential in improving the network coverage. RISs are comprised of several reflecting elements where the phase of each of the reflecting elements is adjustable. Once the phase shifts induced by the effective channel are known, the phases of each of the RIS elements are tuned such that the reflected signal components are coherently combined at the receiver. The challenge in this approach is the accurate tuning of the phases for the establishment of the coherent combining scenario at the receiver. To account for this challenge, phase errors are included in the modeling of the RISs, which introduces a communication performance degradation. There are multiple sources of the phase errors, such as non-continuous phase shifting capabilities of the RIS elements, or imperfect effective channel phase estimates.

Hereafter, we attempt to quantify the performance of a RIS assisted communication link when the RIS elements are impaired by phase errors. We analyze two performance metrics, the average SNR and the spectral efficiency and highlight the functional dependency of these metrics on the phase errors.

2.3.1 System Model

To demonstrate the impact of the phase errors by the RIS elements, we begin by modeling an overall received signal r resulting from a communication link between Nodes A and B through a RIS. When there is no direct link between nodes A and B, r may be written as

$$r = \sqrt{\alpha P} \sum_{n=1}^{Q} h_{r,n} e^{j\theta_n} h_{t,n} x + v, \tag{44}$$

where Q is the total number of RIS elements, $h_{r,n}$ and $h_{t,n}$ represent the complex channel coefficient form the RIS to the receiver and the transmitter to the RIS, respectively, θ_n represents the phase shift induced by the n^{th} RIS element, v represents the additive white Gaussian noise (AWGN) at the receiver, x is the transmitted data symbol which modeled as a complex circularly symmetric Gaussian random variable with zero mean and unity variance, and P is the transmitter power. Finally, α is the overall path gain between node A and B which was derived in [14] and may be written as

$$\alpha = \frac{G_A G_B}{(4\pi)^2} \left(\frac{lw}{d_{AR} d_{RB}} \right)^2 \cos(\psi), \tag{45}$$

where l, w are the length and width of the reflecting element at the RIS, d_{AR} and d_{RB} are the separation distances between Node A and the RIS, and the RIS and Node B, respectively, G_A and G_B represent the gains of the transmitter and receiver antennas, respectively, and ψ is the angle of incidence of the reflecting wave. Table 3 summarizes the adopted parameters.

2.3.2 Phase Errors at the RIS

In this section, we focus on the modeling of phase errors at the RIS, and the near-field/far-field channel modeling distinction is dismissed to focus on the effects of phase errors. Let $h_{t,n} = e^{j\phi_{t,n}}$, and $h_{n,r} = e^{j\phi_{n,r}}$. Then, the phase of the RIS should be tuned such that

$$\theta_n = -(\phi_{n,t} + \phi_{n,r}). \tag{46}$$

Table 3: List of parameters used throughout this section.

Symbol	Meaning
α	Channel path gain
$h_{n,t}$	Channel coefficient of the n^{th} Node A-to-RIS channel link
$h_{n,r}$	Channel coefficient of the n^{th} RIS-to-Node B channel link
$\phi_{n,t}$	Phase of the n^{th} Tx-to-RIS channel link
$\phi_{n,r}$	Phase of the n^{th} RIS-to-Rx channel link
Q	Number of RIS reflecting elements
x	Tx symbol
v	AWGN
ϵ_n	Phase error of the n^{th} RIS element
θ_n	Phase of the n^{th} RIS element

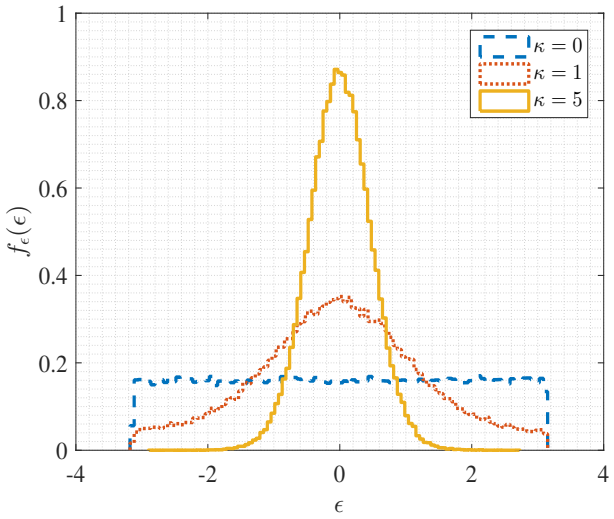

Figure 28: Von Mises PDFs for different values of κ over the interval $[-\pi, \pi]$.

However, this is generally challenging to design, and thus, we get

$$\theta_n + \phi_{n,t} + \phi_{n,r} = \epsilon_n, \tag{47}$$

where ϵ_n is the phase error. To model the phase error, a statistical approach using a generalized distribution is adopted. The Von Mises distribution is adopted to model $\epsilon_n \; \forall n \in \{0, \dots, Q-1\}$, where it is modeled as an i.i.d zero-mean Von-Mises random variable with consternation parameter κ and a probability density function that may be written as [15]

$$f_\epsilon(y) = \frac{e^{\kappa \cos(y)}}{2\pi I_0(\kappa)}, \quad -\pi < y < \pi \tag{48}$$

where $I_0(.)$ is the zero-th order modified Bessel function of the first kind defined in [16, 9.6.19]. To demonstrate the effect of the concentration parameter κ, Fig. 28 shows the effect of varying κ on the probability density function (PDF) defined in (48). Is is shown that as κ is increased, the distribution of the Von Mises random variable becomes more concentrated around zero.

2.3.3 Performance Evaluation

In this section we compute the average SNR metric to quantify the impact of phase errors at the RIS on the communication link performance. The SNR may be written as

$$\gamma \triangleq \frac{\alpha P \left| \sum_{n=1}^{Q} e^{j\epsilon_n} \right|^2}{\sigma_v^2}, \tag{49}$$

where σ_z^2 is the variance of the AWGN. To solve the expectation, we apply

$$\begin{aligned}\mathbb{E}_\epsilon\left\{\left|\sum_{i=1}^{Q} e^{j\epsilon_i}\right|^2\right\} &= \mathbb{E}_\epsilon\left\{\left(\sum_{i=1}^{Q}\cos\left(\epsilon_i\right)\right)^2+\left(\sum_{i=1}^{Q}\sin\left(\epsilon_i\right)\right)^2\right\},\\ &= Q+\sum_{i=1}^{Q}\mathbb{E}_\epsilon\left\{\cos(2\epsilon_i)\right\}-\sum_{i=1}^{Q}\mathbb{E}_\epsilon\left\{\cos(2\epsilon_i)\right\}\\ &+\sum_{n=1}^{Q}\sum_{\substack{m=1\\m\neq n}}^{Q}\mathbb{E}_\epsilon\left\{\cos(\epsilon_n)\right\}\mathbb{E}_\epsilon\left\{\cos(\epsilon_m)\right\}+\sum_{n=1}^{Q}\sum_{\substack{m=1\\m\neq n}}^{Q}\mathbb{E}_\epsilon\left\{\sin(\epsilon_n)\right\}\mathbb{E}_\epsilon\left\{\sin(\epsilon_m)\right\}. \end{aligned} \tag{50}$$

To solve the above, we need to calculate $\mathbb{E}_\epsilon\left\{\cos(\epsilon_m)\right\}$ and $\mathbb{E}_\epsilon\left\{\sin(\epsilon_m)\right\}$. Starting with the latter, we apply

$$\mathbb{E}_\epsilon\left\{\sin(\epsilon_m)\right\}=\int_{-\pi}^{\pi}\sin(x)\frac{e^{\kappa\cos(x)}}{2\pi I_0(\kappa)}\mathrm{d}x=0, \tag{51}$$

where the above result is due to the fact that the integrand is and odd function around zero in the integral interval. Regarding $\mathbb{E}_\epsilon\left\{\cos(\epsilon_m)\right\}$, one can write

$$\begin{aligned}\mathbb{E}_\epsilon\left\{\cos(\epsilon_m)\right\} &= \int_{-\pi}^{\pi}\cos(x)\frac{e^{\kappa\cos(x)}}{2\pi I_0(\kappa)}\mathrm{d}x,\\ &= \frac{1}{2\pi I_0(\kappa)}\left(\int_{-\pi}^{0}\cos(x)e^{\kappa\cos(x)}\mathrm{d}x+\int_{0}^{\pi}\cos(x)e^{\kappa\cos(x)}\mathrm{d}x\right)=\frac{I_1(\kappa)}{I_0(\kappa)}. \end{aligned} \tag{52}$$

where $I_0(\kappa)$ and $I_1(\kappa)$ are the modified Bessel functions of the first kind of orders zero and one, respectively, defined in [16, 9.6.19]. Plugging (52) and (51) in (50) and the (49) yields

$$\mathbb{E}_\epsilon\{\gamma\}=\frac{\alpha PQ}{\sigma_v^2}\left(1+(Q-1)\left(\frac{I_1(\kappa)}{I_0(\kappa)}\right)^2\right). \tag{53}$$

Let us take a closer at (53). For $0\leq\kappa<1$, one can approximate (53) with

$$\mathbb{E}_\epsilon\{\gamma\}\overset{0\leq\kappa<1}{\approx}\bar{\gamma}\left(1+\frac{(Q-1)}{4}\kappa^2\right), \tag{54}$$

where $\bar{\gamma}=\frac{\alpha PQ}{\sigma_v^2}$. This can be easily deduced from using the first term of the series expansion of $I_\nu(z)$, i.e.

$$I_\nu(z)=\sum_{n=0}^{\infty}\frac{\left(\frac{z}{2}\right)^{2n+\nu}}{n!\Gamma(\nu+n+1)}, \tag{55}$$

where $\Gamma(.)$ is the Gamma function [16, 6.1.1]. Plugging in the approximations $I_0(\kappa)=1+\mathcal{O}(\kappa^2)$ and $I_1(\kappa)=\frac{\kappa}{2}+\mathcal{O}(\kappa^3)$ for the range $0\leq\kappa<1$ yields (54). For $\kappa\to\infty$, one can write

$$\mathbb{E}_\epsilon\{\gamma\}\overset{\kappa\to\infty}{\approx}\frac{\alpha PQ^2}{\sigma_v^2}, \tag{56}$$

which is deduced by using the property $\frac{I_1(\kappa)}{I_0(\kappa)}\to 1$ as $\kappa\to\infty$. This result demonstrates that the SNR no longer depends on any of the impairments parameters. We can further deduce from this result that when $\kappa=0$, i.e. a worst-case scenario in the sense that $\epsilon_i\sim\mathcal{U}[-\pi,\pi]$, the average SNR grows linearly with Q as observed from the following relation

$$\mathbb{E}_\epsilon\{\gamma\}\overset{\kappa\to 0}{\approx}\frac{\alpha PQ}{\sigma_v^2}, \tag{57}$$

Table 4: Simulation parameters.

Parameter	Value
d_{AR}	10m
d_{RB}	10m
f_c	300 GHz
G_A	30 dB
G_B	30 dB
l	$\lambda/2$
P/σ_v^2	40 dB
ψ	30°
Q	2^{20}
w	$\lambda/2$

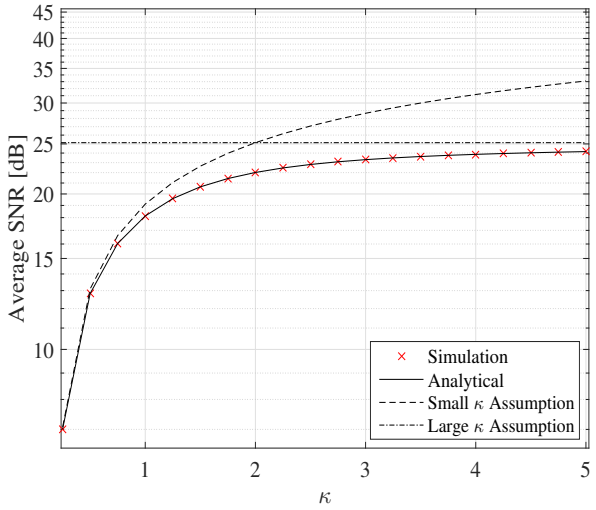

Figure 29: Average SNR vs. κ. Approximations of small κ (54), large κ (56), and the analytical solution in (53) are compared with simulations.

where the result was deduced using the equality $I_1(0) = 0$. Comparing (54) and (56), one can notice that depending on the severity of the phase error distribution, i.e. the concentration parameter κ, the average SNR goes from depending on the square of the number of reflecting elements Q for high κ to depending linearly on Q for low κ.

In Fig. 29, we depict the performance of the average SNR as a function of the concentration parameter κ. The derived approximations of small κ in (54), large κ in (56), and the analytical solution in (53) are compared with simulations. Table 4 presents the adopted simulation parameters. The analytical and simulation results match for different values of κ, and the simple approximations are shown to be accurate once the approximation conditions are met.

Although adopting higher frequencies allows for the exploitation of large bandwidths, devices adopting THz frequencies are practically limited by the supported modulation order due to hardware limitations. Thus, hereafter, we investigate the effect of phase errors at the RIS on the spectral efficiency of a RIS-assisted THz communication link. Using Jensen's inequality, the spectral efficiency (ζ) can be upper bounded as

$$\begin{aligned}\zeta &\leq \log_2(1+\mathbb{E}_\epsilon\{\gamma\}),\\ &= \log_2\left(1+\frac{\alpha PQ}{\sigma_v^2}\left(1+(Q-1)\left(\frac{I_1(\kappa)}{I_0(\kappa)}\right)^2\right)\right).\end{aligned} \tag{58}$$

To consider the effect of the modulation order, we adopt the BER approximation of M-QAM two-dimensional gray coding over AWGN channels [17], which presents an upper bound for $M \geq 4$ and BER$\leq 10^{-2}$ [18]. Using Jensen's inequality, the spectral efficiency may be upper-bounded by the following expression

$$\begin{aligned}\zeta_M &= \log_2(M),\\ &\leq \log_2\left(1+\frac{3\frac{\alpha PQ}{\sigma_v^2}\left(1+(Q-1)\left(\frac{I_1(\kappa)}{I_0(\kappa)}\right)^2\right)}{-2\ln(5\text{BER}_0)}\right),\end{aligned} \tag{59}$$

where BER_0 is a fixed target BER.

Fig. 30 depicts the performance of ζ_M as a function of κ. As a benchmark, ζ_M is computed using the approximation in (56). As the results show, different modulation orders are selected for different concentration parameter values. Generally, as κ is increased, a higher modulation order can be supported. In more details, for $\kappa \lessapprox 0.25$, no QAM transmission could be supported, while for $\kappa \gtrapprox 4.5$, a maximum modulation order of 128-QAM can be supported. The result hence shows that phase errors at the RIS can highly impact the performance of the spectral efficiency and the choice of the modulation order.

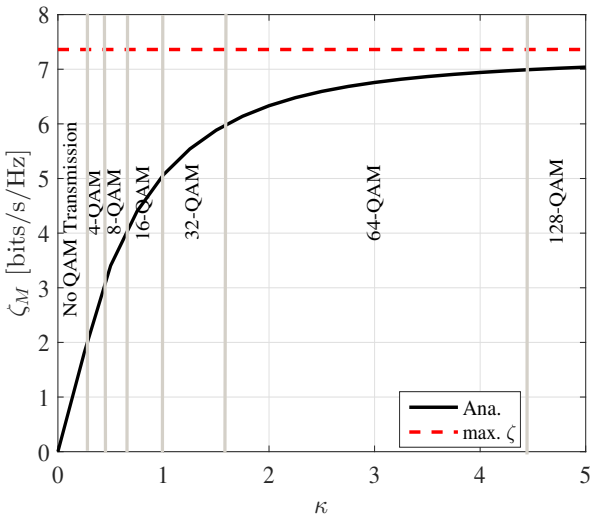

Figure 30: ζ_M (Eq. (59)) vs. κ. ζ using (56) is shown as a reference.

2.4 Low-complexity beamsteering for THz communications using frequency-selective Metasurfaces

RISs have received particular attention in recent years, however, they possess two main disadvantages that could make them not appealing in many applications, especially when working at THz frequencies: i) real-time reconfigurable hardware must be implemented at the cell level. This could be challenging at THz because of the small wavelength and high number of cells; ii) Dedicated interfaces are required to control the RIS with consequent issues in terms of signaling overhead and coordination with the BS; iii) Power supply is needed.

2.4.1 Frequency-selective metasurfaces (Metaprisms)

To cope with these issues, here we consider the concept of *metaprism*, i.e., a static Frequency Selective Surface (FSS) [19]. The metaprism is not reconfigurable so different reflection behaviours are obtained by modifying the spectral characteristics of the impinging signal. The frequency selectivity behavior of the surface can be realized by a proper design of load impedance at each cell/element, as done in [19–21]. In the past FSSs were exploited for selectively suppressing interference from non-selected frequency EM waves and providing signal gain [22–24]. For example, FSS can be appropriately deployed around the antenna to achieve selectivity enhancement or suppression of electromagnetic waves in a specific frequency range [25].

Figure 31 shows a metaprism situated in the x-y plane with its center at coordinates $\mathbf{p}_0 = (0,0,0)$. This metaprism comprises $N \times M$ cells, each with dimensions $dx \times dy$, arranged in a grid pattern. The coordinates of these cells are defined as $p_{nm} = (x_n, y_m, 0)$, where $x_n = n \cdot dx - \frac{N \cdot dx}{2}$ and $y_m = m \cdot dy - \frac{M \cdot dy}{2}$, with n and m ranging from 0 to $N-1$ and 0 to $M-1$, respectively. The total surface area is $L_x \times L_y$, where $L_x = N \cdot dx$ and $L_y = M \cdot dy$. Typically, the cell dimensions dx and dy in the x and y directions are smaller than the wavelength λ and here are assumed to be $\lambda/2$.

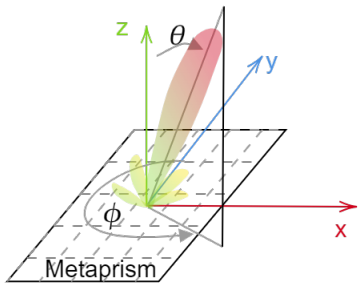

Figure 31: Geometry considered for the frequency selective surface.

A generalized equivalent model of the nm-th cell of the metaprism positioned at $\mathbf{p}_{nm}$ is depicted in Figure 32. This model comprises a radiation element (antenna) situated above a ground screen loaded with a cell-specific and frequency-dependent impedance $Z_{nm}(f)$, where n and m vary from 0 to $N-1$ and 0 to $M-1$, respectively, and f represents the frequency. The impedance is intentionally mismatched with respect to the antenna impedance Z_0, resulting in the generation of a reflected wave that is emitted back by the radiation element. The corresponding frequency-dependent reflection coefficient, when subjected to an incident plane wave with a 3D angle $\Theta_{\text{inc}} = (\theta_{\text{inc}}, \phi_{\text{inc}})$ and observed at angle $\Theta = (\theta, \phi)$, is denoted as $r_{nm}(\Theta_{\text{inc}}, \Theta; f)$ and is expressed as:

$$r_{nm}(\Theta_{\text{inc}}, \Theta; f) = F(\Theta_{\text{inc}})F(\Theta)G_c\Gamma_{nm}(f) = \beta_{nm}(\Theta_{\text{inc}}, \Theta; f)e^{j\psi_{nm}(f)}. \quad (60)$$

Here, $F(\Theta)$ represents the normalized power radiation pattern, accounting for the potential non-isotropic behavior of the radiation element, which is assumed to be frequency-independent within the bandwidth of interest. G_c denotes the boresight antenna gain, $\Gamma_{nm}(f)$ signifies the frequency-dependent load reflection coefficient,

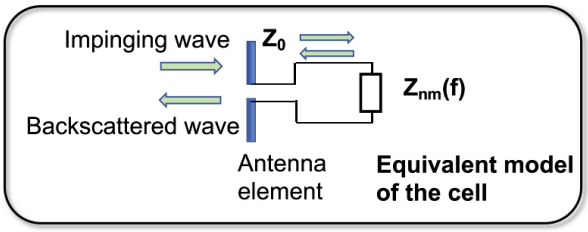

Figure 32: Equivalent model of the metaprism's cell.

$\beta_{nm}(\Theta_{\text{inc}}, \Theta; f)$ represents the reflection amplitude, and $\psi_{nm}(f)$ stands for the reflection phase. The load reflection coefficient is given by

$$\Gamma_{nm}(f) = \frac{Z_{nm}(f) - Z_0}{Z_{nm}(f) + Z_0}, \tag{61}$$

By properly designing the impedance $Z_{nm}(f)$ at each cell, it is possible to realize different reflecting behaviors, as will be explained later. Regardless of the specific technology adopted, we propose to design the reflection phase shift of the metaprism, $\Psi_{nm}(f)$, so that it exhibits a linear behavior with the frequency f, i.e.,

$$\Psi_{nm}(f) = \alpha_{nm} \cdot (f - f_c) + \gamma(f) \tag{62}$$

for f within the signal bandwidth B around the center frequency f_c, where α_{nm} is a cell-dependent coefficient and $\gamma(f)$ is a (possibly present) frequency-dependent phase shift. In particular, $\gamma(f)$ represents a common (among cells) phase offset which is irrelevant to beamsteering and focusing operations. For this reason, in the remaining text, we will neglect it. Thanks to the form in (62), it is possible to obtain a FSS with the desired reflection properties allowing for frequency-dependent beamsteering and focusing, behaving as a *metaprism*. Further details can be found in [19].

2.4.2 Low-complexity beamstearing using a metaprism

In the following, we show how the frequency selectivity of the metaprism can be exploited to obtain a subcarrier-dependent beamsteering in an Orthogonal Frequency Division Multiplexing (OFDM) communication system to cope with NLoS channel conditions. Specifically, we consider a downlink OFDM-based wireless system where a BS serves U single-antenna fixed users located in NLoS conditions with respect to it. In our study, we assume the BS is in LoS condition and in the far-field region with respect to concerning the metaprism. Moreover, we consider all the users are located in LoS condition with respect to the metaprism, but they could be in near- or far-field region depending on their distance from the surface. In a conventional OFDM system, the total bandwidth B is equally divided into $K \geq U$ orthogonal subcarriers with subcarrier spacing $\Delta f = \frac{B}{K}$. The frequency of the kth subcarrier is $f_k = f_c - \frac{B}{2} + k\Delta f$, $k = 1, 2, ..., K$, where f_c denotes the central frequency. The total transmitted power P_T is allocated differently among subcarriers (and hence users).

Through a proper design of coefficients α_{nm} in (62) characterizing the cells of the metaprism, it is possible to perform subcarrier-dependent beamsteering when both the transmitter and the receiver are in the LoS far-field region concerning the metaprism. In far-field condition, the complex channel gain between the transmitter and the nm-th cell of the metaprism for the k-th subcarrier can be well approximated as (plane wavefront) [26]:

$$h_{nm}^{(k)}(\mathbf{p}_{\text{BS}}) \approx \frac{h_0}{|\mathbf{p}_{\text{BS}}|} \exp\left(j\frac{2\pi}{\lambda}(n\,dx \cdot ux(\Theta_{\text{inc}}) + m\,dy \cdot uy(\Theta_{\text{inc}}))\right) \tag{63}$$

where $h_0 = \sqrt{\frac{G_T}{\lambda}}\frac{1}{4\pi}\exp\left(-j\frac{2\pi}{\lambda}|\mathbf{p}_{\text{BS}}|\right)$, G_T is the transmit antenna gain and Θ_{inc} is the direction of the impinging signal on the metaprism. For convenience, we have defined the quantities $ux(\Theta) = \sin(\theta)\cos(\phi)$ and $uy(\Theta) = \sin(\theta)\sin(\phi)$. The exponential argument accounts for the phase shift with respect to the metaprism's center

p_0. Similarly, the channel gain from the nm-th cell to the receiver located in position $\mathbf{p}$ can be approximated as:

$$g_{nm}^{(k)}(\mathbf{p}) \approx \frac{g_0}{|\mathbf{p}|} \exp\left(j\frac{2\pi}{\lambda}(n\,dx \cdot ux(\Theta) + m\,dy \cdot uy(\Theta))\right) \tag{64}$$

where $g_0 = \sqrt{\frac{G_R}{\lambda}}\frac{1}{4\pi}\exp\left(-j\frac{2\pi}{\lambda}|\mathbf{p}|\right)$ and G_R is the receive antenna gain. We consider the particular but significant case where $\beta_{nm}^{(k)}(\Theta_{\text{inc}}, \Theta) = \beta_0^{(k)}(\Theta_{\text{inc}}, \Theta), \forall n, m$, so that using the approximations above, the received signal at the kth subcarrier can be written as:

$$\begin{aligned} y^{(k)} =& \frac{\sqrt{P_T}\cdot h_0 \cdot g_0 \cdot \beta_0^{(k)}(\Theta_{\text{inc}}, \Theta)}{|\mathbf{p}_{\text{BS}}||\mathbf{p}|} \cdot \omega^{(k)} \cdot x^{(k)} \cdot \\ & \sum_{n=0}^{N-1}\sum_{m=0}^{M-1} \exp\left(j\frac{2\pi\, n\, dx}{\lambda}(ux(\Theta_{\text{inc}}) + ux(\Theta)) + j\frac{2\pi\, m\, dy}{\lambda}(uy(\Theta_{\text{inc}}) + uy(\Theta)) + j\Psi_{nm}^{(k)}\right) + n^{(k)}, \end{aligned} \tag{65}$$

where we denoted by $x^{(k)} \in \mathbb{C}$, with $\mathbb{E}\left\{|x^{(k)}|^2\right\} = 1$ a given user's information symbol transmitted at the generic OFDM frame, being $\mathbb{E}\{\cdot\}$ the statistical expectation operator; the transmitted symbols are multiplied by the weights $\omega^{(k)}$. The phase profile the metaprism should obey, at frequency f_k, to have the signal components related to the kth subcarrier reflected towards a target direction $\Theta_0^{(k)} = (\theta_0^{(k)}, \phi_0^{(k)})$, as:

$$\Psi_{nm}^{(k)} = -2\pi\frac{n\,dx}{\lambda}(ux(\Theta_{\text{inc}}) + ux(\Theta_0^{(k)})) - 2\pi\frac{m\,dy}{\lambda}(uy(\Theta_{\text{inc}}) + uy(\Theta_0^{(k)})) \tag{66}$$

so that all the phasors in (65) sum up coherently in the direction $\Theta_0^{(k)}$. Note that one could see the system transmitter-metaprism as an equivalent planar antenna array (reflectenna) whose frequency-dependent array factor is

$$AF^{(k)}(\Theta) = \sum_{n=0}^{N-1}\sum_{m=0}^{M-1} \exp\left(j\frac{2\pi\, n\, dx}{\lambda}(ux(\Theta) - ux(\Theta_0^{(k)}) + j\frac{2\pi\, m\, dy}{\lambda}(uy(\Theta) - uy(\Theta_0^{(k)})\right) \tag{67}$$

having $\beta_0^{(k)}(\Theta_{\text{inc}}, \Theta)$ as the pattern of each antenna element.

Now, with reference to (62), suppose we design the cell-dependent coefficients α_{nm}, $n = 0, 1, ..., N$, $m = 0, 1, ..., M-1$, such that they are related to the cell's positions $\mathbf{p}_{nm} = (x_n, y_m)$ as follows:

$$\alpha_{nm} = a_0 x_n + b_0 y_m$$

with a_0 and b_0 being two constants to be properly designed, as explained in Sec. 2.4.2. The frequency-dependent phase profile results

$$\Psi_{nm}(f) = \alpha_{nm} \cdot (f - f_0) = (a_0 x_n + b_0 y_m) \cdot (f - f_0). \tag{68}$$

By equating (68) and (66) it is

$$a_0(f_k - f_0) = -\frac{2\pi}{\lambda}(u_x(\Theta_{\text{inc}}) + u_x(\Theta_0^{(k)})) \quad \text{and} \quad b_0(f_k - f_0) = -\frac{2\pi}{\lambda}(u_y(\Theta_{\text{inc}}) + u_y(\Theta_0^{(k)})), \tag{69}$$

from which we can determine the reflection direction $\Theta_0^{(k)}$ as a function of the subcarrier k:

$$u_x\left(\Theta_0^{(k)}\right) = -u_x(\Theta_{\text{inc}}) - a_0\frac{\lambda}{2\pi}(f_k - f_0) \quad \text{and} \quad u_y\left(\Theta_0^{(k)}\right) = -u_y(\Theta_{\text{inc}}) - b_0\frac{\lambda}{2\pi}(f_k - f_0). \tag{70}$$

Equation (70) indicates that each subcarrier is reflected towards a different direction depending on the incident angle Θ_{inc}, the coefficients a_0 and b_0, and hence of cells' coefficients α_{nm}. In the next section, we provide a design example making use of (70).

Design example. Suppose that the signal transmitted by the BS impinges the metaprism with incident angle $\Theta_{\text{inc}} = (\theta_{\text{inc}}, 0)$ in the $x-z$ plane and that we want the metaprism to reflect the signal so that the signal component related to subcarrier $k = K$ (the highest subcarrier) is reflected with angle $\theta_0^{(K)} = -\theta_{\text{inc}} - \theta_m$, $\phi_0^{(k)} = 0$, for some angle θ_m, and the other subcarriers are reflected with different increasing angles in order to span a specific NLOS area. Note that according to (70) for the central subcarrier $k_0 = K/2$, corresponding to $f_{k_0} = f_c$, it is $\theta_0^{(k_0)} = -\theta_{\text{inc}}$, independently of a_0 and b_0.

From (69), by setting $k = K$, the design coefficients in (68) result in

$$a_0 = -\frac{2\pi}{\lambda(f_K - f_0)}\left(u_x(\Theta_{\text{inc}}) + u_x\left(\Theta_0^{(K)}\right)\right) = -\frac{4\pi}{\lambda B}\left(-\sin(\theta_{\text{inc}} + \theta_m) + \sin(\theta_{\text{inc}})\right)$$

$$b_0 = -\frac{2\pi}{\lambda(f_K - f_0)}\left(u_y(\Theta_{\text{inc}}) + u_y\left(\Theta_0^{(K)}\right)\right) = 0. \tag{23}$$

With this choice of a_0 and b_0, from (70) we obtain

$$\sin\left(\theta_0^{(k)}\right) = -\sin(\theta_{\text{inc}}) + \frac{2(f_k - f_0)}{B}\left(\sin(-\theta_{\text{inc}} - \theta_m) + \sin(\theta_{\text{inc}})\right). \tag{24}$$

The extreme case where $k = 1$ (the lowest subcarrier) gives

$$\sin\left(\theta_0^{(1)}\right) = -2\sin(\theta_{\text{inc}}) + \sin(\theta_{\text{inc}} + \theta_m).$$

As a result, each subcarrier is reflected according to a different angle in the range $\left[\theta_0^{(K)}, \theta_0^{(1)}\right]$, around Snell's angle $-\theta_{\text{inc}}$, thus creating the "prism" behavior.

In the following, some simulation results are presented concerning a typical industrial scenario to assess the potential of metaprism both to cope with NLoS situations and as a means to realize low-complexity beamforming at the BS. The system parameters are reported in Table 5.

Carrier frequency	$f_0 = 300$ GHz
Total bandwidth	$W = 10$ GHz
Number of subcarriers	$K = 256$
AP antenna gain	$G_T = 40$ dBi
RX noise figure	$F = 8$ dB
UE antenna gain	$G_R = 6$ dBi
TX Power	$P_T = 10$ dBm
Metaprism's size	100x100 cells (5x5 cm^2)

Table 5: System parameters.

Metaprism used to cover an NLoS condition. The first scenario considered is sketched in Fig. 33, where a BS in a typical industrial environment exploits a metaprism deployed along the wall at 5 meters distance to cover a 10×10 m^2 area in NLoS because of an obstacle. The metaprism was designed such that the signal impinging the metaprism from the BS is reflected with a span of $60°$. In particular, subcarrier $k = 1$ is reflected toward $\theta^{(1)} = -25°$ and the last subcarrier $k = K = 256$ is reflected toward the angle $\theta^{(1)} = -85°$. The intermediate subcarriers span the angles between these two extremes.

Supposing a user, e.g., a robot is navigating in the NLoS area, it can be kept connected to that BS by assigning to it the subcarrier corresponding to the angle under which it is seen by the metaprism. This does not necessarily imply that the robot's position must be known. In fact, the robot could periodically send pilot signals

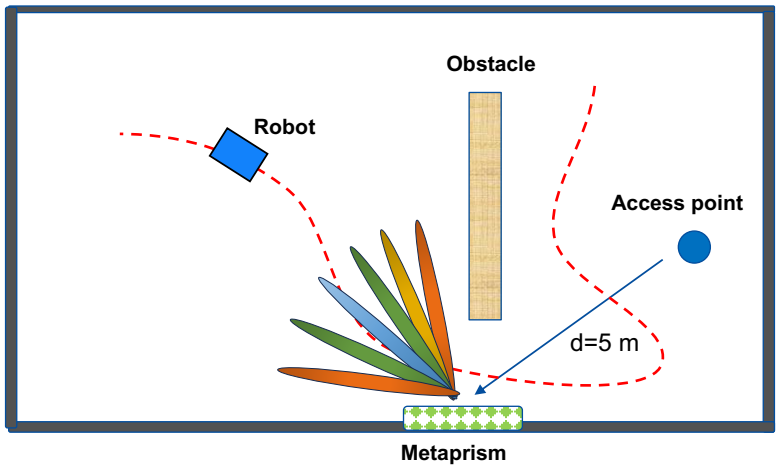

Figure 33: Metaprism used to cover a NLoS situation.

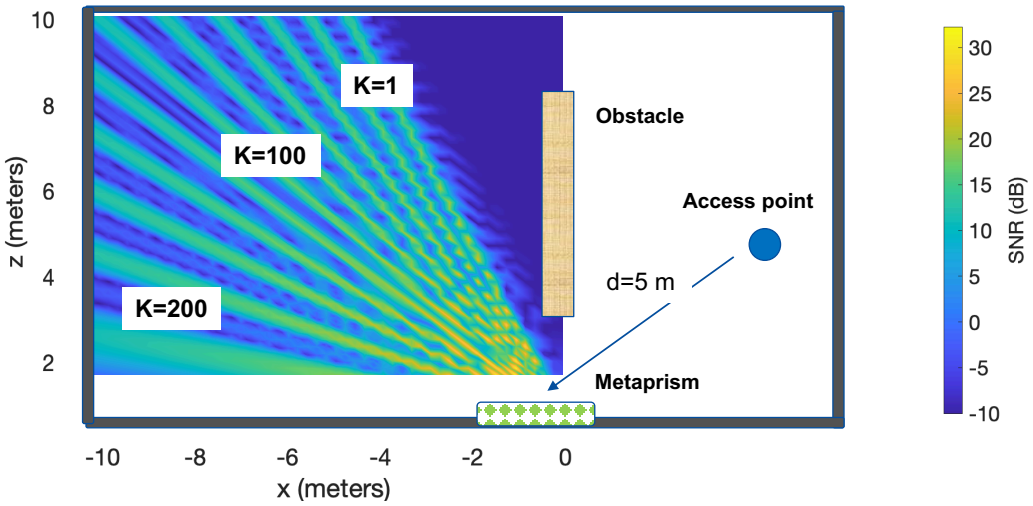

Figure 34: SNR heat map for the NLoS scenario.

that will be received by the BS only in the subcarriers corresponding to reflection angles close to that of its position.

In Fig. 34, the resulting SNR heat map is reported for a selected set of subcarriers (considering all the subcarriers, the area is continuously covered). As it can be noticed, the considered area is fully covered with a SNR larger than 10 dB despite the high path loss caused by the high frequency and the reflection thanks to the high frequency-selective gain of the metaprism. It is worth noticing that the coverage is similar to that one could obtain using a RIS but with the advantage of using a static device (no power supply, no signaling overhead, lower complexity).

Metaprism used as a frequency-selective transmitted antenna array in LOS condition The second scenario considered shows the use of the metaprism as a frequency-selective transmit antenna array with the purpose of allowing beamforming without the need to implement an antenna array at the BS, then with extremely low complexity. As shown in Fig. 35, a transmitting metaprism is placed in front of a single-antenna BS (1 m distance) in a LoS environment. The metaprism was designed to guarantee an angle span close to 160°. The subcarrier assignment strategy is the same as that described for the NLoS scenario.

The corresponding SNR heat map is displayed in Fig. 36 where the reflected beams are shown for a subset

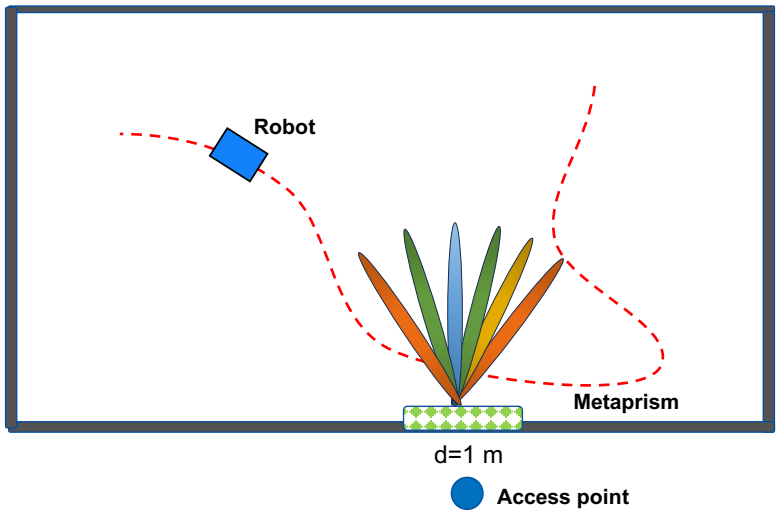

Figure 35: Metaprism used as a frequency-selective transmitted antenna array in LoS condition.

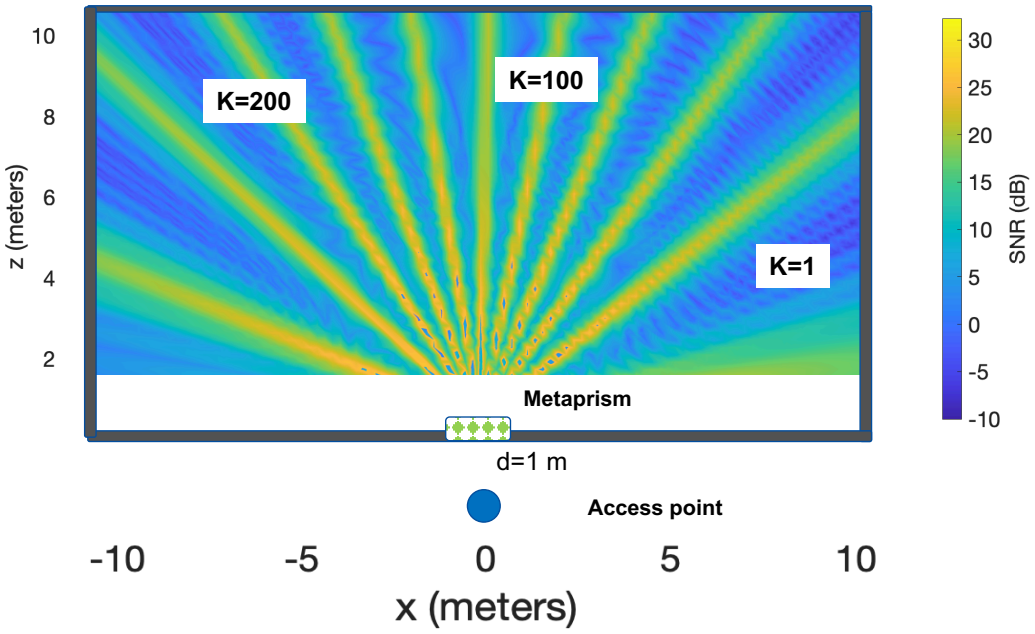

Figure 36: SNR heat map for the LoS scenario.

of subcarriers. Obviously, the presence of multiple users can be managed by assigning distinct subcarriers to the users according to their position.

The previous results demonstrate the feasibility of low-complexity beamforming exploiting a static device thus avoiding the implementation of large antenna arrays working in the THz band that could represent a cost/complexity barrier to the introduction of the THz technology in industrial scenarios.

2.5 Innovative schemes for enhancing sensing and localization with the use of intelligent surfaces at THz

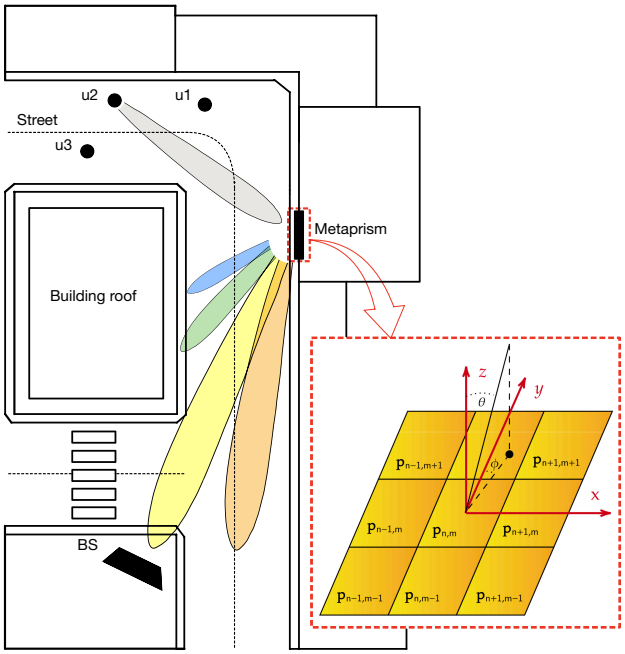

Figure 37: Typical scenario in which the signal transmitted by a user is reflected by the metaprism towards the base station. Each subcarrier component is reflected toward a different angle.

2.5.1 NLOS localization using Metaprisms

In this section, we investigate the possibility of exploiting metaprisms not only for communication purposes, as described before, but also to provide localization functionalities in NLoS conditions.

Referring to Fig. 37, we suppose a certain number of users are located in a region that is in NLoS concerning the BS located at coordinates $\mathbf{p}_{\text{BS}} = (d_{\text{BS}}, \Theta_{\text{BS}})$, where d_{BS} and Θ_{BS} are, respectively, the distance and the 3D angle of the BS with respect to the center $\mathbf{p}_0 = (0, 0, 0)$ of the metaprism, being $\Theta_{\text{BS}} = (\theta_{\text{BS}}, \phi_{\text{BS}})$, with θ_{BS} and ϕ_{BS} representing the azimuth and elevation angles.
We have not made any assumptions about the BS that can also be equipped with a single directive antenna. We assume that both the BS and the users are in LoS with reference to the metaprism. In the context of user localization, users transmit pilot symbols utilizing an OFDM modulation scheme across K available subcarriers, employing a multiple access protocol to prevent interference between them. We focus on the localization of a generic user. The user is located at position $\mathbf{p}_{\text{u}} = (d_{\text{u}}, \Theta_{\text{u}})$, where $\Theta_{\text{u}} = (\theta_{\text{u}}, \phi_{\text{u}})$. Denote by f_c the carrier frequency, λ the corresponding wavelength, and by f_k the k-th subcarrier frequency within the bandwidth B.
We suppose the metaprism lays in the $x-y$ plane as shown in Fig. 31 of Subsec. 2.4.1. Regarding the system

model, we exploit the one described in Sec. 2.4.2, whereby considering both BS-metaprism and metaprism-user Ricean channel models with Rice factor κ, the signal received by the BS at the k-th subcarrier can be expressed as

$$y_k = s_k(\mathbf{p}_\mathrm{u}) + v_k + n_k \tag{71}$$

for $k = 1, 2, \dots, K$, where $s_k(\mathbf{p}_\mathrm{u})$ is the specular component of the useful signal at the k-th subcarrier, dependent on the user's position $\mathbf{p}_\mathrm{u}$, whereas $n_k \sim \mathcal{CN}(0, \sigma^2)$ is the thermal noise sample, being $\sigma^2 = N_0 \Delta f$, N_0 the one-side noise power spectral density, and Δf the carrier spacing $\Delta f = B/K$. The term v_k represents the diffuse component of the received signal and is modeled as a complex Gaussian random variable, i.e., $v_k \sim \mathcal{CN}(0, \sigma_v^2)$. The useful specular component of the received signal $s_k(\mathbf{p}_\mathrm{u})$ is given by

$$s_k(\mathbf{p}_\mathrm{u}) = \sum_{n=0}^{N-1} \sum_{m=0}^{M-1} h_{mn}^{(k)}(\mathbf{p}_\mathrm{u})\, r_{mn}^{(k)}\, g_{mn}^{(k)}(\mathbf{p}_\mathrm{BS}) \sqrt{P_k \frac{\kappa}{1+\kappa}}\, x_k \tag{72}$$

where $r_{mn}^{(k)} = r_{mn}(f_k)$ depends on the metaprism design as described in Sec. 2.4.2, $P_k = P_\mathrm{T}/K$ is the transmitted power allocated to each subcarrier, P_T the total transmitted power, and x_k is the pilot symbol we set to one without loss of generality. The channel gains at frequency f_k between the user and the nm-th cell of the metaprism and between the nm-th cell and the BS are, respectively, given by

$$h_{mn}^{(k)}(\mathbf{p}_\mathrm{u}) = \frac{\sqrt{G_\mathrm{u}}\,\lambda}{4\pi|\mathbf{p}_\mathrm{u} - p_{mn}|} \exp\left(-j\frac{2\pi f_k}{c}|\mathbf{p}_\mathrm{u} - p_{mn}|\right) \tag{73}$$

$$g_{mn}^{(k)}(\mathbf{p}_\mathrm{BS}) = \frac{\sqrt{G_\mathrm{BS}}\,\lambda}{4\pi|\mathbf{p}_\mathrm{BS} - p_{mn}|} \exp\left(-j\frac{2\pi f_k}{c}|\mathbf{p}_\mathrm{BS} - p_{mn}|\right) \tag{74}$$

being c the speed of light, G_u and G_BS the antenna gains of the user and BS, respectively. According to the Ricean fading model, the power spectral density of the received signal's diffuse component is

$$\sigma_v^2 = |A_k|^2 P_k/(1+\kappa), \tag{75}$$

having defined

$$A_k = \sum_{n=0}^{N-1} \sum_{m=0}^{N-1} h_{mn}^{(k)}(\mathbf{p}_\mathrm{U})\, r_{mn}^{(k)}\, g_{mn}^{(k)}(\mathbf{p}_\mathrm{BS})\,. \tag{76}$$

Since the profile $\{y_k\}$, for $k = 1, 2, \dots, K$, of the received signal is a function of the user's position $\mathbf{p}_\mathrm{u}$, then it is possible to estimate $\mathbf{p}_\mathrm{u}$ from the observation of the y_k's. Here we exploit the Maximum Likelihood (ML) estimator, which can be expressed as

$$\widehat{\mathbf{p}}_\mathrm{u} = \arg\max_{\mathbf{p}_\mathrm{U}} \sum_{k=0}^{K-1} Re(y_k\, s_k^*(\mathbf{p}_\mathrm{u}))\,. \tag{77}$$

The ML in (77) corresponds to performing "fingerprinting" localization: the estimator compares the test profiles $\{s_k(\mathbf{p}_\mathrm{u})\}$, computed in all the test locations of the area of interest, with the profile of the received signal $\{y_k\}$, and chooses the position of the profile test pattern that most closely resembles that of the received signal. Obviously, the accuracy of the ML is strictly affected by the granularity of the test grid.

The numerical results reported in this section are related to simulation parameters given in Table 5 when not otherwise specified. The BS's position $\mathbf{p}_\mathrm{BS} = \{3.5, 0, 3.5\}$ m. The position of the users and scenario are shown in Fig.38. The metaprism has been designed to provide an angular span from $\theta_0^1 = -15°$ to $\theta_0^K = -85°$ with an incident angle of $\theta_\mathrm{inc} = 45°$. The test grid step is equal to 0.1 m. For each system configuration and metaprism design criterion, a 200-iteration Monte Carlo simulation has been performed.

The empirical cumulative distribution for the angular and position estimation are reported in Fig.39. What the results show is that by changing the transmitted power and the number of subcarriers the performance does not change because the array factor is already dense with $K = 256$ subcarriers and the SNR is already favorable with $P_\mathrm{T} = 10$ dBm. The results indicate less than $1°$ of angular error and 0.25 m of position error in 90% of the 200 Monte Carlo iterations thus showcasing the significant potential of the metaprism to aid the localization process in NLoS without significant complexity increase with respect to deploying additional BSs or using RISs [27, 28]. Further results can be found in [20, 21].

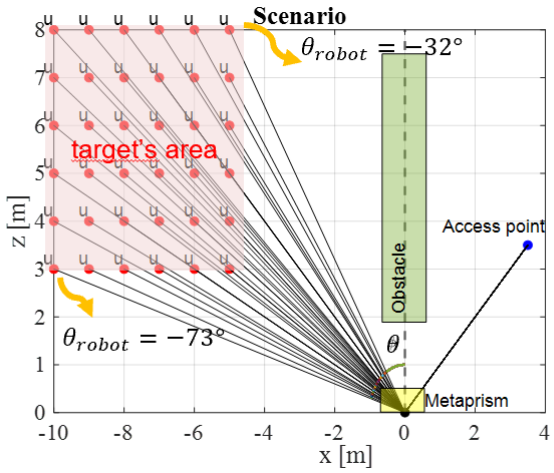

Figure 38: Simulation scenario of localization at 300 GHz

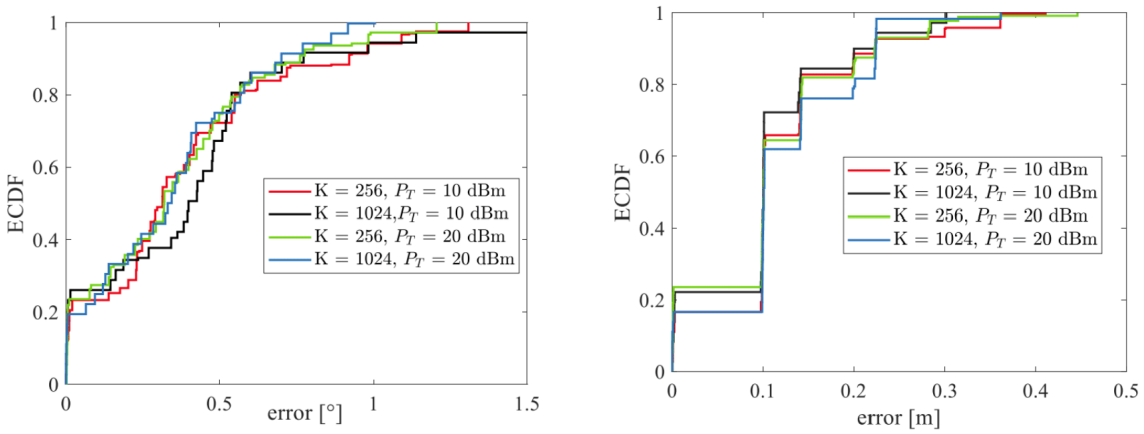

Figure 39: Angular and position Empirical cumulative distribution (ECDF)

2.5.2 RISs-aided Imaging

While the benefits of operating in the near-field regime have been extensively demonstrated for localization, communication, and sensing [29–35], the potential advantages of performing imaging within wireless communication networks operating at millimeter waves and THz frequencies have been largely unexplored to date [36]. This study explores the capabilities of near-field imaging [37–39], shedding light on its potential in practical sixth-generation (6G) applications, e.g., within an industrial scenario. Indeed, safety applications to wirelessly monitor human-to-machine interaction demand extremely low-latency communication and high imaging accuracy, especially in areas where conventional technologies like cameras or thermal sensors may encounter challenges due to obstructed visibility or interference. Given these challenges, our proposed approach leverages a RIS to extend the reach of imaging capabilities, thus proving instrumental in covering blind corners beyond the direct visibility of the transmitter. This ensures unparalleled spatial awareness for critical safety applications and becomes paramount in contexts where alternative technologies may falter, positioning our proposed imaging system as a valuable complement to existing surveillance methods. The process involves initially illuminating the ROI, represented as a pixel-based image, and subsequently capturing its backscattered EM field through the receiving array. The near-field propagation regime, characterized by a larger number of Degrees of Freedom (DOF) compared to the far field, facilitates the collection of more informative measurements from the ROI, thereby enhancing imaging capabilities. Although numerous technologies have been explored to minimize reconstruction errors and enhance the resolution of target images, e.g., Synthetic Aperture Radar (SAR) [40],

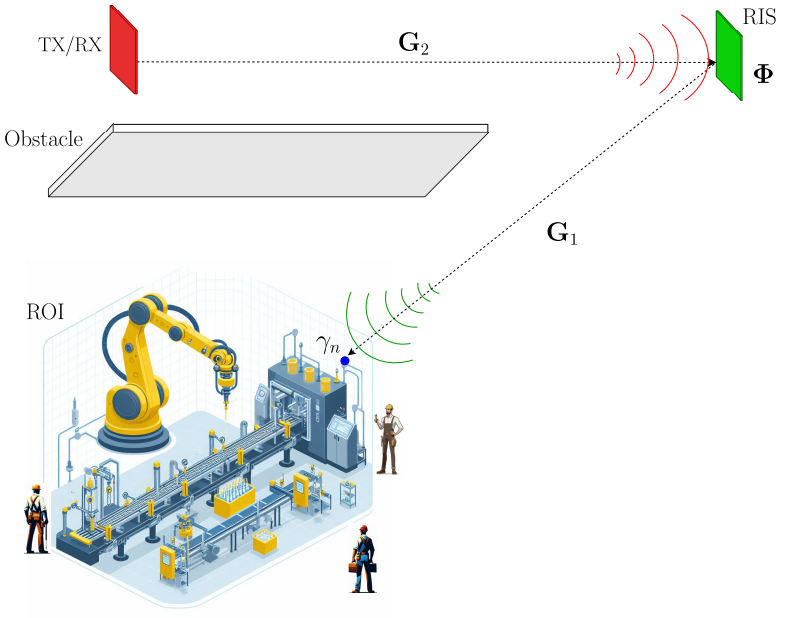

Figure 40: Monostatic RIS-aided system for NLoS imaging of an arbitrary ROI within a factory.

MIMO antennas [41], and computational imaging [42], only a few works have investigated the use of systems primarily designed for wireless communications to perform imaging of unknown objects [43]. Moreover, the imaging approaches proposed in the literature typically operate in the far-field regime and account for deploying a dedicated imaging infrastructure, which needs to illuminate and collect the backscattered EM field from a large set of angles. Consequently, their applicability in next-generation wireless systems endowed with Integrated Sensing and Communication (ISAC) capabilities is limited.

Consider the imaging scenario in Fig. 40, which illustrates a RIS-aided monostatic configuration in NLoS conditions. Specifically, with NLoS we here refer to the case where the direct path between the transceiver and the ROI to be imaged is obstructed, whereas there exists a LoS condition between the RIS and both the ROI and the transceiver. In this manner, we consider that the overall transceiver-ROI link is a concatenation of two LoS channels connected through the RIS. The monostatic transceiver comprises $N_\mathsf{T} = N_\mathsf{R}$ antenna elements and illuminates the ROI with a signal of wavelength λ. The RIS can be modeled as an array of $L = S \times Q$ elements (unit cells) and each RIS cell is characterized by a specific reflection coefficient $\nu_{i,j}$, $i = 1, \dots, S$, $j = 1, \dots, Q$, such that, by stacking all the L coefficients into the vector $\boldsymbol{\nu}$, we can define the matrix $\mathbf{\Phi} = \mathrm{diag}(\boldsymbol{\nu}) \in \mathbb{C}^{L \times L}$ to describe the reflection properties of the RIS. All the arrays' positions are considered known. The ROI is divided into a grid of N square cells of size Δ, located in $\mathbf{p}_n = [x_n, y_n, z_n]^T$, $n \in \mathcal{N} = \{1, 2, \dots, N\}$. Each cell, characterized by a scattering coefficient γ_n, relates to the Radar Cross Section (RCS) of the scatterer within it. If the cell is empty, it holds $\gamma_n = 0$. We assume that $|\gamma_n| \leq \gamma_{\max} = \sqrt{\frac{4\pi}{\lambda^2}\mathrm{RCS}_{\max}}$, $\forall n \in \mathcal{N}$, where $\mathrm{RCS}_{\max} = \frac{4\pi}{\lambda^2}\Delta^2$ is the RCS of a Perfect Electric Conductor (PEC) with area Δ^2. We define $\boldsymbol{\gamma} = [\gamma_1, \gamma_2, \dots, \gamma_N]^T \in \mathbb{C}^{N \times 1}$ as the unknown vector of scattering coefficients associated with the selected ROI that needs to be estimated [44].[4] Moreover, in the absence of a statistical model for the ROI image, we assume that $\boldsymbol{\gamma}$ constitutes a deterministic unknown vector.

The transceiver emits an illumination signal $\mathbf{x} \in \mathbb{C}^{N_\mathsf{T} \times 1}$, $||\mathbf{x}||^2 \leq P_\mathsf{T}$, with P_T the available transmit power. Assuming that the direct transceiver-ROI link is obstructed, the received signal at the transceiver is $\mathbf{y} \in \mathbb{C}^{N_\mathsf{R} \times 1}$

[4]We assume perfect isotropic reflection of the illumination signal in each ROI cell, thus neglecting any diffusive or multiple scattering effects due to the adoption of high frequencies. Moreover, we assume no coupling occurs between the transceiving antennas and the scatterers.

and it is given by

$$\mathbf{y} = \mathbf{G}_{\mathrm{R}}\,\boldsymbol{\Gamma}\,\mathbf{G}_{\mathrm{T}}\,\mathbf{x} + \mathbf{w}\,, \tag{78}$$

where $\mathbf{G}_{\mathrm{T}} = \mathbf{G}_2\boldsymbol{\Phi}\mathbf{G}_1$ and $\mathbf{G}_{\mathrm{R}} = \mathbf{G}_1\boldsymbol{\Phi}\mathbf{G}_2$ denote respectively the illuminating and sensing channels, with $\mathbf{G}_1$ and $\mathbf{G}_2$ being the RIS-ROI and transceiver-RIS channel matrices, $\mathbf{w} \in \mathbb{C}^{N_{\mathrm{R}}\times 1} \sim \mathcal{CN}(0, \sigma^2\mathbf{I}_{N_{\mathrm{R}}})$ is the Additive White Gaussian Noise (AWGN) vector, $\mathbf{I}_{N_{\mathrm{R}}}$ is the identity matrix of dimension N_{R}, and $\boldsymbol{\Gamma} = \mathrm{diag}(\boldsymbol{\gamma}) = \mathrm{diag}(\gamma_1, \gamma_2, \dots, \gamma_N) \in \mathbb{C}^{N\times N}$ is a diagonal matrix containing the ROI's scattering coefficients.[5] The received signal can be re-written as

$$\mathbf{y} = \mathbf{G}_{\mathrm{R}}\,\boldsymbol{\Gamma}\,\tilde{\mathbf{x}} + \mathbf{w} = \mathbf{G}_{\mathrm{R}}\,\tilde{\mathbf{X}}\,\boldsymbol{\gamma} + \mathbf{w}\,, \tag{79}$$

where $\tilde{\mathbf{X}} = \mathrm{diag}(\tilde{\mathbf{x}}) \in \mathbb{C}^{N\times N}$, and $\tilde{\mathbf{x}} = \mathbf{G}_{\mathrm{T}}\,\mathbf{x} \in \mathbb{C}^{N\times 1}$ being the vector identifying the illumination signal as observed at the ROI side. To perform holographic imaging, the ranks of $\mathbf{G}_{\mathrm{T}}$ and $\mathbf{G}_{\mathrm{R}}$ must be much greater than one. Therefore, we assume the ROI is in the radiative near-field region of the transceiver, and/or the RIS, i.e., the distance d between the array/RIS and the ROI satisfies $0.62\sqrt{\frac{D^3}{\lambda}} \leq d \leq \frac{2D^2}{\lambda}$, with D the size of the largest ROI/array [45].

The main goal of the imaging process involves two key tasks: (*i*) accurately estimating $\boldsymbol{\gamma}$ from the signal received in (78); (*ii*) identifying the most effective illumination signal $\mathbf{x}$ and the optimal RIS configuration for minimizing the estimation error. Due to the ill-posed nature of the Inverse Scattering Problem (ISP) under analysis, characterized by being ill-defined and ill-conditioned [46], it is essential to apply regularization techniques to counteract substantial noise enhancements arising from the $\mathbf{G}_{\mathrm{R}}$ matrix pseudoinverse computation. For this reason, we apply Truncated Singular Value Decomposition (TSVD), by keeping only the R strongest. Then, Least Squares (LS) estimate of $\boldsymbol{\gamma}$ can be computed as [37]

$$\hat{\boldsymbol{\gamma}} = \boldsymbol{\gamma} + \tilde{\mathbf{X}}^{-1}\,(\mathbf{H} - \mathbf{I})\,\tilde{\mathbf{X}}\,\boldsymbol{\gamma} + \tilde{\mathbf{X}}^{-1}\mathbf{z}\,. \tag{80}$$

This equation reveals three well-defined terms contributing to the LS estimate $\hat{\boldsymbol{\gamma}}$, i.e., the true value of $\boldsymbol{\gamma}$, a distortion term from regularization, and a noise contribution, respectively. To evaluate the accuracy of the imaging procedure in estimating $\boldsymbol{\gamma}$, we derive a closed-form expression for the Mean Square Error (MSE) of the LS estimate of the deterministic unknown $\boldsymbol{\gamma}$ as a function of $\tilde{\mathbf{x}}$ [37]. Notably, $\mathrm{MSE}(\boldsymbol{\gamma}; \tilde{\mathbf{x}})$ depends on two discernible contributions: a first term representing the distortion introduced by the regularization technique in the estimation procedure, and a second term that is linked to the AWGN presence. A crucial aspect of conducting imaging involves the identification of the optimal illumination signal $\mathbf{x}^\star$, which aims to minimize $\mathrm{MSE}(\boldsymbol{\gamma}; \tilde{\mathbf{x}})$. To facilitate our analysis, we decompose the problem into two sequential steps. Initially, we estimate the illumination signal $\tilde{\mathbf{x}}^\star$, denoted as the signal received at the ROI after propagating through the TX-ROI channel $\mathbf{G}_{\mathrm{T}}$. Subsequently, we determine the corresponding transmit signal $\mathbf{x}^\star$ necessary to achieve a received illumination signal closely approximating $\tilde{\mathbf{x}}^\star$. Given that the MSE is dependent on the actual value of $\boldsymbol{\gamma}$, we frame our problem as follows

$$\begin{aligned} \tilde{\mathbf{x}}^\star = \arg\min_{\mathbf{x}} \max_{\boldsymbol{\gamma}}\ & \mathrm{MSE}(\boldsymbol{\gamma}; \tilde{\mathbf{x}}) \\ \text{s.t. } & ||\mathbf{x}||^2 \leq P_{\mathrm{T}} \\ & |\gamma_n| \leq \gamma_{\max},\ n = 1, 2, \cdots, N\,, \end{aligned} \tag{81}$$

where we recall that $\tilde{\mathbf{x}} = \mathbf{G}_{\mathrm{T}}\,\mathbf{x}$ and $\gamma_{\max}$ represents the maximum magnitude of the scattering coefficient. Specifically, in the presence of a scatterer in the nth ROI cell, the parameter γ_n is assigned the value $M = 10^{-1}\gamma_{\max}$, as real objects typically demonstrate a RCS smaller than that of a PEC. To solve the problem, we optimized the transmitting vector using an interior-point method [47]. This algorithm is initialized using an initial guess solution set equal to $\tilde{\mathbf{x}}_0 = \frac{\sqrt{P_{\mathrm{T}}}}{2N_{\mathrm{T}}}\,\mathbf{G}_{\mathrm{T}}\,(\mathbf{1}_{N_{\mathrm{T}}\times 1} + j\mathbf{1}_{N_{\mathrm{T}}\times 1})$, which corresponds to a uniform illumination of the RIS. Moreover, as previously discussed, we set $\gamma_n = \gamma_{\max}$, $\forall n = 1, \dots, N$, to provide an upper-bound of the cost function to be minimized, being the MSE dependent of the true value of $\boldsymbol{\gamma}$, which is unknown. Once the optimal $\tilde{\mathbf{x}}^\star$ was found, the illumination vector was computed using $\mathbf{x}^\star = \tilde{\mathbf{G}}_{\mathrm{T}}^{\dagger}\tilde{\mathbf{x}}^\star$, where $\tilde{\mathbf{G}}_{\mathrm{T}}$ represents the regularized

[5] Notably, (78) neglects the direct transceiver-ROI contribution because, due to obstructions, it does not lead to any insightful information for imaging the ROI.

version of $\mathbf{G}_\mathrm{T}$. For further insights into optimizing the illumination waveforms at the transmitter side, readers can refer to [37] for a detailed investigation of design considerations.

Apart from that, one should note that the overall optimization of the imaging system not only requires optimizing the transmit signal $\mathbf{x}$ used to illuminate the RIS but also optimizing the RIS configuration itself. Indeed, while in traditional NLoS imaging scenarios, passive walls have primarily been used to aid the ROI illumination [48], the introduction of a RIS opens the door to smarter reflections.

It can be demonstrated that the optimal RIS configuration is given by

$$\mathbf{\Phi}^\star = \mathbf{V}_1 \mathbf{U}_2^H \,. \tag{82}$$

This corresponds to matching the RIS phase profile to the right and left singular vectors of the TX-RIS and RIS-ROI channels, respectively. Incidentally, this is the same result achieved in [13] through an alternative method for maximizing the mutual information between a TX and a RX communicating via a RIS.

For our numerical analysis, we perform imaging over a frequency band $\Delta f = 40\,\mathrm{MHz}$ centered at $f_\mathrm{c} = 300\,\mathrm{GHz}$, with a wavelength of $\lambda = 1\,\mathrm{mm}$. This decision can entail selecting either a sub-carrier or a resource block within an OFDM signal, which is also employed for communication purposes. Then, we consider a transceiver equipped with a uniform squared array with size $(80\lambda \times 80\lambda)\,\mathrm{m}^2$, with antenna elements spaced apart of λ. The selected ROI spans an area of $(480\lambda \times 480\lambda)\ \mathrm{m}^2$, with 8×8 cells equally distributed with an inter-spacing of $\Delta = 60\lambda$. Moreover, the RIS has dimensions equal to $(80\lambda \times 80\lambda)\,\mathrm{m}^2$, corresponding to $L = 6400$, and in paraxial configuration with respect to the transceiver. Specifically, the transceiver is placed in $(0, 0, 0)\ \mathrm{m}$, the RIS is located in $(0,\ 1100\lambda,\ 0)\ \mathrm{m}$, while the ROI's center is positioned in $(0,\ 0,\ -300\lambda)\ \mathrm{m}$. The noise power spectral density is equal to $\sigma^2 = -200\ \mathrm{dBm/Hz}$, and the transmitted power P_T is equal to $0\ \mathrm{dBm}$. Performance assessment is performed using both the empirical and theoretical MSE, along with its normalized version, referred to as Normalized Mean Square Error (NMSE). Specifically, these metrics were calculated as

$$\text{E-MSE} = \frac{\sum_{m=1}^{N_\mathrm{MC}} \|\boldsymbol{\gamma} - \hat{\boldsymbol{\gamma}}_m\|^2}{N_\mathrm{MC}}, \quad \text{E-NMSE} = \frac{\text{E-MSE}}{NM^2}\,, \tag{83}$$

where N_MC denotes the number of Monte Carlo iterations, set at 100. Similarly, the Theoretical Mean Squared Error (T-MSE) is expressed by the analytical $\mathrm{MSE}(\boldsymbol{\gamma}; \tilde{\mathbf{x}})$ expression derived in [37], and its normalized counterpart is denoted as T-NMSE. Our results showcase three distinct approaches:

- *No regularization (NO REG-NO OPT)*: This represents the most unfavorable configuration, wherein we did not take into account both the regularization of the $\mathbf{G}_\mathrm{R}$ matrix and the optimization of the transmit illuminating vector. We have included this scenario in our simulations as a benchmark.
- *Regularization, No optimization (NO OPT)*: In this case, we regularize by applying the TSVD with a fixed threshold to preserve only the first R eigenvalues of $\mathbf{G}_\mathrm{R}$. Conversely, for the $\mathbf{G}_\mathrm{T}$ matrix, we employ TSVD by retaining all eigenvalues whose cumulative sum does not exceed 99% of the total transmit power P_T, given that the illuminating channel is not susceptible to any noise enhancement. Here, we did not implement the optimization of the transmitted signal and we set it as $\mathbf{x} = \frac{\sqrt{P_\mathrm{T}}}{2N_\mathrm{T}}\left(\mathbf{1}_{N_\mathrm{T}\times 1} + j\mathbf{1}_{N_\mathrm{T}\times 1}\right)$.
- *Regularization & Interior-Point Optimization (OPT)*: We applied both the $\mathbf{G}_\mathrm{T}$ and $\mathbf{G}_\mathrm{R}$ matrices regularization as per the previous case but we also added the interior-point method optimization of the transmitting vector.

Moreover, three distinct RIS configurations were tested: (*i*) *matched*, which corresponds to the optimal configuration as per (82), (*ii*) *PEC*, i.e., the RIS acts like a perfect reflecting mirror with $\mathbf{\Phi} = \mathbf{I}$, (*iii*) *anomalous reflection*, which implements the phase profile specifically designed to point the reflected signal toward the ROI's center, when illuminating the radio environment, and toward the transceiver's center when sensing the backscattered EM signal. This latter approach is typically adopted when operating in the far-field regime. Unfortunately, despite careful testing, the PEC case is not depicted in the following figures. This is because it exhibited the configuration with inferior results and extremely high values of NMSE. In this instance, it becomes impractical to reconstruct any image at the transceiver side, rendering the presence of the RIS virtually ineffective for the

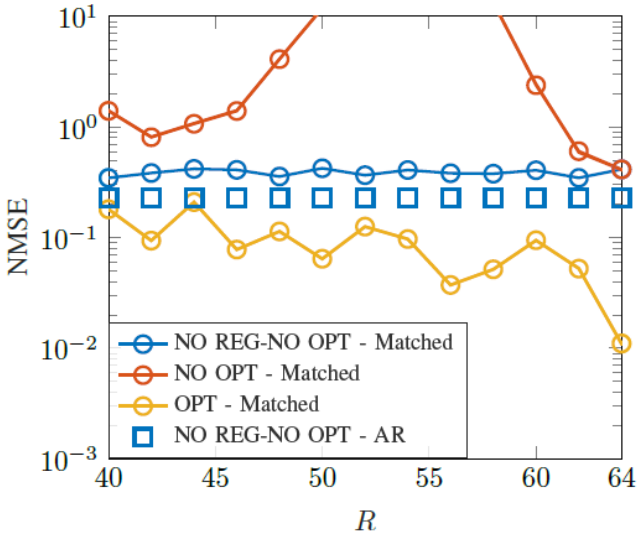

Figure 41: NMSE as a function of the truncation index R selected when applying the TSVD to $\mathbf{G}_R$ and in the presence or absence of the illumination optimization. Dotted ($\circ$) and continuous ($-$) lines correspond to the E-NMSE and T-NMSE, respectively.

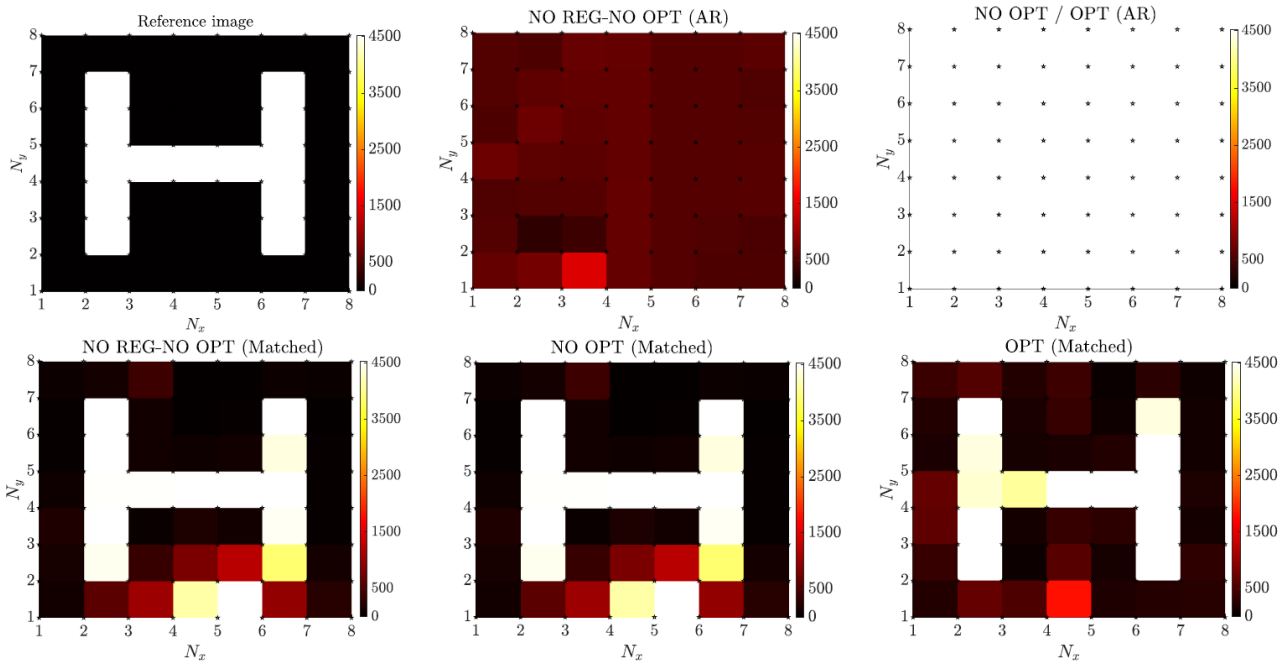

Figure 42: Estimated images ($\hat{\gamma}$) retrieved from the industrial ROI under investigation for $R = 64$. The top-left figure illustrates the reference image to be reconstructed, while top-(center,right) figures represent the image reconstructions for the AR case. The second row shows the reconstructed images when the RIS is optimally configured as per (82).

imaging procedure if not specifically optimized. In Fig. 41, the curves depicting the E-NMSE and T-NMSE are presented for different values of the selected truncation index for TSVD $R \leq N$. In this setup, it is $N = 64$. The matched case demonstrates superior performance in comparison to the other two RIS configurations, thereby facilitating the achievement of NMSE values that are several orders of magnitude smaller. This analysis underscores the fundamental significance of configuring the phase shift matrix $\mathbf{\Phi}$, which governs the behavior of the

signal reflected by the RIS, to be precisely adapted to the wireless channels connecting the transceiver to the ROI. Notably, the curves corresponding to the NO OPT and OPT cases for the AR RIS configuration achieved higher values that extended beyond the plot range. This indicates that image reconstruction is not feasible unless the peculiarities of the near-field MIMO channel are considered and the large number of DOF available are properly leveraged to reconstruct the single-shot image of the ROI with maximum fidelity. Given that the far-field condition, where the number of DOF converges to unity, represents the most challenging scenario for imaging, configuring the RIS with a reflective profile commonly employed in the far field does not permit to fully exploit the channel's DOF available in the Fresnel region, hence improve the reconstruction accuracy of the imaging system. Fig. 42 displays the estimated images, i.e., the $\hat{\gamma}$ values, for the matched and the AR configurations in the presence or absence of both regularization and transmit vector optimization for $R = 64$. Specifically, the first row illustrates the image reconstructed at the transceiver side when the RIS is configured to point only toward the ROI and the transceiver's centers (AR case). In this case, neither regularization nor optimization affects the performance, as the transceiver cannot reconstruct even a single pixel. Conversely, the second row illustrates the three cases corresponding to NO REG-NO OPT, NO OPT, and OPT. These are obtained when the RIS is optimally configured and matched to the strong near-field propagation regime occurring at THz frequencies. In this scenario, it is evident that only the ad-hoc configuration of the RIS allows for a decent reconstruction of the reference image (NO REG-NO OPT and NO OPT case), thereby emphasizing its pivotal role. Furthermore, it is observed that the accuracy and resolution of the reconstructed image can be significantly enhanced when optimizing the transmitted waveform from the transceiver to appropriately illuminate the RIS. This optimization results in a much sharper and well-defined image, thus representing a crucial performance improvement for mission-critical applications focused on workplace safety. Indeed in such contexts, even a small number of pixels reconstructed inaccurately can pose a serious risk to workers and those in proximity.

2.6 Link and system-level simulations of smart propagation environments in THz-based networks

In this section, we describe the implementation of a simulation tool for link- and system-level evaluation of RISs-assisted THz wireless networks. In our previous deliverable [49], we selected SiMoNe as a suitable simulation tool for evaluating the solutions developed within the TIMES project. In the following, we provide a general overview of SiMoNe and describe how this tool has been extended to support the modeling of RISs.

2.6.1 Overview of the SiMoNe simulator

SiMoNe represents a comprehensive platform tailored for the realistic modeling and analysis of mobile wireless communication systems. Developed initially in 2014 to facilitate system-level simulations of mobile networks, SiMoNe has since evolved into a sophisticated simulation suite capable of accurately modeling propagation and system-level behavior in wireless communication systems.
At its core, SiMoNe embodies a modular and flexible approach to simulation, employing a block concept known as "pipes and filter" [50]. This design pattern, inspired by data processing principles, compartmentalizes various functionalities into distinct blocks, each responsible for handling specific tasks within the simulation pipeline. These blocks operate sequentially, passing data between them as inputs and outputs, thus forming an efficient data processing pipeline. This modular composition not only enhances adaptability but also facilitates seamless integration of new concepts, hardware, and simulation technologies as the field of mobile wireless communication continues to evolve.
The SiMoNe simulation suite comprises three interconnected parts, each serving a unique role in the simulation framework. First and foremost, SiMoNe incorporates a powerful ray tracer system, enabling the accurate modeling of 3D scenarios and the prediction of communication paths with consideration for delay and amplitude. Leveraging ray-optical methods, this component provides invaluable insights into the behavior of wireless channels, particularly in the context of THz communication systems where quasi-optical propagation plays a crucial role. SiMoNe accounts for the four types of interactions of rays and surfaces: reflection, diffraction, transmission, and scattering, ensuring a comprehensive understanding of signal propagation characteristics [51].
Building upon the foundation laid by the ray tracer, SiMoNe features a sophisticated system-level simulation module. This component allows for the comprehensive analysis of mobile wireless networks, taking into account factors such as network topology, node placement, and traffic patterns. By simulating realistic scenarios, researchers can evaluate the performance of various communication protocols and algorithms, paving the way for the development of robust and efficient mobile network architectures [52].
The third and final part of SiMoNe is the link level simulator, a high-fidelity tool designed to model the intricate details of individual communication links. Operating at the physical layer, this simulator focuses on the signal processing aspects of wireless communication, meticulously tracking the transmission of data bits between transmitters and receivers. Through the use of advanced coding schemes, modulation techniques, and channel models, the link level simulator provides invaluable insights into the performance of communication links, enabling researchers to optimize system parameters for optimal reliability, latency, and throughput. Additionally, SiMoNe's link level simulator facilitates the simulation of RF impairments, allowing for a comprehensive assessment of system performance in real-world scenarios [50].
Following the introductory overview of SiMoNe, the subsequent sections provide concise descriptions of how RISs are integrated into each component of the framework. Throughout these sections, we showcase the potential research avenues enabled by SiMoNe for investigating the application of RISs in wireless communication systems.

2.6.2 Ray tracing simulations considering the impact of RIS

SiMoNe's ray tracing module, integrated within the FemtoPred channel predictor, serves as a powerful tool for accurately modeling wireless communication channels. Operating within a two-step approach, this module predicts propagation channels by first searching for geometric paths between Transmitter (TX) and Receiver (RX),

then applying electromagnetic models to determine complex amplitudes of Multipath Components (MPCs) [51].

In the initial step, the ray tracing engine conducts a meticulous search for viable geometric paths between the TX and RX. This process involves identifying potential paths characterized by Angle of Departures (AoDs) and Angle of Arrivals (AoAs), as well as interaction points at surfaces. A critical aspect of this step is the determination of valid paths, which involves assessing the feasibility of transmission through surfaces [53].

Direct paths, reflecting the most straightforward transmission route, are calculated based on the relative positions of the TX and RX. The path loss associated with direct paths is computed considering the free-space path loss model, accounting for the distance between the TX and RX. Additionally, if applicable, the transmission loss through surfaces is calculated using the transfer matrix method, considering the material properties and thickness of intervening surfaces.

Reflected paths are identified using the principle of image sources, wherein the TX is mirrored at each surface to pinpoint potential reflection points. The reflection coefficients at each interaction point are derived using the transfer matrix method, which considers the properties of the surface material and the incident angle of the ray.

Scattered rays are identified by dividing surfaces with line-of-sight connections into tiles and validating paths through each tile. If a line-of-sight connection persists for an individual scatter tile, the ray passing through the tile is deemed valid. The complex amplitude of scattered rays is determined using the modified equivalent current approximation, which considers the scattering properties of the surface material as a function of the wavelength.

In the subsequent step, electromagnetic models are applied to predict the complex amplitudes of MPCs along the identified paths. This involves accounting for various propagation mechanisms, including reflection, scattering, and diffraction. Scattered rays contribute to the overall received signal by interacting with objects in the environment, leading to variations in signal strength and phase. Due to complexity, only the last reflection point of a MPC is considered for scattering.

SiMoNe's ray tracing capabilities extend beyond path prediction to include the generation of antenna diagrams, providing insights into the directional characteristics of antennas. By incorporating antenna patterns, researchers can analyze the spatial distribution of transmitted and received power, aiding in the design and optimization of antenna configurations for specific communication scenarios.

The verification process of SiMoNe's ray tracer for indoor scenarios involves comparing simulated MPC with measurement results to assess simulation accuracy, shown in [54]. This comparison focuses on power angular profiles (PAPs) and power delay profiles (PDPs) to evaluate spatial and temporal agreement between simulations and measurements. In cases where the simulated and measured MPCs align closely, particularly in regions of measured MPCs, the agreement indicates the ray tracer's effectiveness in capturing the propagation characteristics accurately. However, discrepancies in gain for those influenced by scattering highlight challenges in accurately representing material properties and interaction points. [54]

Integrating RIS into the ray tracer of SiMoNe necessitates several modifications to accurately model their effects on wireless propagation. First and foremost, RIS needs to be implemented as additional transmitting and receiving elements within the ray tracing environment, allowing for the tracing of rays between transmitters, RIS, and receivers. This entails incorporating RIS antenna diagrams to capture their electromagnetic characteristics. These diagrams are derived from measurements and simulations. Depending on the AoA, an appropriate antenna diagram must be chosen and applied to the MPCs departing from the RIS. Additionally, the ray object description needs to be expanded to include parameters specific to RIS interactions, such as interaction points, path length, angles of arrival and departure, and attenuation. Furthermore, adjustments to ray tracer settings related to reflection, transmission, diffraction, and scattering are essential to accommodate the unique behavior of RIS (e.g., the number of interaction points and when scattering and diffraction need to be taken into account). Finally, the integration process requires thorough validation through simulation and comparison with empirical data to ensure the accuracy and reliability of the modeled RIS effects [55].

The initial ray tracing results provide valuable insights into the impact of integrating RIS into the communication

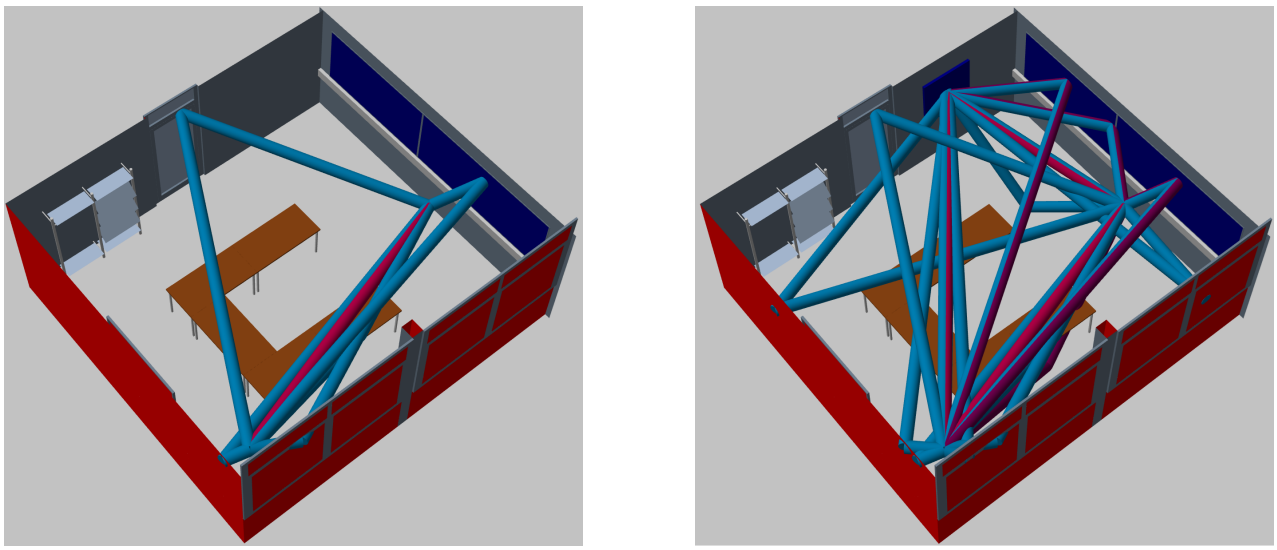

(a) Ray Tracing without RIS

(b) Ray Tracing with RIS

Figure 43: Ray Tracing with and without RIS in a conference room

scenario. In Fig. 43(a), depicting the ray tracing without RIS, the meeting room scenario exhibits several reflected paths alongside a direct path between the TX and RX, resulting in a total of six distinct paths. This configuration represents the baseline scenario, demonstrating the propagation characteristics in the absence of RIS. Contrastingly, Fig. 43(b) illustrates the ray tracing results with the inclusion of RIS positioned on the wall of the meeting room. The integration of RIS introduces additional complexity to the communication environment, manifesting in a significantly expanded set of communication paths. With RIS acting as intermediate elements between the TX and RX, the number of paths increases substantially to a total of 42, reflecting the combinatorial expansion of ray tracing paths facilitated by the presence of RIS. These results underscore the transformative potential of RIS in shaping the propagation environment and highlight the importance of accurate modeling and analysis in understanding their impact on wireless communication systems.

2.6.3 Investigating the effect of RIS in System Level Simulations

The system level simulator (SLS) in SiMoNe is designed to comprehensively model and analyze various aspects of mobile cellular networks. From its inception, the SLS was conceived with the principle of utilizing real geographical data and realistic network topologies to ensure the fidelity of simulations. The SLS is a manifestation of this principle, providing a versatile platform capable of simulating diverse scenarios with precision and accuracy. By leveraging real-world data and advanced modeling techniques, the SLS enables researchers and engineers to evaluate the performance of mobile networks under different conditions, ranging from typical 3GPP scenarios to custom-designed network layouts [52].

The simulation scenarios in SiMoNe primarily depend on and represent real geographical data. This is evident in several aspects: firstly, in the non-regular network topology, which incorporates pathloss predictions that inherently reflect the geographical data. Secondly, the dynamic user demand is based on tempo-spatial traffic distributions, which include either discrete intensities or individual user traces. The ray tracer described in the previous section is used to model the propagation [52].

The SLS in SiMoNe supports two distinct representations of user demand. The first is an abstracted, macroscopic representation given by traffic intensity maps, which illustrate the spatial and temporal variations in network-wide or cell-specific traffic intensity over different times of the day. The second is a microscopic representation, involving individual user traces that simulate the behavior of users within the network, each associated with specific demand types.

The traffic intensity maps method models the variations in traffic intensity across different times of the day, providing an average traffic intensity for specific periods. These maps incorporate statistical data on user activity variations throughout the day and across different land use classes, such as residential areas, streets, and commercial zones. During the morning commute, user intensity is typically concentrated on roads, whereas in the late evening, the majority of users are located in residential buildings. Aligning the time period covered by these maps with the reporting period of a mobile network operator's operations support system allows for the simulation of actual reported average traffic. This alignment facilitates the comparison of different network configurations, such as switched-off cells or altered antenna configurations, under realistic traffic conditions.

The microscopic approach, using individual user traces, allows the simulation of user-driven events, such as handovers, and the evaluation of Key Performance Indicator (KPI) like radio link failures or dropped calls. It also enables the optimization of handover parameters. SiMoNe employs various mobility models to generate realistic, network-wide user traces, ranging from simple random walk patterns to realistic trajectories based on real geographical data. The implemented models include random walk and waypoint mobility, which are based on random directions and velocities, vehicular mobility to account for realistic vehicular user traces, pedestrian and cyclist mobility featuring user traces that start and end at building entrances with realistic movements in between, and a 3D indoor mobility model [56]. This indoor model generates realistic movements, including walking through doors, using elevators, dwelling in certain rooms, and destination-oriented movements from a starting point to a destination, complementing 3D simulations of indoor cells. These diverse models ensure that SiMoNe can provide comprehensive and realistic simulations of user behavior in various scenarios.

As mentioned all computations are organised in the form of functional blocks. Initially, one block provides the scenario data, such as network topology, frequency plan, and network configuration parameters. Subsequently, the "controller" block manages the simulation time, encompassing both macroscopic and microscopic steps, and is followed by the central "signal-strengths" block. Once all subsequent blocks have completed their computations, the controller block advances the simulation by updating the simulation time.

The signal strength at each point in space is calculated based on the transmit power, the gain and pattern of the corresponding antenna, and the pathloss predictions. For macroscopic simulations, these points are organized into a raster grid with a defined spatial resolution and can be represented as a matrix (e.g. in an Referenz Signal Received Power (RSRP) map). A second matrix stores information about the corresponding cell. To account for more than just the strongest layer, the matrices can include several layers, ordered by descending signal strength. In microscopic simulations, these points are defined by the actual positions of the respective trace, with a linear vector representing the signal strength at different positions in an RSRP trace. A second vector contains the cell ID information. To accommodate more than the strongest cell, these vectors are converted into matrices. This approach ensures that both macroscopic and microscopic simulations are treated in a similar manner. Further metrics, such as the Signal-to-Interference-plus-Noise Ratio (SINR), can be calculated based on the RSRP.

Based on the handover-dependent cell assignment of individual users (microscopic case) or cell assignment probabilities (macroscopic case), the traffic demand is allocated to the respective cell. This traffic demand is either user-based (microscopic case) or presented as a map (macroscopic case). To calculate the resulting downlink SINR, an iterative approach is employed, starting with each cell assigned a fixed load value. This load value is used to determine the interfering power of each cell, under the assumption of a linear relationship between cell load and the average transmitted power per used resource. The RSRP and interfering powers provide a preliminary SINR, which is then used to update the actual resource requirements and cell loads using link-level abstractions. These abstractions facilitate the mapping of SINR to spectral efficiency, thereby determining the required amount of resources. This process is repeated until load values converge and a steady state is reached, where all SINR and load values are stable. The link-level abstractions account for the effects of different scheduling and antenna configurations. For uplink computations, only the microscopic approach with discrete users and positions is supported. SINR and load computations, incorporating various scheduling schemes, are performed to enable fast and computationally efficient uplink simulations. Based on the SINR, KPIs such as the Bit Error Rate (BER) can be looked up in tables that are obtained from statistics or the link level simulator (LLS) [52].

In addition to SINR and load value computations in microscopic simulations, SiMoNe incorporates different

handover (HO) procedures, which includes all critical HO events based on 3GPP standards. The process begins with initial cell selection: if the UE enters the scenario or loses the signal, it must execute a cell selection, choosing the best server, i.e., the cell with the strongest RSRP value. Successful HO is logged when a HO to another cell is successfully executed, with the decision based on configurable hysteresis and time-to-trigger value pairs. A ping-pong HO is recorded if the UE reconnects to the previous cell within a predefined time window, with decisions based on adjustable timer values. HO failure occurs if the SINR conditions are too poor during the HO procedure, which can happen if the conditions are too bad in the source cell, preventing the UE from receiving the HO command, or in the target cell, where the UE cannot connect after receiving the HO command. In case of HO failure due to bad SINR conditions at the target cell, a hand back is executed to reconnect the UE with the source cell. A radio-link failure is logged if the UE loses connection to a cell, which can occur if the SINR conditions are too poor for communication between the cell and the UE, or if the RSRP conditions are too weak, placing the UE in a coverage hole [52]. By integrating RIS into the SLS, their impact on network performance can be evaluated, and their deployment and configuration can be optimized. In simulations, RISs can be used to manipulate the wireless propagation environment, enhancing signal strength and coverage in targeted areas. By adjusting the properties of RIS elements, SiMoNe can model various scenarios to assess improvements in metrics such as SINR, data throughput, and user connectivity. Different strategies for RIS placement and orientation to maximize network efficiency and reliability can be reviewed. Additionally, SiMoNe SLS can simulate the dynamic behavior of RISs in response to changing network conditions, providing insights into their effectiveness in real-time adaptive networks.

As next step, we will integrate RIS in the SLS by implementing an additional block in the simulation pipeline. At first, the path loss will be predicted using isotropic path loss. Afterwards, the AoA and AoD at the RIS are determined at runtime by ray tracing and antenna gains based on the angles using the additional block will be assigned. Possible future investigations include updating rates, refining tracking algorithms, analyzing capacity and coverage through maps, developing mobility models tailored for industrial environments, and exploring various placement options as suggested in the literature.

2.6.4 Integrating RIS in Link Level Simulations

The link level simulator within SiMoNe simulates the physical layer and signal processing aspects for one link between a transmitter and a receiver. It intricately examines the transmission and reception of data symbols, meticulously considering factors such as channel impairments, noise, and interference. Armed with coding schemes and modulation presented in [57], it diligently encodes and modulates data for transmission while faithfully modeling various channel phenomena including fading, multipath propagation, and interference. Notably, the simulator supports both hard decision and soft decision detection strategies, as well as different coding schemes like LDPC and RS coding. In essence, the link level simulator plays a pivotal role in assessing and optimizing the performance of wireless communication systems, offering crucial insights into system reliability, latency, and throughput at the physical layer, by simulating the quality of individual connections between transmitters and receivers.

The modular composition of SiMoNe's LLS is fundamental to its adaptability and extensibility, enabling seamless integration of new concepts and technologies as the field of wireless communication evolves. By organizing functionalities into interchangeable blocks and leveraging object-oriented programming principles such as abstract classes and inheritance, the LLS architecture facilitates code reuse and minimizes redundancy. This modular approach not only streamlines development but also enhances the simulator's flexibility to accommodate diverse simulation scenarios and research objectives. In parallel, the LLS employs iterative computations to optimize simulation runtime and resource utilization. Through iterative iterations, the simulator dynamically adjusts the number of simulated bits based on the communication scenario's BER, ensuring statistically significant predictions of system performance while minimizing computational overhead. By discarding transmitted bits after BER calculation, the simulator effectively manages memory resources, allowing for efficient execution of simulations even in scenarios with high BER variability. This iterative approach underscores the LLS's commitment to balancing simulation accuracy with computational efficiency, enabling researchers to conduct comprehensive performance evaluations across a wide range of communication scenarios [50].

The integration of ray tracing results within SiMoNe's LLS is considered a pivotal aspect of its simulation

framework, leveraging advanced ray-optical methods to derive channel information from realistic 3D scenarios. By implementing an interface to the ray tracing framework, the LLS enables the seamless integration of ray tracing data, thereby enriching the simulation environment with detailed channel characteristics such as delay and amplitude. This integration empowers simulation scenarios to be conducted, facilitating comparison with measurement results and enabling insights into scenarios that may be challenging or impractical to access through empirical means. Furthermore, the visualization capabilities of the LLS play a crucial role in interpreting simulation outcomes and facilitating scientific communication. Through tools such as constellation diagrams, eye diagrams, and spectrum plots, various stages of the transmission system can be visually analyzed and interpreted, aiding in the identification of key phenomena and providing valuable insights into system performance. [50]

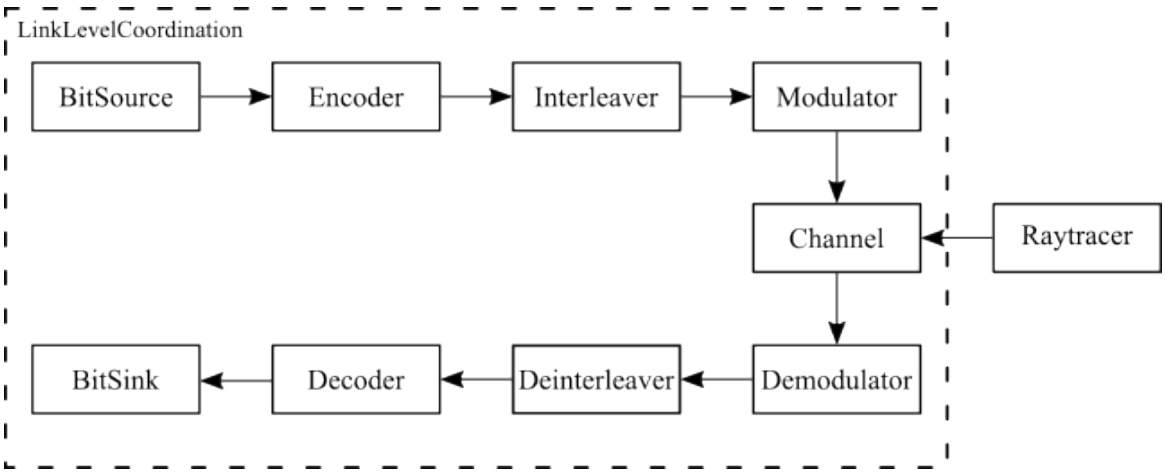

Figure 44: block diagram of the link level simulator in SiMoNe

The link level simulator comprises distinct blocks operating at both the transmitter and receiver sides to emulate the transmission and reception of data, as shown in Fig. 44. At the transmitter side, the process begins with the BitSource-Block, responsible for generating the data bits to be transmitted. These bits are then passed through the Encoder-Block, where error correction coding is applied to enhance the robustness of the transmission. Subsequently, the Interleaver-Block rearranges the encoded bits to mitigate the effects of burst errors. The Modulator-Block then translates the bit sequence into a corresponding waveform suitable for transmission over the channel. In the channel, represented by the Channel-Block, the transmitted signal is subjected to various impairments such as noise, fading, and interference. At the receiver side, the received signal undergoes processing to recover the transmitted data. The Detector-Block first extracts the modulated symbols from the received waveform. The Deinterleaver-Block reverses the interleaving process to restore the original order of the symbols. Finally, the Decoder-Block deciphers the encoded symbols to retrieve the original data bits. The processed bits are then delivered to the BitSink-Block, completing the transmission cycle within the link level simulator.

Since only the Channel-Block is impacted by the RIS implementation, the implementation of this block requires more detailed consideration. The challenge faced by the simulator lies in translating the time-continuous behavior of the channel into the discrete-time domain required for computer simulation. Beginning with the MPCs derived from the ray tracing simulation, represented as pairs of amplitude A_i and delay τ_i, the Channel Impulse Response (CIR) of the propagation channel is constructed as

$$h_C(t) = \sum_i A_i \delta(t - \tau_i), \tag{84}$$

where the amplitude is assumed to be frequency-independent. To adapt this continuous-time expression to discrete-time simulation, the modulation channel incorporates the transmit pulse discussed previously. By convolving the band-limited transmit pulse with the channel impulse response and sampling it at the specified

sampling frequency, the resulting discrete-time channel impulse response is expressed as

$$h_{TX,C} = (g * h_C)[n] = \sum_i A_i A T_S h_{TX}(n\Delta t - \tau_i), \tag{85}$$

where T_S represents the sampling interval, A the amplitude dependent on the transmission power and $g[n]$ the transmit pulse. This discrete-time representation serves as the filter coefficients for a finite impulse response (FIR) filter, implemented using a fast convolution approach. Consequently, the incident signal at the receiver is obtained through the convolution operation $\underline{w}[n] = \underline{d}[n] * h_{TX,C}[n]$, where $\underline{d}[n]$ denotes the sampled complex samples, send by the TX. Importantly, the channel and the transmit filter can be split, allowing these filters to be applied to the signal independently of each other, providing flexibility in the simulation setup. [50]

For the integration of RIS into the LLS, two possible concepts emerge, each offering distinct advantages and limitations. The first approach entails encapsulating all electromagnetic characteristics of a RIS within the antenna diagram of the RIS itself. Using this method, only one channel filter is generated, simplifying the simulation process. However, this approach does not differentiate between MPCs influenced by the RIS and those solely between the TX and RX. Consequently, the first approach lacks the ability to capture the specific impact of individual Radio Frequency (RF) impairments associated with an RIS.

Alternatively, the second approach involves implementing a novel ChannelBlock capable of distinguishing between MPCs influenced by the RIS and those without such influence. Here, two separate channel filters are created: one for MPCs without RIS and another for MPCs with RIS. To calculate the incident signal at the receiver, the outputs of both filters are superimposed. This approach allows for a more nuanced representation of the RIS's impact, enabling the simulation to model RF impairments of the RIS in a more complex manner than merely through an antenna diagram. However, the implementation of this method is more complex and computationally intensive compared to the first approach, potentially leading to longer simulation times. Therefore, while the first approach offers simplicity and faster simulations, the second approach provides greater precision in calculating the impact of an RIS. Further investigation is required to determine which implementation is superior based on the specific requirements and objectives of the simulation. Potential research areas for the LLS extend beyond addressing RF impairments and encompass investigations into Inter-Symbol Interference (ISI), including the refinement of channel estimation techniques and the optimization of RIS illumination strategies.

3 Multi-goal network optimizations and MAC procedures for THz-based mesh network

3.1 Objective and methodology

Following the physical (PHY) layer analysis of RISs, RF impairments, and metaprisms, this section addresses the MAC and network-level aspects of industrial networks. Specifically, this part of the deliverable relates to the project's proposal of an "intelligent and multi-goal mesh network". This concept involves a THz network that interconnects active and passive devices and utilizes intelligent/Artificial Intelligence (AI)-based algorithms to seamlessly satisfy various requirements in different areas of the plant, taking advantage of the link redundancy provided by mesh networking.

For this sake, we consider a factory where different types of sensors are deployed over automation machines to collect meaningful data. Sensors on the machines generate different types of traffic (see Section 3.2.2) with different type of requirements, and send the measured data to a BS, located somewhere in the factory, via wireless links.

From the wireless communication perspective, this scenario is extremely challenging: as identified in our previous deliverables [49, 58], the number of sensors, as well as the corresponding data-rates, produce network throughput that can be as large as tens of Gbit/s, and sensor miniaturization imposes another fundamental constraint. These requirements cannot be fulfilled by current wireless technologies, and this opens up new possibilities, such as using higher frequencies. In particular, the THz band, that is, the interval of frequencies from 0.1 to 10 THz, offers bandwidths of several GHz which provide ultra-high data rates, while sensors miniaturization will benefit from the smaller wavelengths.

However, these advantages are obtained at the cost of very high channel losses that limit the transmission range, even in Line of Sight (LOS) conditions. The latter problem can be partially tackled by means of directional antennas. Due to miniaturization and cost constraints, we assume the sensors have low transmit and receive antenna gains, due to their simplicity. The latter will have two consequences. The first one is that sensors will have very limited sensing range, making the application of Carrier Sense Multiple Access (CSMA) techniques difficult, due to the huge impact of the Hidden Terminal Problem (HTP). The second one is that in an industrial scenario, with many metallic surfaces, the transmission range cannot guarantee direct connectivity between all sensors in the factory and the BS, resulting in the need for deploying a mesh (i.e., multi-hop) topology. Another implication on the network layer protocols of the use of THz frequencies is that the ultra-high bit rates, combined with the short packet lengths typical of Industrial Internet of Things applications, will make packet transmission times shorter than the propagation delays. This fact sets unprecedented issues that, at the MAC layer of the protocol stack, need specific considerations.

In this Section, we present a system model describing the aforementioned scenario, based on two Italian factories (Robopac-Aetna Group and Bi-Rex), a channel model, and the traffic models. Two feasible MAC protocols, based on Unslotted Aloha and Slotted Aloha, are presented, accounting for the real propagation delays. Results report a comparison between the two MAC protocols and the impact of propagation delays on the performance when considering a typical star network topology. Finally, some preliminary results related to a two-hop mesh topology are presented, where we propose an innovative flooding-based extension of the Unslotted Aloha protocol from the MAC layer perspective. Results have been obtained via simulations, through the use of a customized simulator.

It is worth noting that, in alignment with Objective 4 of the TIMES project, these intermediate results propose a MAC layer protocol that supports mesh networking exclusively among active devices. However, we are also developing a scheme to include passive RISs as an additional opportunity for link redundancy. The final subsection also describes the approach we are following in this sense. Intelligent/AI-based optimizations for performance enhancements and link predictions will be addressed in the next deliverable, as we chose to contextualize the motivation for mesh networking and benchmark it against legacy approaches in this first phase.

3.2 System model

In this section, we introduce our system model, emphasizing the network architecture, traffic, deployment, and channel models. This system model, along with the proposed THz network architectures and MAC protocol solutions, have been incorporated into a modular network simulator written in Python. While time is discrete in this simulator, an event-based approach has been adopted to accommodate the short timeframes characteristic of THz networks, which typically operate on the scale of nanoseconds, with the aim of shrinking the simulation timings.

3.2.1 Scenario

We consider a factory floor formed by a pilot line and a remote control unit. Industrial machines are deployed over the pilot line to perform specific tasks (i.e., soldering, milling, assembling, etc.). These machines are equipped with sensors that need to communicate with their Programmable Logic Controller (PLC). Usually, the PLC is connected to the machine by cable. Conversely, we foresee a futuristic approach where the PLC is remote, i.e., is implemented in a server located in the remote control unit of the industry plant. To do so, we consider that each machine's sensor is a UE operating in the THz band.

3.2.2 Traffic model

In light of the above industrial scenario, each UE is categorized based on its traffic model. We foresee three different traffic models, as defined by Work Package (WP)2 [49]:

1. **Real-Time (RT):** It is a fixed periodic traffic, i.e., each UE generates fixed data size, P_{RT}, at predefined time intervals T_{RT};
2. **Camera Node (CN):** This is the traffic produced by the cameras present in the industrial environment and aiming at monitoring the manufacturing processes. Notice that those video streams do not interact with a PLC but still need to reach the remote control unit where the monitoring logic is present. Like RT, CN is a fixed periodic traffic, with both fixed data size P_{CN} and inter-arrival time T_{CN};
3. **Non Real-Time (NRT):** Similarly to RT, this traffic characterizes machines, where the PLC have to gather data from the sensors of the machine and forwards them to an edge computer which is still located in the remote control unit. Specifically, there are two phases:
   (a) *Data collection:* The data are generated with a fixed inter-arrival time $T_{\text{NRT,DC}}$. The data size is also constant but it depends on the machine state. In particular, during a standby period of random duration T_{SB}, which is modeled as an exponential random variable with parameter λ_{SB}, the data size is $P_{\text{NRT,SB}}$, whereas, during the ON period of fixed duration T_{ON}, the data size is $P_{\text{NRT,ON}}$;
   (b) *Data optimization:* The data are generated with a random inter-arrival time $T_{\text{NRT,DO}}$, which is modeled as an exponential random variable with parameter λ_{DO}. The data size is constant and can be $P_{\text{NRT,H}}$ with probability p, or $P_{\text{NRT,L}}$ otherwise.

The result of our implementation of the three traffic types is shown in Figure 45, which portrays the buffer size of a generic UE as a function of the data generation instant and its traffic type. We set $P_{\text{RT}} = 70$ B, $T_{\text{RT}} = 10$ ms, $P_{\text{CN}} = 10$ MB, $T_{\text{CN}} = 8.3$ ms, $\lambda_{\text{SB}} = 50$ arrivals/s, $T_{\text{SB}} = 50$ ms, $P_{\text{NRT,SB}} = 40$ B, $T_{\text{ON}} = 100$ ms, $P_{\text{NRT,ON}} = 200$ B, $\lambda_{\text{DO}} = 0.9$ arrivals/s, $p = 1$, $P_{\text{NRT,H}} = 100$, $P_{\text{NRT,L}} = 50$. The random exponential values (i.e., T_{SB} and $T_{\text{NRT,DO}}$) have been determined as the mean of 100 samples.

From the network perspective, Figure 45 shows that the considered traffic is a mixture of regular (i.e., RT and CN), and irregular (i.e., NRT) patterns with different characteristics (in terms of data size and inter-arrival time) and requirements (e.g., machines' data may require high reliability, whereas video streaming demands for high network throughput). This heterogeneous multi-goal objective is typical of industrial environments and poses tremendous challenges to the mobile radio network design.

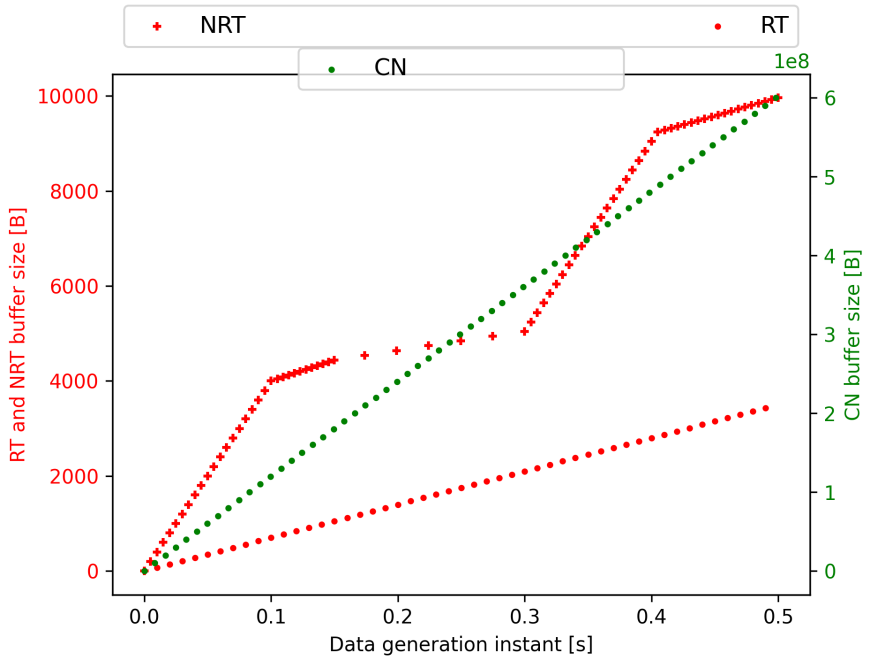

Figure 45: Buffer size as a function of the data generation instant and the three traffic types, namely RT, CN, and NRT. We set $P_{RT} = 70$ B, $T_{RT} = 10$ ms, $P_{CN} = 10$ MB, $T_{CN} = 8.3$ ms, $\lambda_{SB} = 50$ arrivals/s, $T_{SB} = 50$ ms, $P_{NRT,SB} = 40$ B, $T_{ON} = 100$ ms, $P_{NRT,ON} = 200$ B, $\lambda_{DO} = 0.9$ arrivals/s, $p = 1$, $P_{NRT,H} = 100$, $P_{NRT,L} = 50$.

3.2.3 Deployment model

The pilot lines examined in this study are actual Italian plants, namely those belonging to the Robopac-Aetna Group and Bi-Rex. We meticulously modeled and implemented these pilot lines in our network simulator thanks to the information provided by such partners.

Robopac-Aetna Group The Robopac-Aetna plant has a size of $52.36\text{x}35.4\text{x}8.5 m^3$, in which $O = 9$ packing machines of various sizes are placed according to their actual position. For the sake of simplicity, these industrial machines have been modeled as cubes of side 2 m for small machines and 4.2 m for large machines, respectively. To reach the remote control unit, we assume that a THz BS is located at the center of the top base of the factory, as shown in Figure 46.

Bi-Rex The Bi-Rex scenario is a $32.2\text{x}66.24\text{x}6.3 m^3$ plant in which $O = 28$ machines, including printers, assembly, packing, and measurement stations, are placed according to their actual position. For the sake of simplicity, these industrial machines have been modeled as cubes of different sides $\{1, 1.5, 2, 3.5\}$ m. The real plant is equipped with a Non-Public 5G Network; therefore we have placed the THz BS in the exact location of the actual 5G BS, being approximately at the height of 6 meters in one corner, as depicted in Figure 47.

As can be observed, in both scenarios, we assume that UEs generating RT or NRT traffic are randomly distributed across the industrial machines, either inside and along the external machine's surface, whereas CN UEs are located randomly on the walls of the plants.

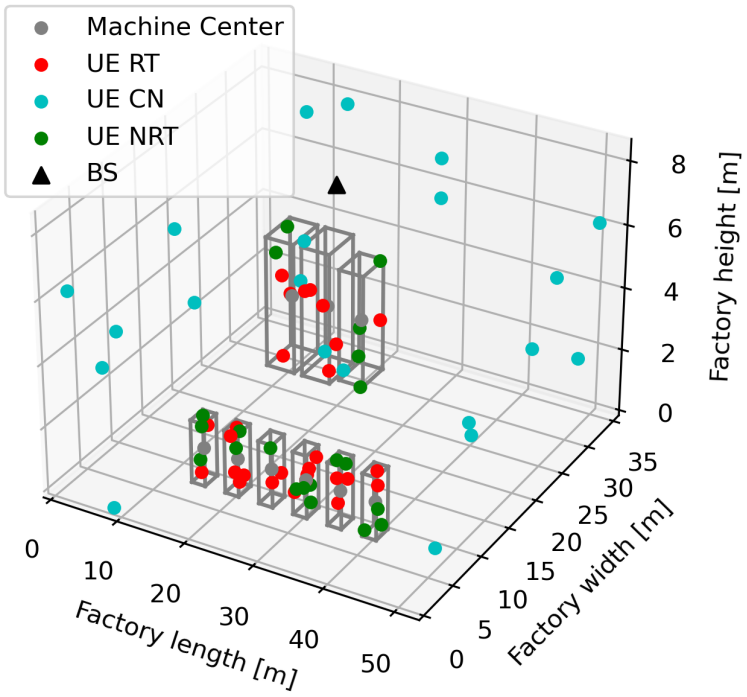

Figure 46: Implementation of the Robopac-Aetna Group pilot line

3.2.4 Channel model

The channel propagation conditions considered for the radio channel modeling follow the Indoor Factory (InF) scenario of the 3GPP TR 38.901 [59]. In particular, the channel is modeled with a narrowband description where the path loss *PL* can be written as follows:

$$PL[dB] = \beta + \alpha log_{10}(d[m]) + \gamma log_{10}(f_c[GHz]) + SH[dB], \tag{86}$$

where d is the Tx-Rx distance, f_c is the carrier frequency, SH represents the Shadowing modeled as a gaussian random variable with zero mean and standard deviation σ, whereas α, β, and γ are real-values that depend on:

- LOS/Non Line of Sight (NLOS) conditions;
- the clutter density of the scenario, either sparse (S) or dense (D). Specifically, the clutter density, (CD), is defined as the ratio between the sum of the area occupied by the machines Am_o, with $o = 1, 2, ..., O$, and the area of the industrial plant Aw, therefore: $CD = \frac{\sum_{o=1}^{O} Am_o}{Aw}$;
- the height of the transmitter, either low (L), if the transmitter is inside a machine, or high (H), if it is located outside the machines.

The signal-to-noise-ratio (SNR) can be then written as:

$$SNR[dB] = P_{tx}[dBW] + \eta_{tx}[dB] + \eta_{rx}[dB] + G_{tx}[dB] + G_{rx}[dB] - PL[dB] - P_n[dBW], \tag{87}$$

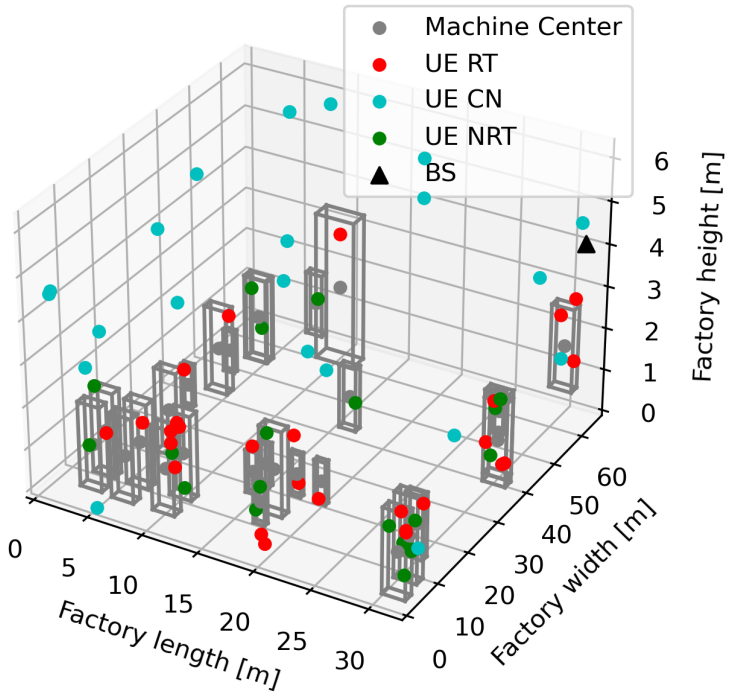

Figure 47: Implementantion of the Bi-Rex pilot line

where P_{tx} is the transmitted power, η_{tx}, η_{rx} are the transmitter and receiver antenna efficiencies, respectively, G_{tx}, G_{rx} are the transmitter and receiver gains, PL is the path loss, and $P_n = kT_0FB$ is the noise power, with k being the Boltzmann constant, T_0 is the reference temperature of 290 K, F is the noise figure of the receiver, and B is the bandwidth. In particular, a successful decoding happens when the SNR overcomes a given threshold SNR_{th}, that is, $SNR \geq SNR_{th}$. In this regard, Figures 48 and 49 provide a quantitative idea of the SNR values characterizing the Robopac-Aetna and Bi-Rex scenario in a 2D fashion, with and without shadowing, where we consider the downlink transmission from the BS to the different UEs in the best-case of LOS conditions. We set $P_{tx} = 32$ dBm, $G_{tx} = 14.5$ dB, $G_{rx} = 14$ dB, $f_c = 300$ GHz, $B = 25$ GHz, $\eta_{tx} = 0$ dB, $\eta_{rx} = 0$ dB, and $F_{rx} = 8.5$ dB.

The SNR_{th} values are then computed starting from the requirement on the success probability at the PHY layer, p_{phy}, whose expression is as follows:

$$p_{\text{phy}} = 1 - BLER, \tag{88}$$

where $BLER$ represents the Block Error Rate, defined in Eq. 89, particularly when considering Automatic Repeat Request (ARQ) as the error correction technique.

$$BLER = 1 - (1 - BER)^P, \tag{89}$$

where BER represents the Bit Error Rate and P is the size of the message in bits. By assuming an M-QAM modulation scheme, the BER can be calculated as follows:

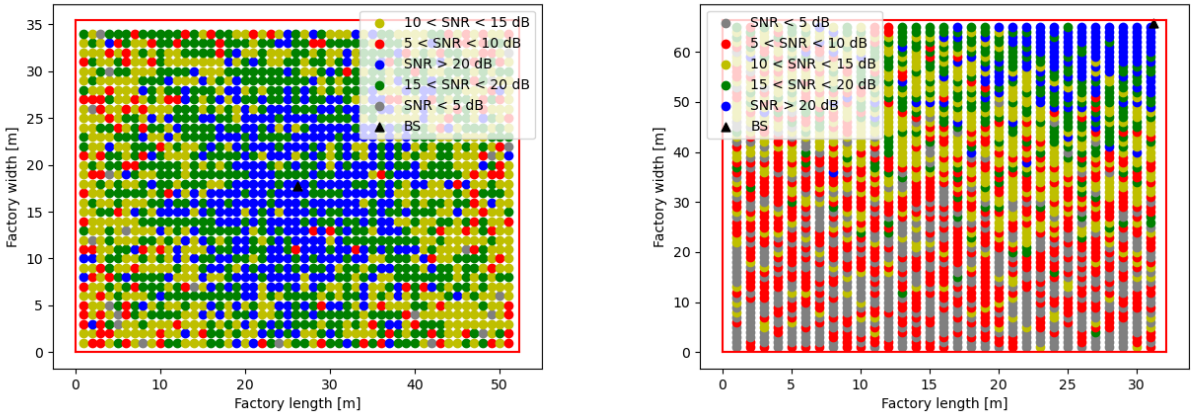

(a) Robopac-Aetna scenario

(b) Bi-Rex scenario

Figure 48: SNR values characterizing the Robopac-Aetna and Bi-Rex scenario according to the LOS InF 3GPP model and with shadowing.

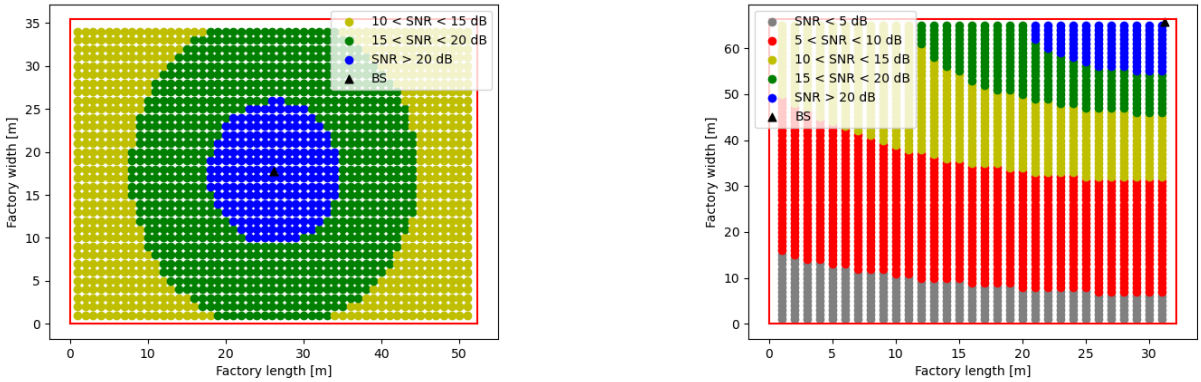

(a) Robopac-Aetna scenario

(b) Bi-Rex scenario

Figure 49: SNR values characterizing the Robopac-Aetna and Bi-Rex scenario according to the LOS InF 3GPP model but without shadowing.

$$BER = \frac{L-1}{L\,log_2 L} erfc\left(\sqrt{\frac{log_2 L}{(L-1)^2} SNR}\right), \tag{90}$$

where $L = \sqrt{M}$ is the level of modulation.

Hence, starting from a p_{phy} requirement, it is possible to define a minimum SNR, SNR_{th}, that allows to obtain such p_{phy} value. Indeed, given three reasonable values of p_{phy} calculated at the BS side, Table 6 presents the corresponding SNR_{th} data of the BS-UE link in LOS condition. Here, we consider the uplink direction of communication from the UEs to the BS and we set $P_{tx} = 30$ dBm, $G_{rx} = 14.5$ dB, $f_c = 300$ GHz, $B = 25$ GHz, $\eta_{tx} = 0$ dB, $\eta_{rx} = 0$ dB, and $F_{rx} = 8$ dB. Additionally, the table showcases the required G_{tx} levels for covering either the entire industrial plant (denoted as $G_{tx|d_{max,Aetna}}$ for the Robopac-Aetna layout, where $d_{max,Aetna} = 32$ m, and $G_{tx|d_{max,Bi-Rex}}$ for the Bi-Rex scenario, where $d_{max,Bi-Rex} = 73$ m) or half of it (represented as $G_{tx|\frac{d_{max,Aetna}}{2}}$ for

Table 6: Success probability at the PHY layer, p_{phy}, as a function of the transmitter gain, G_{tx}, and the maximum or half-maximum distance of the two considered scenarios, Robopac-Aetna and Bi-Rex.

p_{phy}	SNR_{th}	$G_{tx\|d_{max,Aetna}}$	$G_{tx\|\frac{d_{max,Aetna}}{2}}$	$G_{tx\|d_{max,Bi-Rex}}$	$G_{tx\|\frac{d_{max,Bi-Rex}}{2}}$
0.9	7.13 dB	11.89 dB	5.42 dB	19.59 dB	13.12 dB
0.95	7.65 dB	12.42 dB	5.95 dB	20.12 dB	13.65 dB
0.99	8.66 dB	13.43 dB	6.96 dB	21.13 dB	14.66 dB

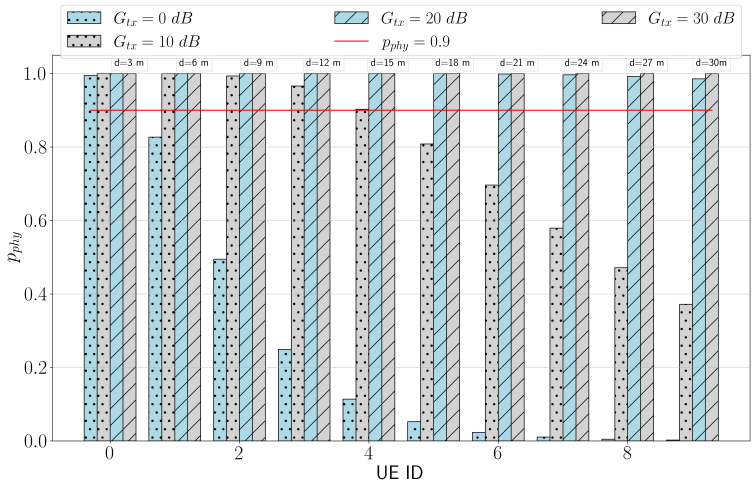

Figure 50: p_{phy} as a function of the transmitter gain, G_{tx}, and the UE ID, where each UE is located at a different distance d from the BS. The distance d for each UE is indicated at the top of each x-axis value. The p_{phy} requirement is 0.9.

the Robopac-Aetna layout, where $\frac{d_{max,Aetna}}{2} = 16$ m, and $G_{tx|\frac{d_{max,Bi-Rex}}{2}}$ for the Bi-Rex scenario, where $\frac{d_{max,Bi-Rex}}{2} = 36.5$ m). Notably, under our specified conditions, achieving a satisfactory success probability at the PHY layer for covering the entire warehouses necessitates directive gains exceeding 10 dB and 20 dB for Robopac-Aetna and Bi-Rex layouts, respectively.

To further extend these preliminary considerations on coverage, Figures 50, 51, 52 illustrate the p_{phy} variation for the scenarios when shadowing and fading are considered in LOS condition. Here we consider the uplink direction of communication from the UEs to the BS again and we set $P_{tx} = 30$ dBm, $G_{rx} = 14.5$ dB, $f_c = 300$ GHz, $B = 25$ GHz, $\eta_{tx} = 0$ dB, $\eta_{rx} = 0$ dB, and $F_{rx} = 8$ dB. Additionally, the p_{phy} values are averaged over 10^5 samples. UEs are randomly distributed in the pilot line and G_{tx} is taken from the set $\{0, 10, 20, 30\}$ dB. Every x-axis corresponds to a given UE ID, that is, a different BS-UE distance, which is reported at the top of the bars, whereas every plot is characterized by a different p_{phy} requirements of 0.9, 0.95, and 0.99, respectively, that in turn results in SNR_{th} of $\{7.13, 7.65, 8.66\}$ dB (see Table 6). The results confirm that the p_{phy} decreases by increasing the UE-BS distances and that high gains (20/30 dB) are needed to meet the p_{phy} requirements of 0.9, 0.95, and 0.99, respectively, for sufficiently high Tx/Rx distance $d > 6$ m. Remarkably, with these high gains, the Robopac-Aetna scenario can be covered entirely, while the Bi-Rex layout only partially. However, these results have been obtained under LOS conditions, whereas most of the UEs are located inside machines (i.e., in NLOS). Therefore, it is expected that lower p_{phy} values will be reached compared to those observed in Fig. 50, 51, and 52, resulting in shorter transmission ranges. This statement motivates the need to investigate mesh networking at THz frequencies.

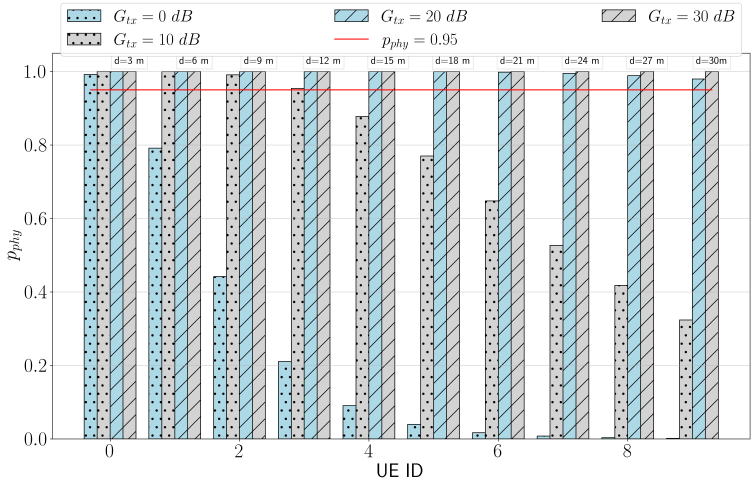

Figure 51: p_{phy} as a function of the transmitter gain, G_{tx}, and the UE ID, where each UE is located at a different distance d from the BS. The distance d for each UE is indicated at the top of each x-axis value. The p_{phy} requirement is 0.95.

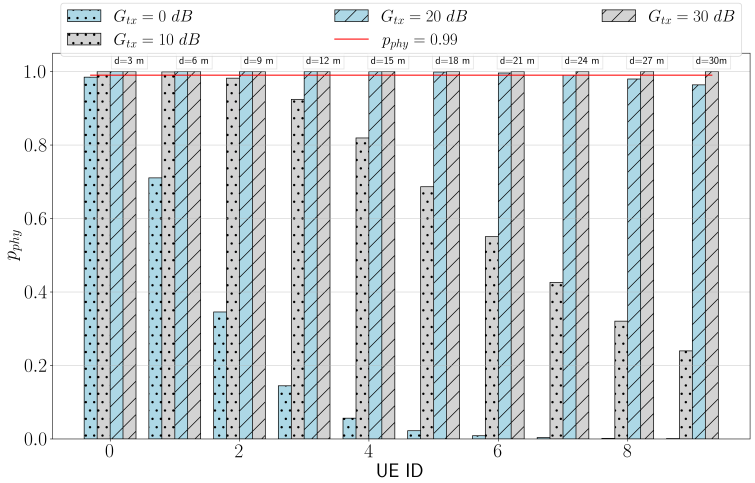

Figure 52: p_{phy} as a function of the transmitter gain, G_{tx}, and the UE ID, where each UE is located at a different distance d from the BS. The distance d for each UE is indicated at the top of each x-axis value. The p_{phy} requirement is 0.99.

3.2.5 Network architecture

We foresee two main THz-based network architectures:

1. **Star:** This is the benchmark and straightforward network architecture where the UEs communicate directly with the BS.
2. **Mesh:** In this case, UEs can both communicate directly with the BS and with other UEs. All UEs that receive data from the others must forward the receptions directly to the BS, together with any of their own data. This is because the objective of the communication remains to connect UEs with the PLC located in the remote control unit, thereby the mesh is characterized by a fixed destination to be reached (i,e, the BS).

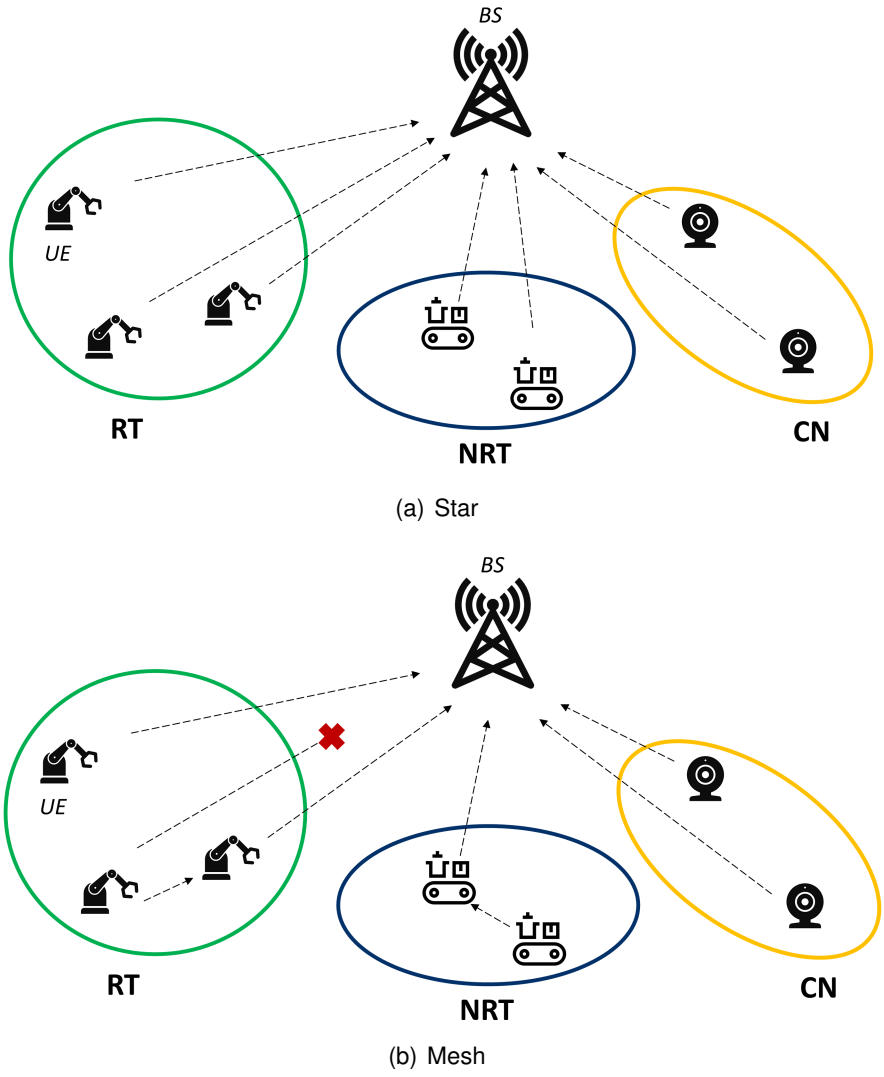

Figure 53: Exemplary plot of the considered THz-based network architectures within the multi-goal industrial framework.

An exemplary plot can be found in Figure 53. Besides the star topology of Figure 53(a), the mesh depicted in Figure 53(b) shows that a UE may need (at least) an additional hop to reach the BS due to (i) unfavorable propagation conditions (as the case for the depicted RT UE) or (ii) capacity issues (as the case for the depicted NRT UE). Details on the MAC protocol tailored for such THz-based network architectures are presented in the following section.

3.3 Network layer protocol

3.3.1 MAC layer

In order to save energy we consider a very simple protocol based on Unslotted Aloha, where a random Back-Off (BO) is added with the aim of reducing packet collisions.

In particular, the protocol works as follows: each UE is in IDLE mode and, as soon as it has a data packet ready to be transmitted in the MAC queue, it will initiate BO for a random number of time slots, T_{BO}, in the

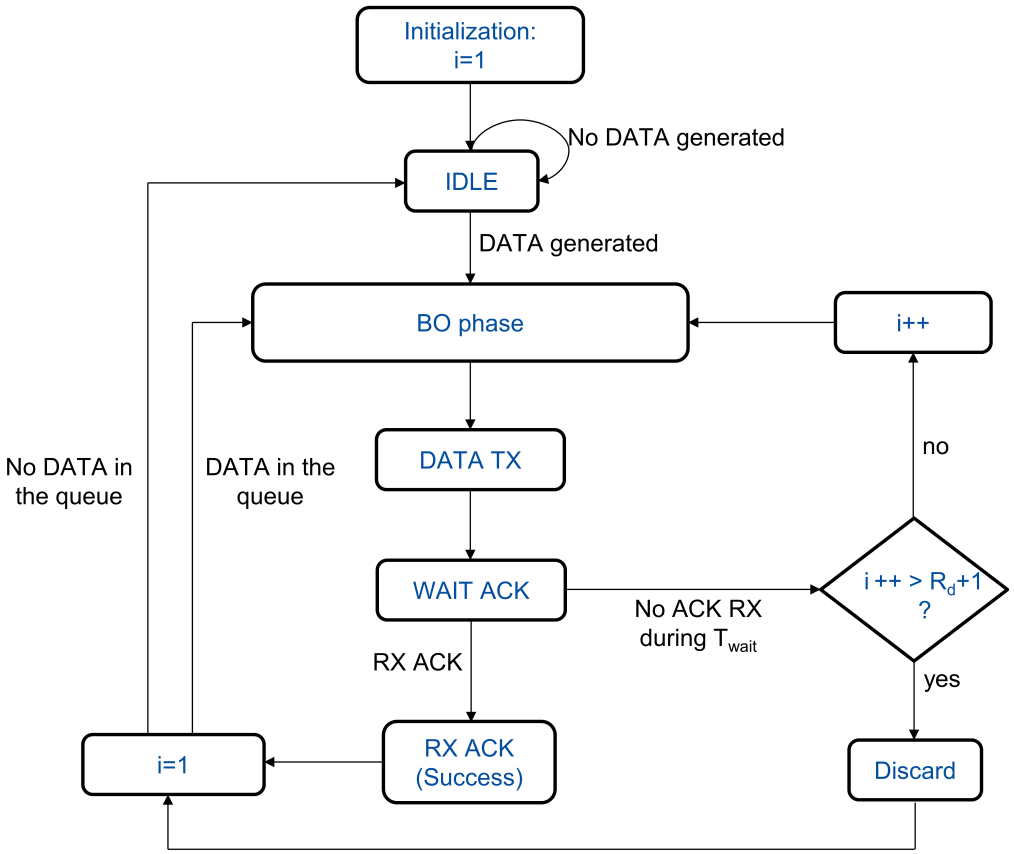

Figure 54: UE state diagram for the Unslotted Aloha protocol.

range $[1; 2^i C]$, where $2^i C$ is the maximum duration of the contention window (C is an integer number), while i is another integer number which counts the number of transmissions attempts (i is set to 1 for the first transmission attempt). At the end of the BO period, the UE sends the data packet and it goes in reception mode for a maximum amount of time, T_{WAIT}. In case an Acknowledgment (ACK) is received, the UE goes back to BO, if a new data packet is already in the queue, or to IDLE, if no data packet is in the queue. If the ACK is not received the UE retries the transmission of the data packet up to a maximum number of time, R_d.

Fig. 54 represents the aforementioned UE state diagram. The time spent in each state is set as follows: $T_{\text{IDLE}} = T_{\text{BO}} = 1.6$ ns, $T_{\text{ack}} = P_A\, 8/R_b$, being P_A the number of bytes in the ACK packet and R_b the bit rate, $T_{\text{data}} = P\, 8/R_b$, where P is the data packet size in bytes; finally $T_{WAIT} = T_{\text{ack}} + 2\,\tau_{p_{max}}$, where $\tau_{p_{max}}$ is the maximum propagation delay possible in the considered scenarios.

Collisions are computed at the BS side, accounting for the real propagation delay between the transmitter UE and the BS, τ_p. If two (or more) packets are received at the BS partially or completely overlapped in time (see Figure 55 on the right) data packets are all considered as lost (no packet capture model is considered actually). In addition, we assume the BS is working in half-duplex mode, that is, if it receives a data packet when it is busy with the transmission of an ACK, the packet is discarded (see Figure 55 on the left).

In order to decrease collisions, at the expense of energy consumption and throughput, also the case of Slotted Aloha has been considered. The protocol works exactly in the same way as described before, with the exception that time is divided into slots, of duration $T_{slot} = T_{data} + \tau_{p_{max}}$, and each time a UE has to change a state it should locate the boundary of the next slot (see Figure 56). In such case we set $T_{\text{IDLE}} = T_{\text{BO}} = T_{slot}$. Note that the presence of large propagation delays, different from UE to UE, may decrease the collision probability in this slotted protocol. Indeed, frames (data or ACK) that are sent at the beginning of the same slot may do not result

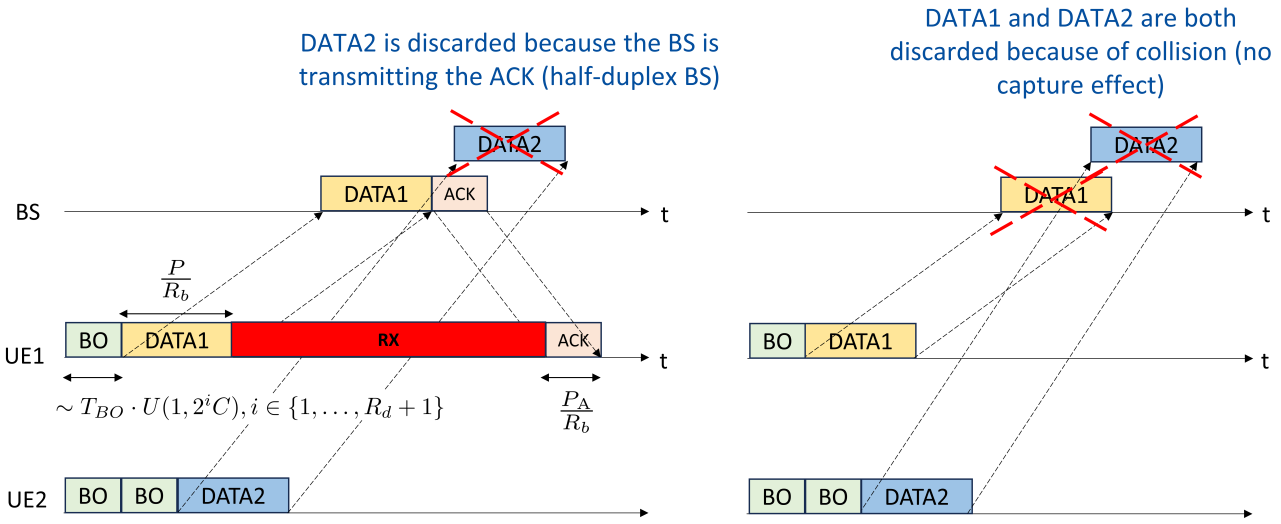

Figure 55: Unslotted Aloha: Examples of data packet losses.

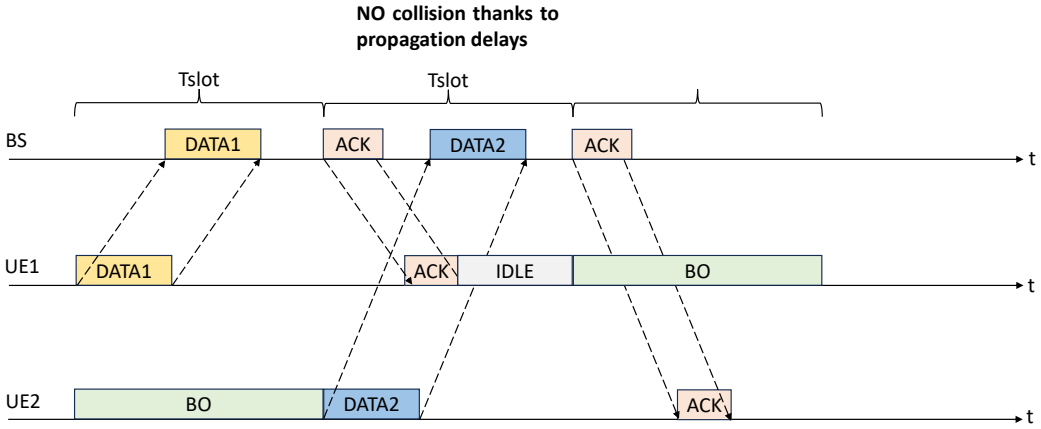

Figure 56: Slotted Aloha: Example of data packets transmission without losses thanks to the propagation delays.

in collision, since they are received not overlapped in time at the receiver side. Examples are given in Figure 56, for the case of ACK and data transmission and in Figure 57 for the case of two data transmissions.

3.3.2 Mesh formation

To provide an initial assessment of mesh networking at THz frequencies, we propose a flooding-based extension of the Unslotted Aloha MAC protocol, summarized in Figure 58. The key innovation is that UEs enter reception mode during BO, resulting in a longer BO duration to ensure a possible reception of data even in the worst case. Consequently, we set the BO duration equal to $T_{\mathrm{B}} = T_{\mathrm{data}} + \tau_{\mathrm{p_{max}}} + T_{\mathrm{BO}}\,\xi$, where ξ represents the

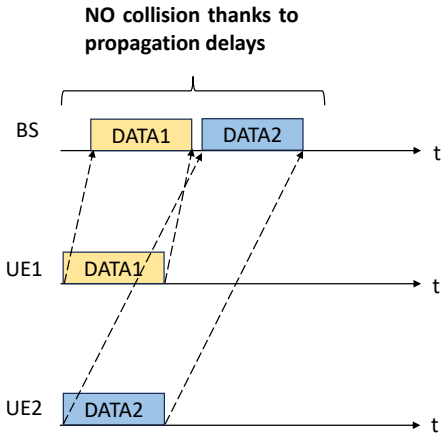

Figure 57: Slotted Aloha: Example of data packets transmission without losses thanks to the propagation delays.

random number of time slots in the range $[1; 2^i C]$. If during BO the UEs correctly receive a data packet that has not yet been forwarded to the BS by another UE and the number of data packets in the MAC layer queue is below its capacity Q, they will enqueue it. Like the BS, UEs will immediately acknowledge successful reception with an ACK. They will then transmit the data in the MAC layer queue, including both their own data and those to be forwarded. Notably, the portion of the transmission containing forwarded data is intended exclusively for the BS and will be discarded by other UEs, while the remaining data is sent in broadcast.

In this flooding-based extension of the Unslotted Aloha MAC protocol, it is confirmed that, after data transmission, UEs go in reception (i) until an ACK is received or (ii) for a maximum amount of time T_{WAIT}. However, in this mesh networking, a UE can receive an ACK, either by the BS or other UEs, which may not be intended for such UE and that should be discarded. The BS should do the same, as it might receive duplicated data packets from different UEs.

Another important note is that during T_{WAIT}, UEs can also receive data from other UEs. In this case, they will enqueue the reception if their MAC layer queue does not already contain Q data packets and this transmission is not intended for the BS. After any reception, the UEs will continue waiting until the reception of the right ACK or when T_{WAIT} ends. At the end of the WAIT phase, each UE will transmit the ACKs relative to all the receptions, if any, and it will check the MAC layer queue. If it is empty, the UE will return in IDLE, otherwise, it will perform data transmission, and the MAC protocol starts again.

Figure 59 illustrates an example of the aforementioned approach, considering two UEs, UE1 and UE2, transmitting DATA1 and DATA2, respectively. In particular, the figure assumed that the former is in BO when the latter transmits DATA2, thereby enabling mesh networking according to the proposed variant of the Unslotted Aloha MAC protocol. In particular, Figure 59 depicts an exemplary timing diagram of (i) the considered Unslotted Aloha MAC protocol when applied to the benchmarking star topology (see Fig. 59(a)), i.e., when UE1 do not set the reception mode during BO, (ii) the aforementioned flooding-based extension of the Unslotted Aloha MAC protocol when the BS is capable of receiving DATA1 and DATA2 (two times) from both UEs (see Fig. 59(b)), (iii) same as case (ii) but when the BS receives DATA1 and DATA2 only from UE1 because there is a link failure with UE2 (see Fig. 59(c)). As can be seen, the BS sends cumulative ACKs when correctly receives

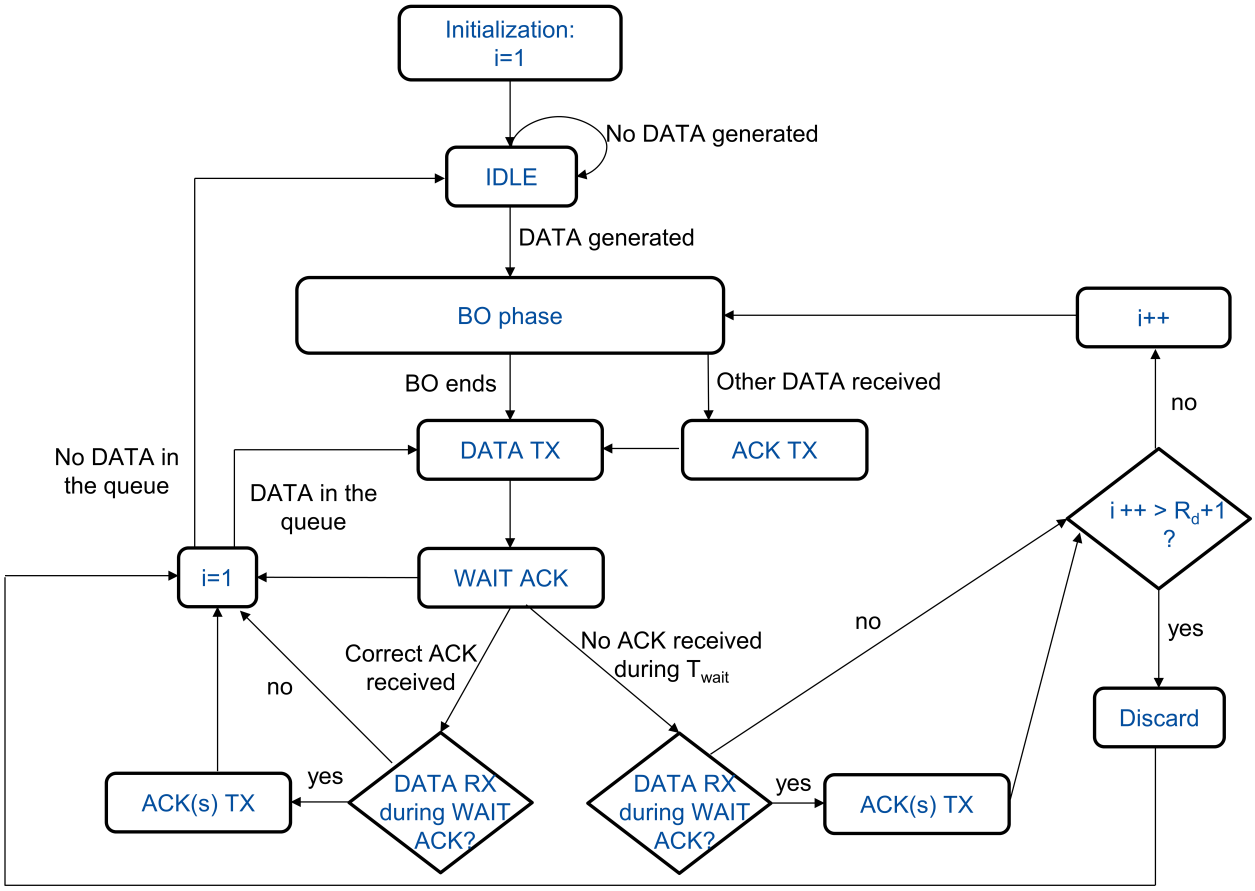

Figure 58: UE state diagram for the proposed flooding-based extension of the Unslotted Aloha protocol, enabling mesh networking. Some details, such as the criteria for accepting data/ack receptions and discarding data packets from other UEs, are omitted for simplicity.

DATA1 and DATA2 in a single reception (i.e., the cases shown in Figs. 59(b) and 59(c)).

3.4 Key Performance Indicators

In this section, we present the KPIs that have been utilized to validate the proposed MAC protocols' design (see Section 3.3.1) within our THz-based system model (see Section 3.2).

3.4.1 Success probability

The success probability, p_s, is defined as the ratio between the average number of data successfully received at the PHY and MAC layers of the BS, and the total number of data transmitted by the UEs, that is,

$$p_s = \frac{1}{N} \sum_{i=1}^{N} \frac{N_{RX_i}}{N_{TX_i}}, \tag{91}$$

where N is the total number of UEs, N_{RX_i} is the number of data successfully received at the BS by the i-th UE, and N_{TX_i} is the number of data transmitted by the i-th UE. We then recall that a data packet is deemed

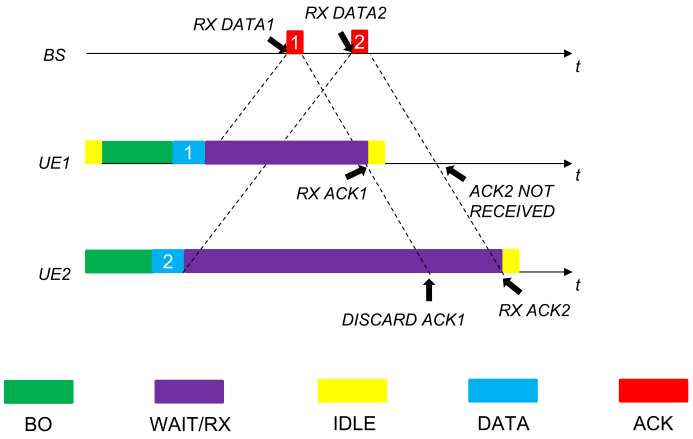

(a) Unslotted Aloha-based star topology working principle.

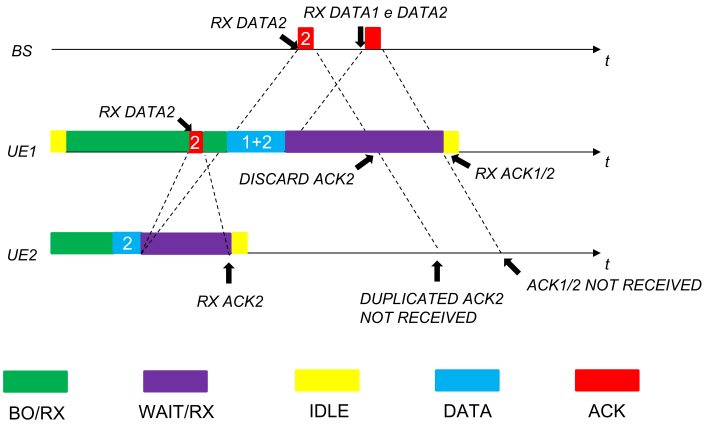

(b) Unslotted Aloha-based mesh topology working principle when the BS successfully receives the data coming from UE2.

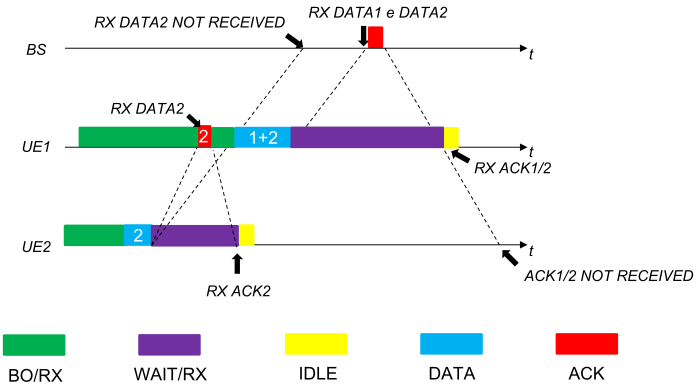

(c) Unslotted Aloha-based mesh topology working principle when the BS does not successfully receives the data coming from UE2.

Figure 59: Examplary timing diagram of the Unslotted Aloha-based star and mesh networking working principle.

successfully received at the PHY and MAC layers of the BS when its $SNR \geq SNR_{\text{th}}$ and it has not collided with any other transmission.

3.4.2 Network Throughput

The network throughput, S, is defined as the number of information bits per second successfully received at the MAC layer of the BS, that is,

$$S = \frac{P\, N_{\text{R}}}{T_{\text{S}}}, \tag{92}$$

where P is the data size, N_{R} is the number of data successfully received at the BS, and T_{S} is the simulation time.

3.4.3 Latency

The average latency, $\overline{L}$, is defined as the average time needed by UEs to transmit data with success, that is,

$$\overline{L} = \frac{1}{N} \sum_{i=1}^{N} \frac{1}{N_{\text{P}_i}} \sum_{j=1}^{N_{\text{P}_i}} L_{i,j} \tag{93}$$

where N is the total number of UEs, N_{P_i} is the number of data packets generated by the i-th UE and not discarded, and $L_{i,j}$ is the time interval from the generation of the j-th data by the i-th UE to the reception of the corresponding ACK. It is worth mentioning that a UE discards a data packet when the number of retransmissions has overcome a given threshold R_{d}. Note that, in mesh networking, UEs can receive ACKs from other UEs acting as relays to the BS. In this scenario, when the BS successfully receives the data from the first relay, it calculates the latency for that packet, denoted as $L_{i,j}$, by summing the time required for the transmission of the ACK to the UE that generated the data packet and the propagation delay of the ACK. This approach ensures fairness between star and mesh computations. Indeed, it is important to note that the ACK sent by the BS is likely not received by the originating UE, as it is not in reception mode, having already received a confirmation from the first relay.

3.4.4 Energy consumption

The average energy consumption, $\overline{E}$, is defined as the average energy consumed by UEs, that is,

$$\overline{E} = \frac{1}{N} \sum_{i=1}^{N} \frac{1}{N_{\text{P}_i}} \sum_{j=1}^{N_{\text{P}_i}} E_{i,j}, \tag{94}$$

where N is the total number of UEs, N_{P_i} is the number of data generated by the i-th UE, and E_j is the energy consumed by the i-th UE to transmit the j-th data packet. Notice that we consider the energy consumption for all the actions taken by the i-th UE to transmit the j-th data. This includes retransmissions, BO periods, reception of ACKs, etc.

3.5 Numerical Results

In this deliverable, our aim is to analyze the achievable network performance under the worst-case scenario of offered traffic. This scenario occurs when the buffers of the UEs are consistently full, meaning the UEs

Table 7: Simulation parameters.

Parameter	Description	Value
$P_{\text{tx,UE}}$	Power transmitted from a UE	30 dBm
$P_{\text{tx,BS}}$	Power transmitted from the BS	32 dBm
G_{UE}	Antenna gain of a UE	14 dB
G_{BS}	Antenna gain of the BS	14.5 dB
B	Bandwidth	25 GHz
F_{UE}	UE noise figure	8.5 dB
F_{BS}	BS noise figure	8 dB
SNR_{th}	SNR threshold	7.13 dB
C	Integer value defining the BO period	5
R_{d}	Maximum number of data packet retransmissions	3
P_{A}	Size of ACK packet	10 B
P	Size of data packet	20 B
Q	Length of the MAC layer queue of UEs	4 data packets
f_{c}	Carrier frequency	300 GHz
R_{b}	UE bit rate	50 Gbit/s
T_{BO}	Back-off minimum time slot duration	1.6 ns
N_{s}	Number of simulations	10
T_{S}	Simulation time	50 ms
W_{BO}	Power consumed in BO (star architecture)	0.1 mW
W_{TX}	Power consumed in transmission	1 mW
W_{RX}	Power consumed in reception	0.5 mW
W_{IDLE}	Power consumed in IDLE	0.1 mW

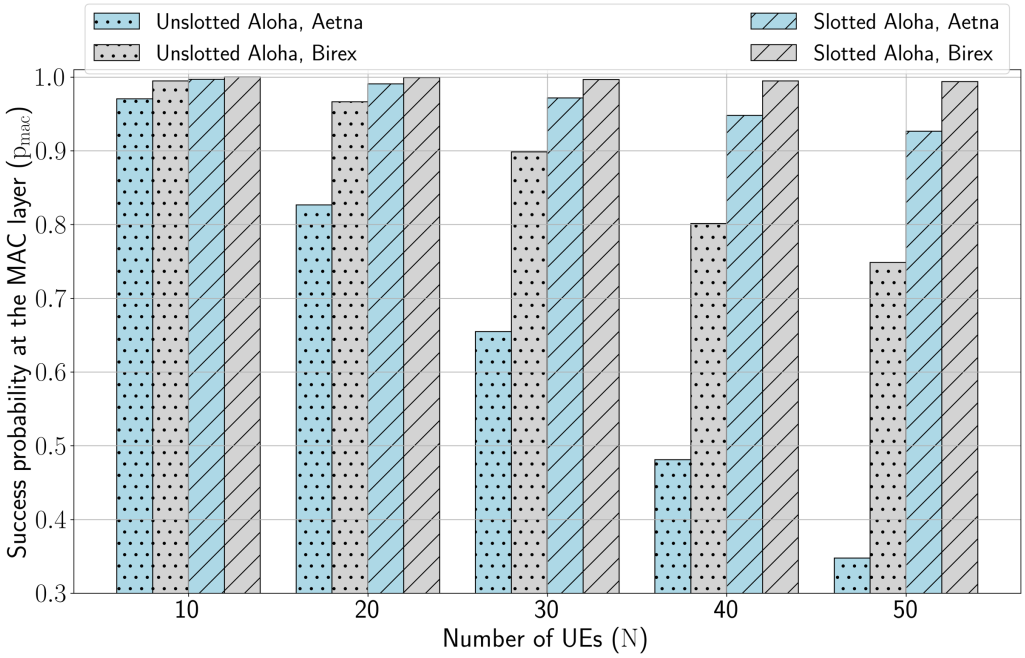

Figure 60: Success probability at the MAC layer, p_{mac}, as a function of the number of UEs, N, the MAC protocol (either Slotted or Unslotted), and pilot line layout (either Robopac-Aetna or Bi-Rex).

always have data awaiting transmission to the BS, resulting in a null inter-arrival time. This analysis is crucial for evaluating the network throughput of a THz network, as this metric is dependent on the traffic type. Therefore, moving forward, we will operate under the assumption that all UEs generate traffic with a fixed size P. Additionally, it is important to note that we also account for the worst-case scenario from an interference standpoint. Specifically, as stated in Section 3.3.1, we do not incorporate any capture effect (i.e., we consider an infinite capture threshold), meaning that all collisions result in the loss of colliding data packets regardless of their respective power levels or the type of collision (partial or total).

All the KPIs introduced in Section 3.4 are numerically evaluated as a function of different input parameters. All results have been obtained by averaging over N_S simulations of duration T_S. Simulation parameters, if not otherwise specified, are reported in Table 7. Specifically, for simplicity, we assume that all UEs are multiplexed within the same bandwidth $B = 25$ GHz, centered in the carrier frequency $f_c = 300$ GHz and the bit rate can be computed as $R_b = B\,log_2(M) = 50$ Gbit/s, since we are considering a 4-QAM modulation scheme. While this assumption may influence the numerical results, the primary objective of this deliverable is to provide an initial assessment of network optimizations and MAC procedures for THz-based networks (where both mesh and star topology are considered). Consequently, we will defer more refined considerations to the subsequent version of the deliverable.

In the following, we present numerical results pertaining to both THz-based star and mesh networks for industrial environments.

3.5.1 Performance of a THz-based star network

To assess the performance of a THz-based star network, we consider $G_{BS} = 25$ dB. This implies that in both the Robopac-Aetna and Bi-Rex layouts, all UEs have an $SNR \geq SNR_{th}$, indicating they can directly communicate with the BS. Consequently, data packets are lost only due to MAC layer issues, such as collisions with other data packets. Based on this, it is possible to directly evaluate the success probability at the MAC layer, p_{mac}, as the ratio between the average number of data packets successfully received at the MAC layer of the BS, and

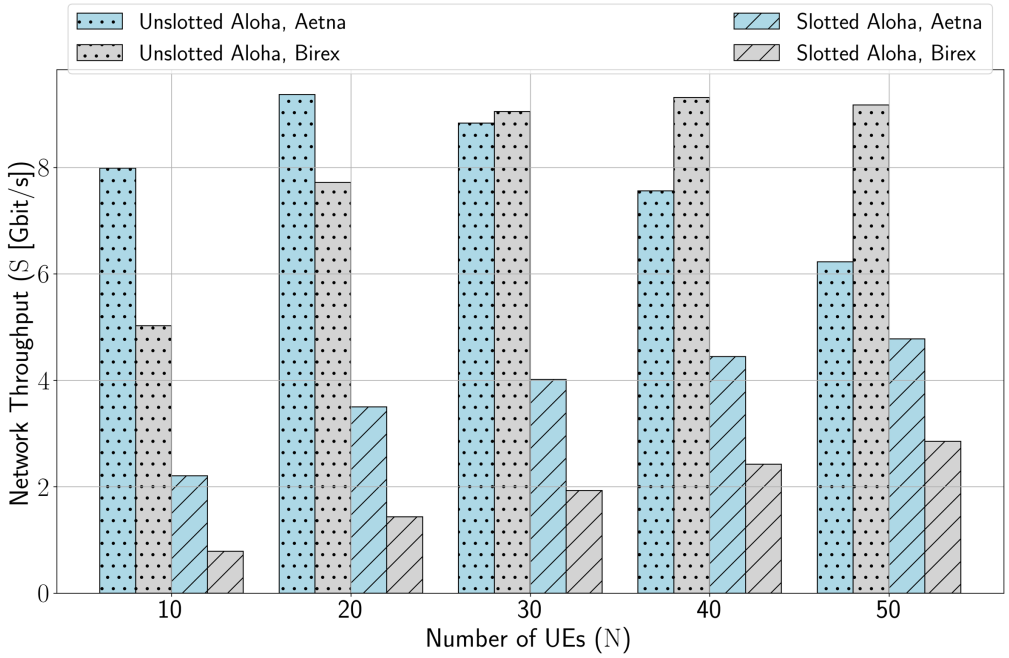

Figure 61: Network throughput at the MAC layer, S, as a function of the number of UEs, N, the MAC protocol (either Slotted or Unslotted), and pilot line layout (either Robopac-Aetna or Bi-Rex).

the total number of data packets transmitted by the UEs.

We start the analysis with Figure 60, where the p_{mac}, is portrayed as a function of the number of UEs, N, the MAC protocol (either Slotted or Unslotted), and pilot line layout (either Robopac-Aetna or Bi-Rex). As expected, the decreasing trend of p_{mac} is confirmed. Moreover, Slotted Aloha outperforms Unslotted Aloha due to the halving of the contention window. However, it is noteworthy that the Bi-Rex layout contributes to performance enhancement. This is attributed to the wider environment compared to the Robopac-Aetna pilot line (see Section 3.2.3), resulting in longer propagation delays that enhance the success probability. In essence, it is more probable that UEs transmitting data packets simultaneously would not collide, as the BS receives them at distinct time intervals. This result demonstrates that the design of MAC protocols at THz frequencies should also account for propagation delays.

Then, Figure 61 shows the network throughput at the MAC layer, S, as a function of the number of UEs, N, the MAC protocol (either Slotted or Unslotted), and pilot line layout (either Robopac-Aetna or Bi-Rex). As well-known from the Aloha theory, there exists an optimum value for network throughput based on the offered traffic (in this case, we are just varying the number of UEs). This holds true for Unslotted Aloha but not for Slotted Aloha, as it can accommodate a larger number of UEs — more than 50 — due to its superior performance in terms of success probability, and thereby the optimum point is not visible for this MAC protocol.

By focusing on the Unslotted Aloha performance, it can be seen that such optimal condition is observed to be lower for the Robopac-Aetna layout w.r.t the Bi-Rex one, owing to the increased collision probability resulting from lower propagation delays. In particular, the dual effect stemming from reduced propagation delays provided by the Robopac-Aetna scenario — a heightened collision probability alongside a decrease in overall transmission time — introduces a tradeoff. Notably, this causes a reversal in the network throughput trend when $N \geq 30$, that is, the network throughput is higher for the Robopac-Aetna layout when the number of UEs is lower than 30.

Additionally, it can also be seen that, despite Unslotted Aloha exhibiting a lower success probability, it outperforms Slotted Aloha. This is attributed to its lack of synchronization, leading to prolonged timings that have a more detrimental effect.

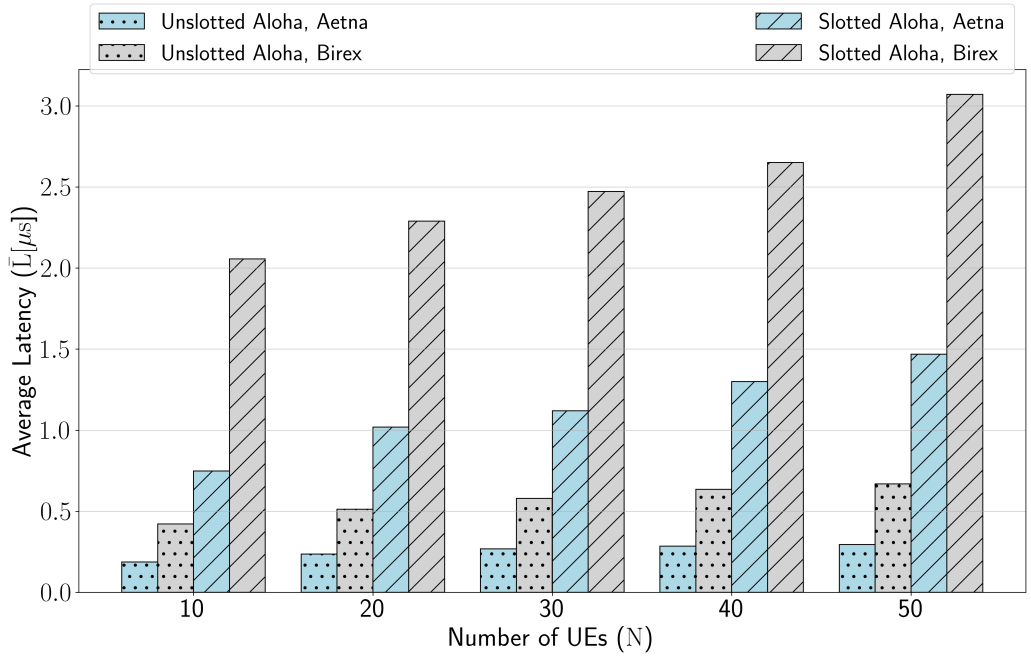

Figure 62: Average latency, $\overline{L}$, as a function of the number of UEs, N, the MAC protocol (either Slotted or Unslotted), and pilot line layout (either Robopac-Aetna or Bi-Rex).

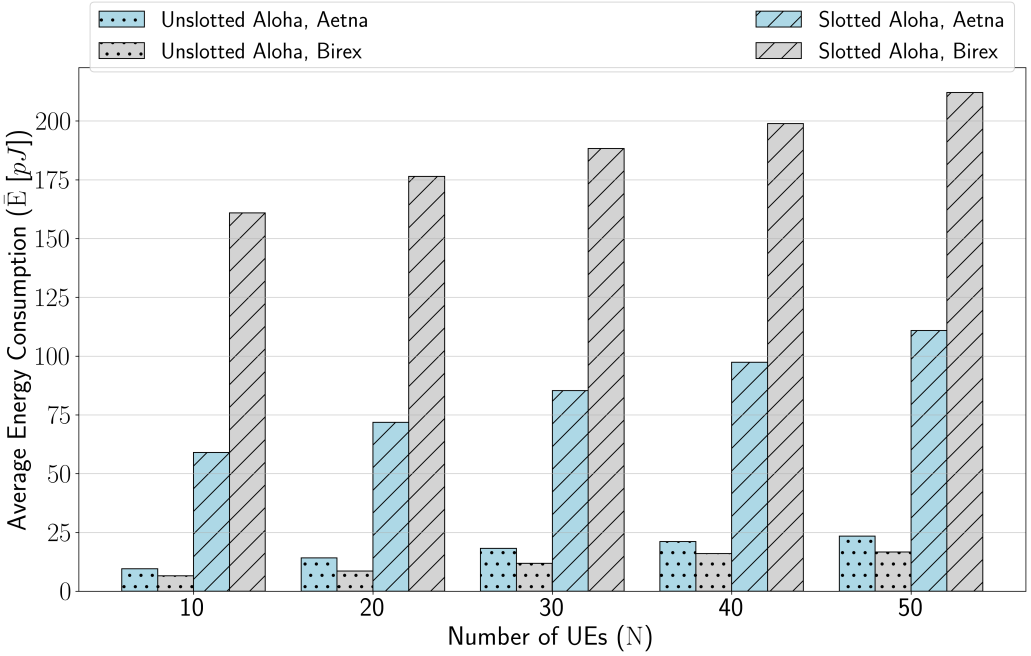

Figure 63: Average energy consumption, $\overline{E}$, as a function of the number of UEs, N, the MAC protocol (either Slotted or Unslotted), and pilot line layout (either Robopac-Aetna or Bi-Rex).

Figures 62 and 63 conclude the performance analysis of our THz-based star network by showing the average latency, $\overline{L}$, and average energy, $\overline{E}$, as a function of the number of UEs, N, the MAC protocol (either Slotted or Unslotted), and pilot line layout (either Robopac-Aetna or Bi-Rex). As expected, in both cases, there is

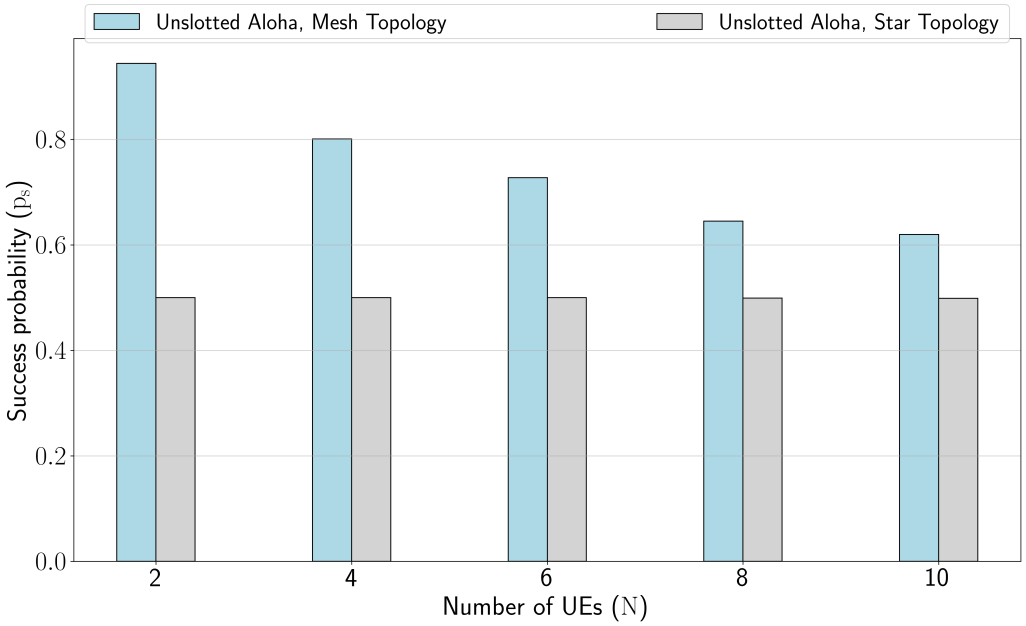

Figure 64: Success probability, p_s, for the Unslotted Aloha protocol as a function of the number of UEs, N, and the network architecture (either star or mesh).

an increasing trend with the number of UEs due to the higher number of collisions that in turn cause more retransmissions.

When examining latency across both pilot line scenarios, the Unslotted Aloha emerges as the optimal MAC protocol due to its lack of synchronization. Furthermore, the reduced propagation delays associated with the Robopac-Aetna layout contribute to additional latency reduction, which nevertheless never exceeds 3 microseconds.

When considering average energy consumption and the Unslotted Aloha MAC protocol, as expected, it is evident that the increased number of retransmissions inherent in the Robopac-Aetna scenario leads to a higher $\overline{E}$ compared to the Bi-Rex layout. This is because the uncoordinated nature of this protocol results in higher power consumption due to retransmissions of unsuccessfully received data packets, compared to those caused by the longer WAIT state characteristic of the Bi-Rex scenario. In contrast, the Slotted Aloha MAC protocol performs worse because of its time slots, which results again in significantly longer BO and waiting times. Additionally, the Bi-Rex scenario exhibits higher average energy consumption for Slotted Aloha due to the greater impact of causing higher propagation delays.

3.5.2 Performance of a THz-based mesh network

In this section, we focus on the Unslotted Aloha protocol because on average it exhibits better performance than the Slotted one, as previously shown in Sec. 3.5.1. Specifically, for mesh networking, we consider the proposed flooding-based extension of Unslotted Aloha described in Sec. 3.3.2. We evaluate the performance of our proposed THz-based mesh network in terms of success probability, p_s, network throughput, S, average latency $\overline{L}$, and average energy consumption $\overline{E}$, comparing them with that of the star network. To ensure a fair comparison between the two network architectures, we consider the Robopac-Aetna pilot line layout and G_{BS} = 14.5 dB, meaning that half of the UEs are positioned in machines directly connected to the BS (i.e., the $SNR \geq SNR_{th}$), and the other half of the UEs are not connected. In particular, we set the requirement on the success probability at PHY layer, $p_{phy} = 0.9$ and we derive the SNR_{th} according to what is explained in Sec.

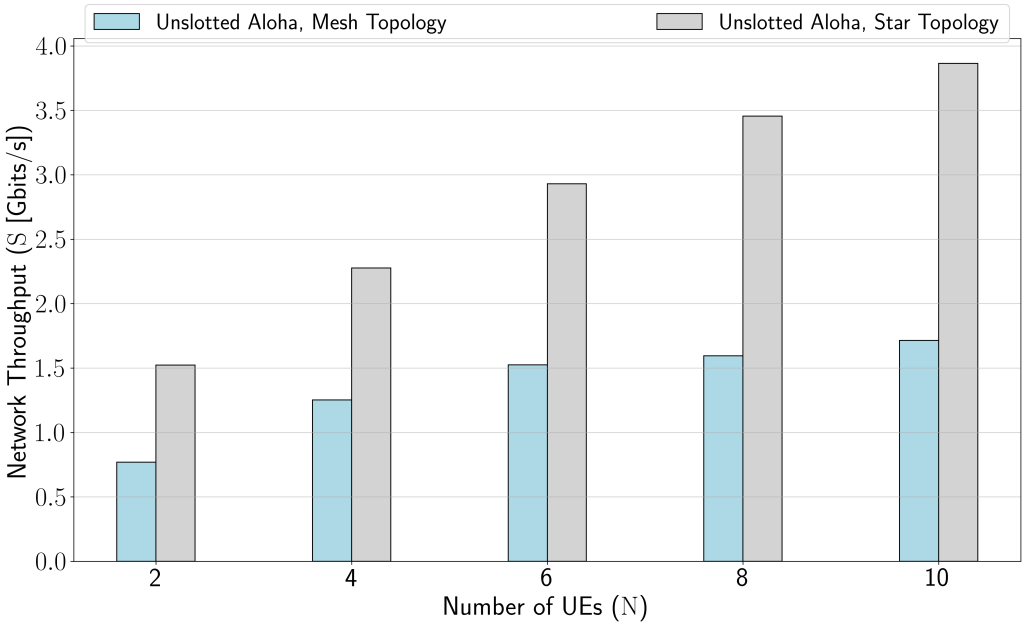

Figure 65: Network throughput at the MAC layer, S, for the Unslotted Aloha protocol as a function of the number of UEs, N, and the network architecture (either star or mesh).

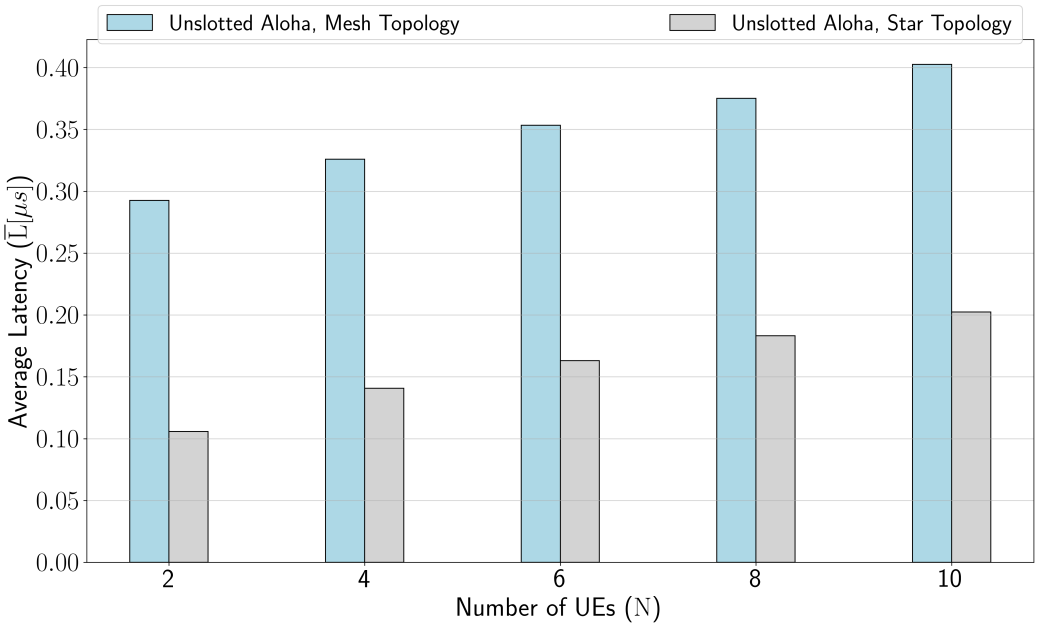

Figure 66: Average Latency, $\overline{L}$, for the Unslotted Aloha protocol as a function of the number of UEs, N, and the network architecture (either star or mesh).

3.2.4.

We start the analysis with Figure 64, where the success probability, p_s, is portrayed as a function of the number of UEs, *N*, and the two network architectures (either star or mesh). Examining the p_s values for a

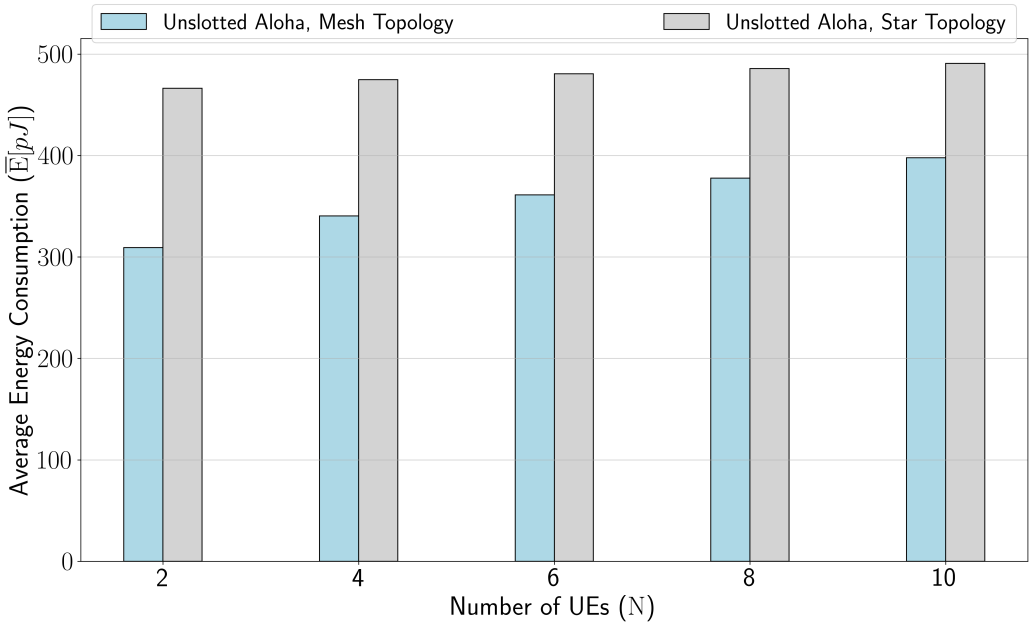

Figure 67: Average Energy Consumption, $\overline{E}$, for the Unslotted Aloha protocol as a function of the number of UEs, N, and the network architecture (either star or mesh).

specific number of UEs in both the mesh and star network setups, it's apparent that the mesh outperforms the star. This difference arises because, in the star network, half of the UEs remain unconnected to the BS, resulting in communication failures. Conversely, in the mesh network, all UEs broadcast their data, enabling neighboring devices within their coverage area to successfully receive it, provided they are in a reception state (either in BO or awaiting ACK after data transmission). The proposed flooding-based solution ensures reliable data reception by the BS, even from UEs that can not directly communicate with it. This difference becomes particularly evident with 2 UEs, where the p_s in the mesh solution is double that of the star, as one UE in the star network never successfully transmits to the BS. As the number of UEs increases from 2 to 10, the p_s values for the star network remain almost constant, close to 0.5. This is because only half of the UEs successfully transmit their data to the BS, leading to a low number of data collisions at the MAC layer. On the contrary, in the mesh network, the implementation of flooding-based Unslotted Aloha leads to an increase in protocol overhead due to the data sent in broadcast to allow forwarding by other UEs. Consequently, as the number of UEs increases, p_s decreases because the number of collisions at the MAC side increases. Despite this, the mesh solution provide better performance in terms of p_s than the star, even for 10 UEs.

Then, Figure 65 shows the network throughput at the MAC layer, S as a function of the number of UEs, N, and the two network architectures. The graph shows an increasing trend of S as the number of UEs increases, both for the mesh and the star solution. Since the number of UEs in the network is low, the optimal value of the network throughput will be achieved for a higher number of UEs than 10, as can be seen in Fig. 61, for the basic Unslotted Aloha protocol, i.e., star topology, and Robopac-Aetna layout. Furthermore, the trend is reversed from that obtained in Fig. 64, where the performance of the mesh network in terms of p_s overcomes that of the star. In this graph, in fact, it is observed that the network throughput of the star network is higher than that of the mesh, because the former is characterized by a lower protocol overhead (BO time is lower, as explained in Sec. 3.3.1), no forwarding, and therefore on average the BS successfully receives a higher number of data packets. Despite this, we remark that, in the star network topology, only half of the UEs can directly communicate with the BS, and thus the advantage gained in terms of network throughput in the star should be considered with the understanding that this solution does not provide the possibility for the BS to be able to receive data from all UEs (thereby not satisfying their requirements), contrary to what happens in the mesh solution.

Figures 66 and 67 conclude the performance analysis of our THz-based mesh network by showing the average latency, $\overline{L}$, and average energy, $\overline{E}$, as a function of the number of UEs, N, and the two network architectures. In both the two cases, there is an increasing trend with the number of UEs due to the higher number of collisions that in turn cause more retransmissions.

Focusing on Figure 66, it is evident that $\overline{L}$ is always higher in the mesh network compared to that of the star network because a UE generally takes longer to successfully transmit data to the BS. Firstly, this is because the BO duration is typically longer in the mesh network to allow a UE to receive at least one data packet from other UEs. Secondly, a UE acting as a relay must first send an ACK to the transmitting UE before forwarding the reception, along with the buffered data, to the BS. Both factors clearly cause longer latency values.

Conversely, Figure 67 shows that $\overline{E}$ is higher in the star network. This is because half of the UEs are never able to successfully communicate with the BS, leading them to repeatedly attempt to transmit each generated packet until reaching the maximum number of retransmissions before discarding it. In contrast, in the mesh network, UEs not directly connected to the BS can successfully transmit their data through other UEs acting as relays, resulting in lower retransmissions and thereby a reduced energy consumption.

3.6 Architecture design for the simulation of RIS-based mesh networks

The performances of the THz-based star network and the THz-based mesh network, previously shown, are achieved by considering a simple narrowband channel model, which takes into account the SNR at the receiver (see Eq. 87). Therefore, this section presents the concept behind a much more comprehensive and accurate PHY layer model that incorporates the following key features:

- **Wideband Channel Model**: The model considers the frequency-dependent characteristics of the wireless channel, providing a more realistic representation of the propagation environment compared to narrowband models.
- **Agnostic Approach**: The simulator can effortlessly accommodate both NF and FF propagation conditions, allowing for the evaluation of network performance in various deployment scenarios.
- **Interference Modeling**: The simulator computes SINR as KPI, which considers the interference between each UE and not only the noise, providing the possibility to predict and analyze the impact of signal interference on network performance.
- **RISs Integration**: The simulator includes the presence of RISs in the scenario. This feature enables the evaluation of network performance by exploiting the alternative paths created by RISs within the environment, effectively acting as an additional forwarding strategy.
- **Beamforming and Diversity Gain**: Our simulator focuses on a Single Input Multiple Output (SIMO) system implementation, where these techniques can be applied at the receiver to enhance the received signal power and counteract fading effects.

By studying the quality of the links from the above PHY layer perspective, it is possible to consider the impact of these more realistic features on the MAC scheduler evaluation. In this way, the MAC simulator can have more accurate information about the links between UEs-BSs and effectively manage the allocation of resources, optimizing efficient data transmission.

3.6.1 Analysis of the simulator architecture

This section then provides a high-level overview of the PHY simulator architecture that implements the above concept. More detailed information about the parameter definitions, models used by the simulator and results will be presented in the next deliverable.

Table 8 summarizes the objects that the simulator can manage within the scenario. Each object is defined using 3-D coordinates. While UEs utilize a single antenna element because the simulator considers a SIMO system,

UE	BS	RIS	OBSTACLE	ADDITIONAL PARAMETERS
3D centroid positions [m]	3D centroid positions [m]	3D centroid positions [m]	3D centroid positions [m]	Bandwidth [Hz]
Transmission Power [dBm]	Rotation Offset [°]	Rotation Offset [°]	Obstacle length [m]	Carrier frequency [Hz]
Active Subchannels	Number of antenna elements	Number of antenna elements	Obstacle width [m]	-
-	Antenna elements spacing [m]	Antenna elements spacing [m]	Obstacle height [m]	-
-	Lattice	Lattice	-	-
-	Noise Figure [dB]	-	-	-

Table 8: Input parameters of the physical layer simulator.

BSs, and RISs can be oriented and configurated with multiple antenna elements, with different antenna spacing and lattice, such as uniform linear array (ULA) or UPA. The simulator utilizes the geometrical information of the elements within the environment to evaluate the LOS or NLOS status for each link connecting UEs, active RISs, and BSs. Then, it computes the end-to-end channel vector, considering the free space propagation between each transmitting and receiving antenna element. Finally, the simulator calculates the SINR, for each UE, employing two diversity schemes at the receiver: Minimum Mean Square Error (MMSE) and MR combining. The MMSE technique is particularly suited for scenarios where interference presence needs to be carefully considered, offering a robust solution to mitigate its impact on signal quality. On the other hand, MR combing focuses on maximizing the SNR, optimizing reception performance without including interference considerations. By exploiting these channel modeling and SINR calculation techniques, the MAC simulator can achieve a more accurate assessment of network performance, enabling informed decision-making and efficient resource allocation.

3.6.2 Integration between physical and MAC layer simulators

As previously mentioned, the purpose of this PHY layer simulator, developed in MATLAB, is to interface with the Python-based MAC layer simulator to provide more realistic results. To effectively integrate these two simulators, a structured approach is essential and is described in the following.

The PHY layer simulator is modularized into two MATLAB functions that the MAC simulator can call from Python. Figure 68 illustrates the simulation flow:

(i) The MAC simulator calls the MATLAB “Initialization” function, which is designed to be executed once. It retrieves the scenario parameters from a “.mat” file generated by the MAC simulator **(1)**, sets up the scenario for the PHY simulator, and saves the workspace into a “.mat” file **(2)**. This file establishes the MATLAB global variables environment for the subsequent function by loading it. Additionally, the function returns details regarding the angular sectors covered by each RIS **(3)**.

(ii) The Python-based MAC simulator, collects UE details, information about the obstacles, and optimal configuration for active RISs **(4)** **(5)**. It can then invoke the main function “Physical Layer Simulator” **(6)**, which considers updated inputs and global variables **(7)** to calculate the SINR for each UE-BS link **(8)**.

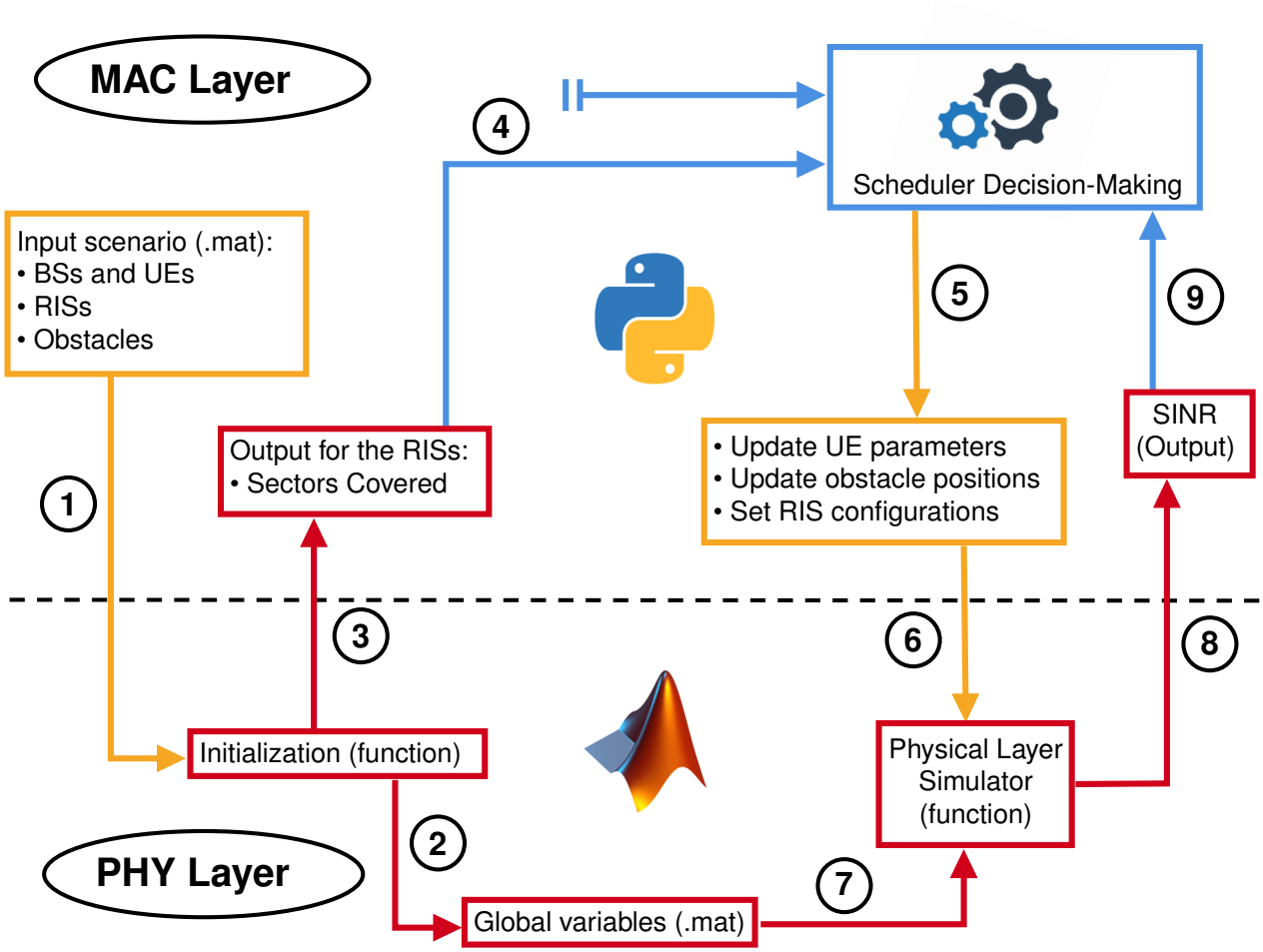

Figure 68: Simulation flow

(iii) On the MAC layer side, the simulator uses the accurate indicators of SINR to evaluate the network level performance **(9)**.

It is important to highlight that the MAC simulator can set up a cyclic invocation of the second MATLAB function **(5-9)** for each transmission. This approach enables dynamic scenario monitoring and eases the evaluation of how MAC scheduler decisions influence the PHY layer. By incorporating this iterative process, the simulator can continuously assess and adapt to changing conditions, such as variations in traffic patterns and channel quality, thereby improving its overall effectiveness in analyzing network performance over time.

4 Conclusions

The results presented in this deliverable can be summarized as follows. We firstly investigated the theoretic performance of a RIS-aided scenario in a factory environment. We then improved the system model by considering RF impairments on RIS-based networks at THz, and we also considered a multi-carrier approach employing passive metaprisms. In the second part of the deliverable, we proposed a network-level analysis at THz frequencies for the real factory floors of Robopac-Aetna and Bi-Rex. Specifically, we considered four KPIs (Success Probability, Network Throughput, Latency, and Energy Consumption) and compared the performance of two network architectures (star and two-hop mesh) and two MAC protocols (Slotted and Unslotted Aloha). Notably, the MAC protocol design accounts for propagation delays, which play a significant role at these frequencies. Additionally, we proposed an innovative flooding-based extension of the Unslotted Aloha MAC protocol to enable mesh networking. These results are presented in the worst-case offered traffic condition and as a function of (i) the industrial environments, which have been meticulously modeled in terms of dimensions and obstacles, and (ii) the number of UEs (each UE is assumed to be mounted on different assets of industrial machines).

4.1 Results and lessons learned

Numerical results reveal that:

1. when considering RIS-aided scenarios, the RIS size increases (in the order of tens of thousands elements) as the carrier frequency increases in order to offset the loss due to the indirect propagation paths; in this context, it is also important to evaluate the directivity features of the RIS to compensate for the path loss;
2. when focusing on the achievable throughputs, the most crucial parameters, in order to achieve significant performance and to limit the penalty gap between direct and indirect links, are represented by the antenna gains at the BS and the RIS;
3. when exploiting the spherical model to achieve spatial multiplexing in a RIS-assisted scenario, placing the RIS close to the BS is the optimal choice for achieving highest capacity, which appears in the region with the highest number of eigenchannels used, while the sensitivity analysis with respect to UE displacements exhibits that this region is also most prone to significant drops in capacity;
4. when considering the RF impairments, phase errors at the RIS are shown to highly impact the performance of the spectral efficiency and the choice of the modulation order;
5. the use of frequency-selective surfaces, called metaprisms, can be employed to cover areas in NLoS conditions with the BS or as a transmitted antenna array in LoS conditions. Unlike RIS, they do not require any power supply, signaling overhead, and are of low complexity while still achieving the same performance in terms of coverage;
6. metaprisms can also be utilized for localization applications, where a user or target is in NLoS conditions with the BS, and the metaprism is used as a passive reflector to assist the BS in the localization task;
7. when considering intelligent surfaces at THz, only the ad-hoc configurations of the RIS allows for a decent reconstruction of the reference image, also noting that the accuracy and resolution of the reconstructed image can be significantly enhanced when optimizing the transmitted waveform from the transceiver to appropriately illuminate the RIS;
8. when considering MAC protocols, Slotted Aloha ensures a higher success probability due to the halving of the contention window. However, considering network throughput, latency and energy consumption, the unsynchronized nature of Unslotted Aloha, i.e., lower waiting times, makes it the superior MAC protocol;
9. in terms of quantitative results, using the Aloha MAC protocol at THz frequencies results in average network throughputs of a few tens of Gbit/s and average latencies of less than 3 μs, even in crowded networks with 50 UEs, that is compatible with many requirements of industrial applications;

10. when considering real industrial environments, the Robopac-Aetna and Bi-Rex scenarios result in diverse network performances due to variations in distances and, consequently, propagation delays. Specifically, a trade-off exists: higher propagation delays increase the likelihood that simultaneous transmissions arrive at the receiver at different times, at the cost of longer transmission times. Clearly, the Slotted Aloha MAC protocol is more affected by the latter downside, leading to poorer performances in wide industrial environments (like Bi-Rex). However, these considerations confirm that propagation delays should be taken into account in the design of MAC protocols at THz frequencies.
11. as far as the network architecture is concerned, the proposed MAC protocol for mesh networking outperforms the Unslotted-Aloha MAC protocol for a star topology in terms of success probability because it also provides access to UEs that cannot reach the BS, that is, UEs located in far machines. Additionally, UEs do not waste energy in retransmitting data intended solely to the BS, as this may not always be possible due to coverage issues. However, the star network offers higher network throughput and latency performance than the mesh solution because of the lack of control plane overhead to enable data forwarding to the BS and lower waiting/idle times, at the cost of having UEs that never successfully transmit to the BS.

4.2 Future work

The objective of this deliverable was to present the opportunities offered by the exploitation of smart environments within multi-goal mesh networks at THz frequencies. To do so, the deliverable has followed a two-part structure, which has mirrored typical layered architectures: one part for the physical layer algorithms and studies and one part for the MAC and network layers algorithms. Each part has developed a simulator. Future work, which will result in the Deliverable 4.4, will be organized to follow two convergent paths:

1. build on the knowledge accumulated and on the lessons learned to further improve the proposed algorithms;
2. harmonize the two parts to give consistent answers on the potentials of smart sensing and propagation in THz industrial networks.

A specific point of attention is represented by the two simulators. In this case, the goal of the future activity is to compare results, harmonize different contributions/settings, and eventually share data among the simulators, to provide a comprehensive multi-layered approach, including a PHY layer model that incorporates smart propagation environments and RISs, along with the proposed MAC layer and network-level tools.

References

[1] Sean Victor Hum and Julien Perruisseau-Carrier. Reconfigurable reflectarrays and array lenses for dynamic antenna beam control: A review. *IEEE transactions on antennas and propagation*, 62(1):183–198, 2013.

[2] Wankai Tang, Ming Zheng Chen, Xiangyu Chen, Jun Yan Dai, Yu Han, Marco Di Renzo, Yong Zeng, Shi Jin, Qiang Cheng, and Tie Jun Cui. Wireless communications with reconfigurable intelligent surface: Path loss modeling and experimental measurement. *IEEE transactions on wireless communications*, 20(1):421–439, 2020.

[3] Steven W Ellingson. Path loss in reconfigurable intelligent surface-enabled channels. In *2021 IEEE 32nd Annual International Symposium on Personal, Indoor and Mobile Radio Communications (PIMRC)*, pages 829–835. IEEE, 2021.

[4] David R Smith, Okan Yurduseven, Laura Pulido Mancera, Patrick Bowen, and Nathan B Kundtz. Analysis of a waveguide-fed metasurface antenna. *Physical Review Applied*, 8(5):054048, 2017.

[5] Stanislav B Glybovski, Sergei A Tretyakov, Pavel A Belov, Yuri S Kivshar, and Constantin R Simovski. Metasurfaces: From microwaves to visible. *Physics reports*, 634:1–72, 2016.

[6] Viktar S Asadchy, Mohammad Albooyeh, Svetlana N Tcvetkova, Ana Díaz-Rubio, Younes Ra'di, and Sergei A Tretyakov. Perfect control of reflection and refraction using spatially dispersive metasurfaces. *Physical Review B*, 94(7):075142, 2016.

[7] Carl Pfeiffer and Anthony Grbic. Metamaterial huygens' surfaces: tailoring wave fronts with reflectionless sheets. *Physical review letters*, 110(19):197401, 2013.

[8] Michael Selvanayagam and George V Eleftheriades. Circuit modeling of huygens surfaces. *IEEE Antennas and Wireless Propagation Letters*, 12:1642–1645, 2013.

[9] Nasim Mohammadi Estakhri and Andrea Alu. Wave-front transformation with gradient metasurfaces. *Physical Review X*, 6(4):041008, 2016.

[10] TIMES. Deliverable 4.1 - intermediate report on phy layer enhancements for thz links supporting sensing and communication functionalities. Technical report, TIMES, 2023.

[11] Emil Björnson, Jakob Hoydis, Luca Sanguinetti, et al. Massive mimo networks: Spectral, energy, and hardware efficiency. *Foundations and Trends® in Signal Processing*, 11(3-4):154–655, 2017.

[12] Giacomo Bacci, Luca Sanguinetti, and Emil Björnson. Spherical wavefronts improve MU-MIMO spectral efficiency when using electrically large arrays. *IEEE Wireless Communications Letters*, 2023.

[13] Giulio Bartoli, Andrea Abrardo, Nicolo Decarli, Davide Dardari, and Marco Di Renzo. Spatial multiplexing in near field MIMO channels with reconfigurable intelligent surfaces. *IET Signal Processing*, 17(3):e12195, Mar. 2023.

[14] Özgecan Özdogan, Emil Björnson, and Erik G Larsson. Intelligent reflecting surfaces: Physics, propagation, and pathloss modeling. *IEEE Wireless Communications Letters*, 9(5):581–585, 2019.

[15] Kanti V Mardia and Peter E Jupp. *Directional statistics*. John Wiley & Sons, 2009.

[16] Milton Abramowitz and Irene A Stegun. *Handbook of mathematical functions with formulas, graphs, and mathematical tables*, volume 55. US Government printing office, 1948.

[17] Andrea J Goldsmith and Soon-Ghee Chua. Variable-rate variable-power mqam for fading channels. *IEEE transactions on communications*, 45(10):1218–1230, 1997.

[18] Mohamed-Slim Alouini and Andrea J Goldsmith. Adaptive modulation over nakagami fading channels. *Wireless Personal Communications*, 13:119–143, 2000.

[19] Davide Dardari and Devis Massari. Using metaprisms for performance improvement in wireless communications. *IEEE Transactions on Wireless Communications*, 20(5):3295–3307, 2021.

[20] Marina Lotti and Davide Dardari. Metaprism-aided nlos target localization. In *2023 31st European Signal Processing Conference (EUSIPCO)*, pages 895–899. IEEE, 2023.

[21] Marina Lotti, Giacomo Calesini, and Davide Dardari. Nlos localization exploiting frequency-selective metasurfaces. *arXiv preprint arXiv:2307.12800*, 2023.

[22] Syed Abdullah Nauroze, Xuanke He, and Manos M Tentzeris. Fully additively manufactured tunable active frequency selective surfaces with integrated on-package solar cells for smart packaging applications. In *2019 IEEE 69th Electronic Components and Technology Conference (ECTC)*, pages 119–125. IEEE, 2019.

[23] Gengyu Xu, Sean V Hum, and George V Eleftheriades. Systematic design of single-layer multi-stop-band frequency selective surfaces. In *2017 IEEE International Symposium on Antennas and Propagation & USNC/URSI National Radio Science Meeting*, pages 261–262. IEEE, 2017.

[24] Grace HH Sung, Kevin W Sowerby, and AG Williamson. The impact of frequency selective surfaces applied to standard wall construction materials. In *IEEE Antennas and Propagation Society Symposium, 2004.*, volume 2, pages 2187–2190. IEEE, 2004.

[25] Xuehan Chen, Jingjing Tan, Litian Kang, Fengxiao Tang, Ming Zhao, and Nei Kato. Frequency selective surface towards 6g communication systems: A contemporary survey. *IEEE Communications Surveys and Tutorials*, pages 1–1, 2024.

[26] Constantine A Balanis. *Antenna theory: analysis and design*. John wiley & sons, 2016.

[27] Davide Dardari, Nicolò; Decarli, Anna Guerra, and Francesco Guidi. LOS/NLOS near-field localization with a large reconfigurable intelligent surface. *IEEE Transactions on Wireless Communications*, 21(6):4282–4294, June 2022.

[28] Fan Jiang, Andrea Abrardo, Kamran Keykhosravi, Henk Wymeersch, Davide Dardari, and Marco Di Renzo. Two-timescale transmission design and RIS optimization for integrated localization and communications. *IEEE Transactions on Wireless Communications*, 22(12):8587–8602, 2023.

[29] Davide Dardari. Communicating with large intelligent surfaces: Fundamental limits and models. *IEEE J. Sel. Areas Commun.*, 38(11):2526–2537, Nov. 2020.

[30] Silvia Palmucci, Anna Guerra, Andrea Abrardo, and Davide Dardari. Two-timescale joint precoding design and ris optimization for user tracking in near-field MIMO systems. *IEEE Trans. Signal Process.*, Aug. 2023.

[31] Fan Liu, Yuanhao Cui, Christos Masouros, Jie Xu, Tony Xiao Han, Yonina C Eldar, and Stefano Buzzi. Integrated sensing and communications: Toward dual-functional wireless networks for 6G and beyond. *IEEE J. Sel. Areas Commun.*, 40(6):1728–1767, Mar. 2022.

[32] Francesco Guidi, Anna Guerra, and Alberto Zanella. Performance analysis of randomly distributed reconfigurable intelligent surfaces with different phase profiles. *IEEE Trans. Wireless Commun.*, pages 1–1, To Appear, 2023.

[33] Ahmed Elzanaty, Anna Guerra, Francesco Guidi, Davide Dardari, and Mohamed-Slim Alouini. Toward 6G holographic localization: Enabling technologies and perspectives. *IEEE Internet of Things Magazine*, 6(3):138–143, Sep. 2023.

[34] Haiyang Zhang, Nir Shlezinger, Francesco Guidi, Davide Dardari, and Yonina C. Eldar. 6G wireless communications: From far-field beam steering to near-field beam focusing. *IEEE Communications Magazine*, 61(4):72–77, April 2023.

[35] Nuria González-Prelcic, Musa Furkan Keskin, Ossi Kaltiokallio, Mikko Valkama, Davide Dardari, Xiao Shen, Yuan Shen, Murat Bayraktar, and Henk Wymeersch. The integrated sensing and communication revolution for 6G: Vision, techniques, and applications. *Proc. of the IEEE*, pages 1–16, 2024.

[36] Marina Lotti, Gianni Pasolini, Anna Guerra, Francesco Guidi, Raffaele D'Errico, and Davide Dardari. Radio SLAM for 6G systems at THz frequencies: Design and experimental validation. *IEEE Journal of Selected Topics in Signal Processing*, 17(4):834–849, July 2023.

[37] Giulia Torcolacci, Anna Guerra, Haiyang Zhang, Francesco Guidi, Qianyu Yang, Yonina C Eldar, and Davide Dardari. Holographic imaging with XL-MIMO and RIS: Illumination and reflection design. *arXiv preprint arXiv:2312.11102*, Dec. 2023.

[38] Giulia Torcolacci, Anna Guerra, Haiyang Zhang, Francesco Guidi, Qianyu Yang, Yonina C Eldar, and Davide Dardari. RIS-empowered near-field imaging in NLOS scenarios. *Proc. IEEE ICC,*, Jun. 2024.

[39] Davide Tornielli Bellini, Dario Tagliaferri, Marouan Mizmizi, Stefano Tebaldini, and Umberto Spagnolini. Multi-view near-field imaging in NLOS with non-reconfigurable EM skins. *arXiv e-prints*, pages arXiv–2401, 2024.

[40] Juan M Lopez-Sanchez and Joaquim Fortuny-Guasch. 3-D radar imaging using range migration techniques. *IEEE Trans. Antennas Propag.*, 48(5):728–737, May 2000.

[41] Jingkun Gao, Yuliang Qin, Bin Deng, Hongqiang Wang, and Xiang Li. Novel efficient 3D short-range imaging algorithms for a scanning 1D-MIMO array. *IEEE Trans. Image Process.*, 27(7):3631–3643, Apr. 2018.

[42] Joseph N Mait, Gary W Euliss, and Ravindra A Athale. Computational imaging. *Adv. Opt. Photonics*, 10(2):409–483, 2018.

[43] Antoni Broquetas, Josep Palau, Luis Jofre, and Angel Cardama. Spherical wave near-field imaging and radar cross-section measurement. *IEEE Trans. Antennas Propag.*, 46(5):730–735, May 1998.

[44] Yang Tao and Zhaoyang Zhang. Distributed computational imaging with Reconfigurable Intelligent Surface. In *Proc. Int. Conf. Wireless Commun. Signal Process. (WCSP)*, pages 448–454, Oct. 2020.

[45] C.A. Balanis. *Antenna Theory: Analysis and Design*. Wiley, 2015.

[46] Mario Bertero, Patrizia Boccacci, and Christine De Mol. *Introduction to inverse problems in imaging*. CRC press, 2021.

[47] Richard H Byrd, Mary E Hribar, and Jorge Nocedal. An interior point algorithm for large-scale nonlinear programming. *SIAM J. on Optimiz.*, 9(4):877–900, Sep. 1999.

[48] Ahmed Kirmani, Tyler Hutchison, James Davis, and Ramesh Raskar. Looking around the corner using transient imaging. In *Proc. IEEE 12th Int.Conf. Computer Vision*, pages 159–166, Oct. 2009.

[49] TIMES. Deliverable 2.2 - definition of scenarios for software simulation. Technical report, TIMES, 2023.

[50] Johannes M. Eckhardt, Christoph Herold, Bo Kum Jung, Nils Dreyer, and Thomas Kürner. Modular Link Level Simulator for the Physical Layer of Beyond 5G Wireless Communication Systems. *Radio Sci.*, 57(2):e2021RS007395, 2022.

[51] Michael Schweins, Lennart Thielecke, Nils Grupe, and Thomas Kürner. Optimization and Evaluation of a 3-D Ray Tracing Channel Predictor Individually for Each Propagation Effect. *IEEE Open Journal of Antennas and Propagation*, 5(2):495–506, April 2024.

[52] Dennis M. Rose, Johannes Baumgarten, Soren Hahn, and Thomas Kurner. SiMoNe - Simulator for Mobile Networks: System-Level Simulations in the Context of Realistic Scenarios. In *2015 IEEE 81st Vehicular Technology Conference (VTC Spring)*, pages 1–7, May 2015.

[53] Nils Dreyer and Thomas Kürner. An Analytical Raytracer for Efficient D2D Path Loss Predictions. In *2019 13th European Conference on Antennas and Propagation (EuCAP)*, pages 1–5, March 2019.

[54] Johannes M. Eckhardt. *THz Communications in a Data Center: Channel Measurements, Modeling and Physical Layer Analysis*. PhD thesis, Technische Universität Braunschweig, 2024.

[55] Christoph Herold and Thomas Kürner. A Concept for the Efficient Integration of Reconfigurable Intelligent Surfaces into a Ray Tracing Framework. In *2023 48th International Conference on Infrared, Millimeter, and Terahertz Waves (IRMMW-THz)*, pages 1–2, September 2023.

[56] Soren Hahn, Dennis M. Rose, Jaroslaw Sulak, and Thomas Kurner. Impact of Realistic Pedestrian Mobility Modelling in the Context of Mobile Network Simulation Scenarios. In *2015 IEEE 81st Vehicular Technology Conference (VTC Spring)*, pages 1–5, May 2015.

[57] IEEE Standard for High Data Rate Wireless Multi-Media Networks–Amendment 2: 100 Gb/s Wireless Switched Point-to-Point Physical Layer.

[58] TIMES. Deliverable 2.1 - definition of scenarios and kpi for hardware demonstration and poc. Technical report, TIMES, 2023.

[59] 3GPP. Study on channel model for frequencies from 0.5 to 100 GHz (Release 16). *TS 38.901*, 2019.